AER/AGS Report 103

Alberta Energy Regulator

CO_2 Capacity Estimation and Caprock Assessment of the Leduc-Ireton Storage Complex in Central Alberta

AGS
ALBERTA GEOLOGICAL SURVEY

AER/AGS Report 103

CO_2 Capacity Estimation and Caprock Assessment of the Leduc-Ireton Storage Complex in Central Alberta

T.E. Hauck[1], S. Lyster[1], D. Palombi[1], L.J. Knapp[1], L. Maliki[2] and C. Virues[3]

[1] Alberta Energy Regulator – Alberta Geological Survey
[2] Alberta Energy Regulator – Regulatory Applications
[3] Alberta Energy Regulator – Technical Science & External Innovation Support

November 2026

©His Majesty the King in Right of Alberta, 2026
ISBN 978-1-4601-6604-8

The Alberta Energy Regulator / Alberta Geological Survey (AER/AGS), its employees and contractors make no warranty, guarantee, or representation, express or implied, or assume any legal liability regarding the correctness, accuracy, completeness, or reliability of this publication. Any references to proprietary software and/or any use of proprietary data formats do not constitute endorsement by the AER/AGS of any manufacturer's product.

If you use information from this publication in other publications or presentations, please acknowledge the AER/AGS. We recommend the following reference format:

Hauck, T.E., Lyster, S., Palombi, D., Knapp, L.J., Maliki, L. and Virues, C. (2026): CO_2 capacity estimation and caprock assessment of the Leduc-Ireton storage complex in central Alberta; Alberta Energy Regulator / Alberta Geological Survey, AER/AGS Report 103, 77 p.

Published November 2026 by:
Alberta Energy Regulator
Alberta Geological Survey
4th Floor, Twin Atria Building
4999 – 98th Avenue
Edmonton, AB T6B 2X3
Canada

Tel: 780.638.4491
Fax: 780.422.1459
Email: AGS-Info@aer.ca
Website: www.ags.aer.ca

Contents

Acknowledgements vi
Abstract vii
1 Introduction 1
2 Geological Setting 3
3 Methods and Results 3
3.1 Stratigraphic Mapping and Hydrocarbon Pools 3
3.1.1 Leduc-Ireton Storage Complex 5
3.2 Stratigraphic Modelling 9
3.3 Petrophysical Evaluation 10
3.4 Property Modelling 12
3.4.1 Hydrocarbon-Water Contacts 12
3.4.2 Upscaling 3D Properties 15
3.4.3 Pressure and Temperature 16
3.4.4 Quantifying Uncertainty 16
3.5 CO_2 Capacity Estimation 17
3.5.1 Fluid Substitution 17
3.5.2 Results: Fluid Substitution in Leduc Formation Hydrocarbon Pools 19
3.5.3 DOE-NETL Methods 20
3.5.4 Oil and Gas Methodology Results 24
3.5.5 Saline Aquifer Methodology Results 25
3.6 Clive Field Benchmarking 27
4 Ireton Formation Caprock Integrity Assessment 30
4.1 Lithofacies 30
4.2 MICP Analysis 32
4.3 Petrography 36
5 Discussion and Future Work 40
5.1 Leduc Formation CO_2 Capacity Estimates 40
5.2 Ireton Formation Caprock Assessment 42
5.3 Summary 43
6 References 45
Appendix 1 – Leduc Formation Hydrocarbon Pool Ultimate Recovery Tables 49
Appendix 2 – Fluid Substitution Results by Leduc Formation Pool 53
Appendix 3 – CO_2 Mass Estimate Results 57
Appendix 4 – Ireton Formation Lithologs 60

Tables

Table 1. Petrophysical methods and calibration parameters. 9
Table 2. Summary statistics for upscaled 3D properties in the property model. 15
Table 3. Summary statistics for upscaled 2D properties in the property model. 16
Table 4. Oil and gas reservoirs with ultimate recoveries greater than 10 000 10^3m^3. 18
Table 5. Non-associated gas reservoirs with ultimate recoveries greater than 1000 10^6m^3. 19
Table 6. Fluid substitution results (CO_2 volume and mass at storage pressure) for Leduc Formation oil and gas reservoirs with ultimate recoveries greater than 10 000 10^3m^3 19
Table 7. Fluid substitution results (CO_2 volume and mass at storage pressure) for Leduc Formation non-associated gas reservoirs with ultimate recoveries greater than 1000 10^6m^3. 20
Table 8. Terms in the capacity estimate equations as used in this work. 20
Table 9. Description of the different terms in the efficiency factors (Goodman et al., 2011). 21

Table 10. Input efficiency factor distributions and simulated total efficiency factor results; input values are from Goodman et al. (2011). 22
Table 11. Comparison of the Clive D-3A Pool reservoir parameters for the fluid substitution method and volumetric results. 29
Table 12. Ireton Formation cores logged for the study, and their location with respect to the underlying Leduc Formation buildups. 30
Table 13. Ireton Formation lithofacies and associated MICP sample numbers from cores overlying Leduc Formation buildups. 31
Table 14. Interfacial tension and contact angle values (from Kawaura et al., 2013) used in this study. 33
Table 15. Capillary pressure data and calculated CO_2 column height from the 20 MICP samples taken from the Ireton Formation. 35
Table A1. Oil and gas reservoirs with ultimate recoveries greater than 5000 10^3m^3 49
Table A2. Oil and gas reservoirs with ultimate recoveries greater than 1000 10^3m^3 49
Table A3. Oil and gas reservoirs with ultimate recoveries greater than 100 10^3m^3 50
Table A4. Non-associated gas reservoirs with ultimate recoveries greater than 500 10^6m^3. 51
Table A5. Non-associated gas reservoirs with ultimate recoveries greater than 100 10^6m^3. 52
Table B1. Oil reservoirs with ultimate recoveries greater than 5000 10^3m^3. 53
Table B2. Oil reservoirs with ultimate recoveries greater than 1000 10^3m^3. 53
Table B3. Oil reservoirs with ultimate recoveries greater than 100 10^3m^3. 54
Table B4. Non-associated gas reservoirs with ultimate recoveries greater than 500 10^6m^3. 56
Table B5. Non-associated gas reservoirs with ultimate recoveries greater than 100 10^6m^3. 56
Table C1. Results of CO_2 mass estimates (in megatonnes) for the DOE-NETL oil and gas, and fluid substitution methods 57

Figures

Figure 1. Location and simplified stratigraphic column for the study area in central Alberta. 2
Figure 2. Location of select hydrocarbon pools (outlined in green) and estimated resources in the Leduc Formation buildup complexes in central Alberta. 4
Figure 3. Variation in Leduc Formation buildup thicknesses near the city of Edmonton 6
Figure 4. Thickness of the Ireton Formation (caprock) within the study area 8
Figure 5. An isometric view of the geological model horizons from top Leduc horizon down. 10
Figure 6. Map view of the hydrocarbon-water contact data points (green), Leduc Formation pool outlines (red), geological model area (blue), and Leduc buildup outlines (pink). 14
Figure 7. An isometric view of the hydrocarbon-water zone model within the Leduc Formation. 15
Figure 8. Matrix limestone fraction (0.1 to 0.6, with 0.6 representing pure limestone, 0.1 representing pure dolostone) within the Bashaw and Redwater (Leduc Formation) buildups. 23
Figure 9. Forty-four Leduc Formation oil and gas pools evaluated by at least two estimation methods (DOE-NETL and fluid substitution). 24
Figure 10. DOE-NETL saline aquifer volumetric estimates for 23 Leduc Formation buildups (excluding hydrocarbon pools) in the study area. 25
Figure 11. Volumetric CO_2 capacity estimates from the Leduc Formation in the study area 26
Figure 12. Capillary pressure data of 20 MICP samples from the Ireton Formation: a) mercury-air system, and b) CO_2-brine system. 34
Figure 13. Photomicrographs of Ireton Formation lithofacies LF1 to LF3 37
Figure 14. Photomicrographs of Ireton Formation lithofacies LF4. 38
Figure 15. Photomicrographs of Ireton Formation lithofacies LF5 to LF7 39

Acknowledgements

David Herbers, Krista Beavis, and Tiffany Playter (Alberta Geological Survey [AGS]) are thanked for contributing to the stratigraphic model. Gil Abinal (AGS) is thanked for assisting with GIS work. Hugo Geng (formerly AGS) is thanked for assistance with the MICP data/analysis. We would like to give a special acknowledgment to the late Ken Potma of Calgary for meeting with AGS staff at the Core Research Centre for a day of learning. We benefited greatly from his vast knowledge of the Devonian carbonates of the Alberta Basin, especially the depositional and production history of the Leduc Formation buildups. We lament not being able to learn more from him in the coming years as Devonian carbonates are seeing renewed focus for various subsurface applications. Alex MacNeil and Matt Grobe (AGS) provided reviews that improved this contribution.

Abstract

Carbonate buildups of the Leduc Formation in central Alberta are an attractive target for CO_2 sequestration. The reefal buildups have been the focus of oil and gas production for many decades and are now mostly in a state of abandonment or enhanced recovery schemes. Despite the possibilities for sequestration in this formation, very little work has been done to quantify—even at a high level—the capacity of these buildups to sequester anthropogenic CO_2. While a small number of production-based estimates exist for some of the hydrocarbon pools, no estimations for the vast saline aquifer portions of the buildups are publicly available. This study provides a regional CO_2 capacity estimation for both the hydrocarbon-bearing and saline aquifer portions of the Leduc Formation in central Alberta—a formation comprising more than 23 buildups in the study area. Three methodologies are applied based on extensive stratigraphic mapping, petrophysical evaluation, and a stochastic approach to 3D property modelling in a multi-million-cell Petrel model: 1) a fluid substitution method involving hydrocarbon production databases, and volumetric approaches using the well-known U.S. Department of Energy and National Energy Technology Laboratory (DOE-NETL) methods for 2) hydrocarbon pools and 3) saline aquifers. Capacity estimations for the saline aquifer portion of the Leduc Formation total 1.66 gigatonnes of CO_2 (P_{50}). Aggregated mass estimates for the oil and gas pools are greater than 348.9 megatonnes of CO_2 (P_{50}; n=80), which is less than that estimated from the fluid substitution method at 817.5 megatonnes (n=72). The total P_{50} capacity estimate for the pools (DOE-NETL method) and saline aquifers within the study area is greater than 2.01 gigatonnes of CO_2. Given that this estimate far exceeds the annual emissions in Alberta at 260 megatonnes as of 2024, and the proximity of the buildups to industrial point-source emitters, the Leduc Formation has significant potential to contribute to Canada's net-zero emissions plans. Capacity estimations may also aid in evaluating the use of pore space in these buildups for purposes other than CO_2 sequestration, such as geothermal development, lithium recovery from brines, and water disposal. In addition to the Leduc Formation capacity estimation work, the Ireton Formation, which forms the caprock to the Leduc buildups, was regionally mapped and assessed from several cores for the purpose of caprock integrity assessment, which included X-ray fluorescence analysis. Twenty mercury injection capillary pressure tests were performed on seven lithofacies to assess the entry and threshold pressures to CO_2. The results show that theoretical CO_2 column heights across much of the study area may be significant.

1 Introduction

Alberta's portion of the Western Canada Sedimentary Basin is a mature hydrocarbon-producing basin that has significant potential to sequester CO_2 within deep saline aquifers and depleted oil and gas reservoirs, and through CO_2-enhanced oil recovery (CO_2-EOR) schemes. Currently, two carbon capture utilization and storage (CCUS) projects are actively emplacing CO_2 into the deep subsurface: 1) Shell Canada Energy's Quest project (dedicated sequestration), and 2) Enhance Energy Inc.'s Clive Field CO_2-EOR project. Beyond these current projects, Alberta has a long history of safe subsurface disposal of greenhouse gases in the form of acid gas (CO_2 + H_2S) disposal. Acid gas disposal has been successfully regulated by the Alberta Energy Regulator (AER) and its predecessors in Alberta since 1990 (Bachu et al., 2008). Considering that acid gas contains CO_2, studies undertaken by the Alberta Geological Survey (AGS) have used these disposal schemes as an analogue to safe and secure geological storage of CO_2 within Alberta (Bachu and Gunter, 2004).

Building on previous AGS basin-scale suitability studies that identified central Alberta as extremely suitable for CCUS (Bachu et al., 2000), this report highlights the results of work focused on the Leduc-Ireton storage complex in central Alberta (Figure 1), an area of critical importance due to the presence of numerous industrial CO_2 emitters located in Alberta's Industrial Heartland region. The report presents CO_2 storage capacity estimates within the Leduc buildups using two established methodologies arriving at a total CO_2 storage capacity of >2.01 gigatonnes. It also summarizes key lithological properties of the overlying Ireton Formation, which forms the primary seal for sequestered CO_2.

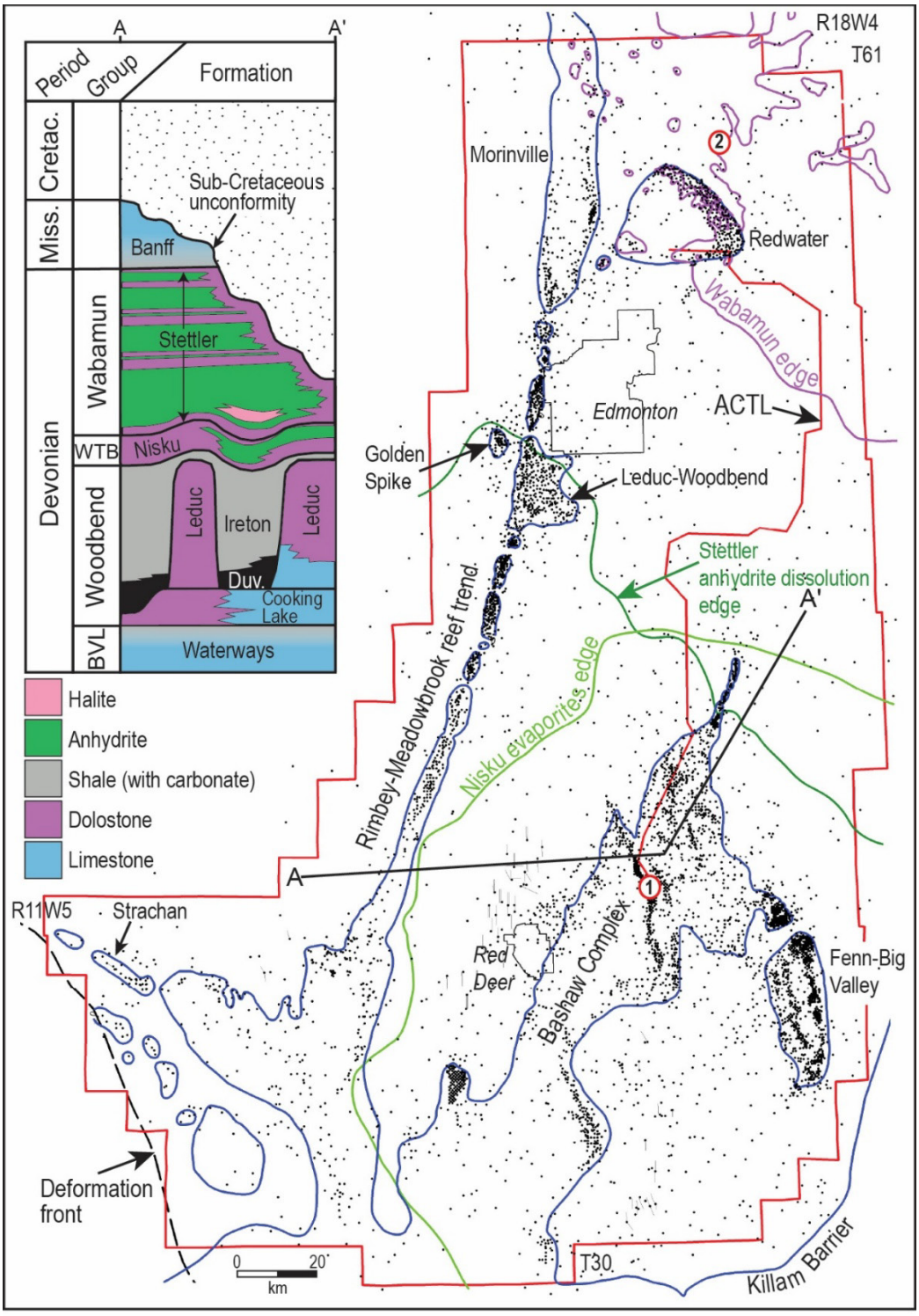


Figure 1. Location and simplified stratigraphic column for the study area in central Alberta. Leduc Formation buildup complexes are outlined in blue, modified from Switzer et al. (1994). 1) Enhance Energy Inc.'s Clive CO_2-EOR project. 2) Shell Canada Energy's Quest CO_2 sequestration project. Well control = 6004. Study area boundary in red. The edges of the Nisku and Stettler (Wabamun Group) anhydrite shown in light and dark green, respectively. The locations of Edmonton and Red Deer are outlined by thin black lines. Abbreviations: ACTL, Alberta Carbon Trunk Line; Miss., Mississippian; Cretac., Cretaceous; Duv., Duvernay; BVL, Beaverhill Lake; WTB, Winterburn.

2 Geological Setting

The Upper Devonian Leduc Formation is primarily dolostone formed after replacement of reefal and carbonate bank limestone deposits. The top of the Beaverhill Lake Group, represented by the interbedded carbonates and shales of the Waterways Formation, forms the base of the mapped units. The Waterways is overlain by the Cooking Lake Formation, a biostromal platform with an edge that is approximated by the western edge of the Rimbey-Meadowbrook reef trend (Figure 1). Detailed studies of the Leduc Formation include Andrichuck (1958), Klovan (1964), Mossop (1972), McGillivray and Mountjoy (1975), Stoakes and Wendte (1987), Stoakes (1992), Atchley et al. (2006) and Wong et al. (2016). Leduc reefs are buried in the subsurface from over 4500 m in the southwest near the Rocky Mountain deformation front (e.g., Strachan, Figure 1), to just less than 1000 m in the northeast (e.g., Redwater, Figure 1).

The paragenetic history of Leduc buildup deposits is well documented (e.g., Walls et al., 1979; Drivet and Mountjoy, 1997; Green and Mountjoy, 2005; Davies and Smith, 2006; Stacey et al., 2020). Post-depositional dolomitization was widespread and included several events (e.g., Mountjoy et al., 1999). Dolomitization is responsible for significant porosity enhancement and increased permeability which has implications for reservoir quality across the study area. The Leduc buildups and underlying Cooking Lake platform deposits are pervasively dolomitized along the Rimbey-Meadowbrook reef trend (Figure 1). Dolomitization within the Cooking Lake Formation extends slightly farther east of the trend and includes the far western margin of the Redwater buildup in the northern part of the study area (Figure 1); however, the bulk of the Redwater buildup is limestone. The Golden Spike buildup, located just west of the Rimbey-Meadowbrook reef trend also did not experience widespread dolomitization. The Bashaw and Fenn-Big-Valley buildup complexes in the southern part of the study area are variably dolomitized, with dolostones gradually changing to limestone with depth toward the base of the Leduc Formation—a pattern consistent with a seepage-reflux model of dolomitization as suggested by Potma et al. (2001).

Leduc buildups are overlain by a regional aquitard in the form of shale and argillaceous carbonates of the Ireton Formation (Figure 1). Detailed studies of the Ireton Formation include Oliver and Cowper (1963), Stoakes (1980), Switzer et al. (1994), Hearn et al. (2011) and Wong et al. (2016).

3 Methods and Results

3.1 Stratigraphic Mapping and Hydrocarbon Pools

Stratigraphic tops from wells (n=6004) of varying depths of penetration were mapped across the study area and provided most of the subsurface data for property modelling. Only 605 wells penetrated the entire Leduc Formation succession. The Leduc edges from Switzer et al. (1994) were used as a guide for mapping; however, they were updated in this study to reflect newer well control—the differences between the two are relatively minor.

The locations of Leduc Formation hydrocarbon pools from AER databases were used to constrain well data inside and outside of pool boundaries for the purposes of CO_2 capacity estimations from hydrocarbon pools versus saline aquifers (Figure 2).

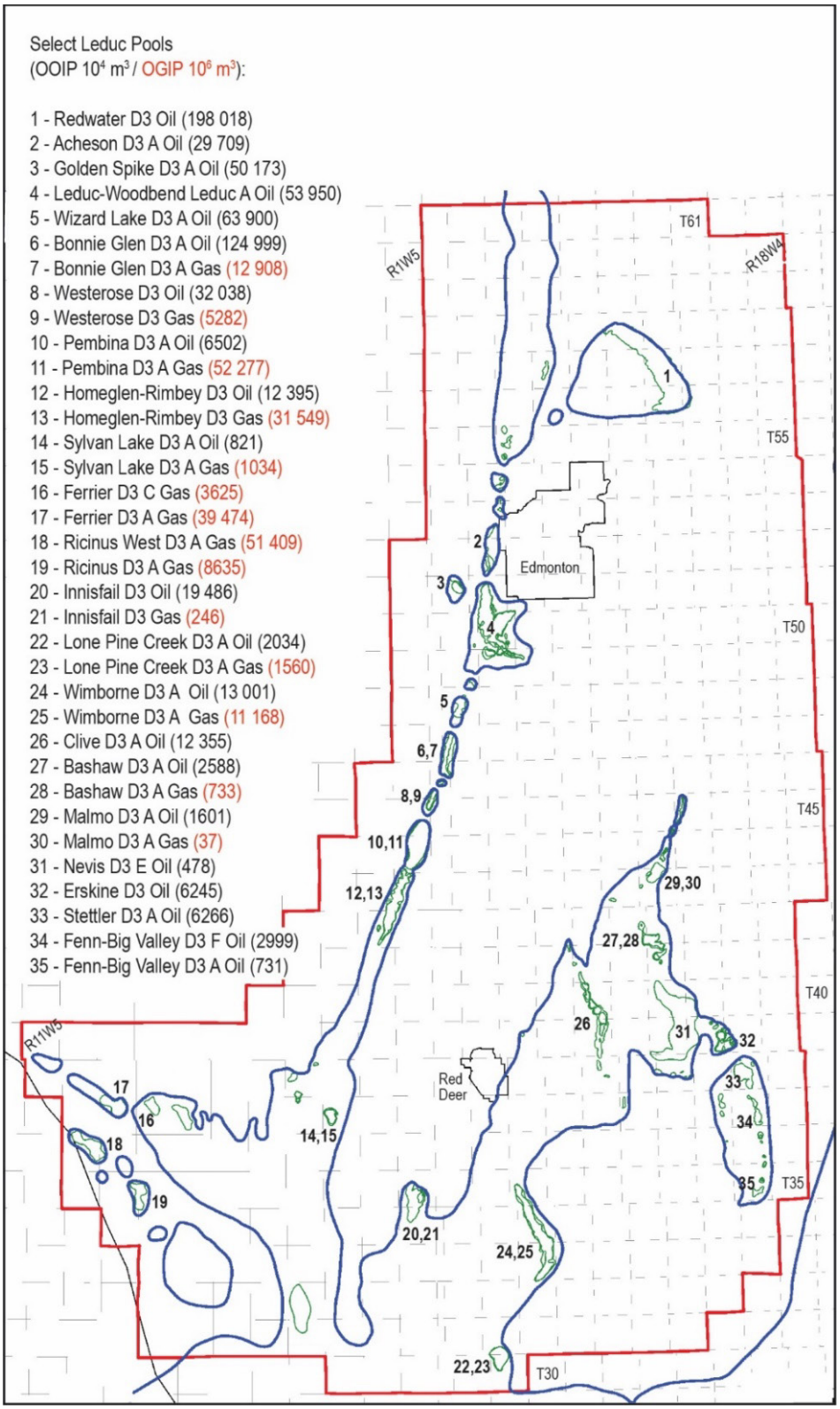


Figure 2. Location of select hydrocarbon pools (outlined in green) and estimated resources in the Leduc Formation buildup complexes in central Alberta. Leduc Formation buildup complexes are outlined in blue, modified from Switzer et al. (1994). Abbreviations: OOIP, original oil in place; OIGP, original gas in place.

3.1.1 Leduc-Ireton Storage Complex

The thickness of the Leduc Formation varies considerably across the study area (Figure 3). From well control, minimum thickness is just over 20 m and maximum thickness reaches 321 m, averaging 181 m (n=323). Most of the buildups have relatively steep margins that appear even steeper when vertically exaggerated (Figure 3, Acheson). Some of the isolated buildups along the Rimbey-Meadowbrook reef trend appear to have more gradual transitions from the edge of the buildup toward maximum buildup thickness (Figure 3, Leduc-Woodbend and Golden Spike buildups).

Many of the larger Leduc buildups have thickness trends that reveal lithologically competent margins relative to interiors that have experienced compaction (see Hearn et al., 2011). Hydrocarbon pools are often located within the buildup margins, in part due to favourable rock properties as well as stratigraphic trapping associated with a shallowly dipping Paleozoic succession toward the southwest.

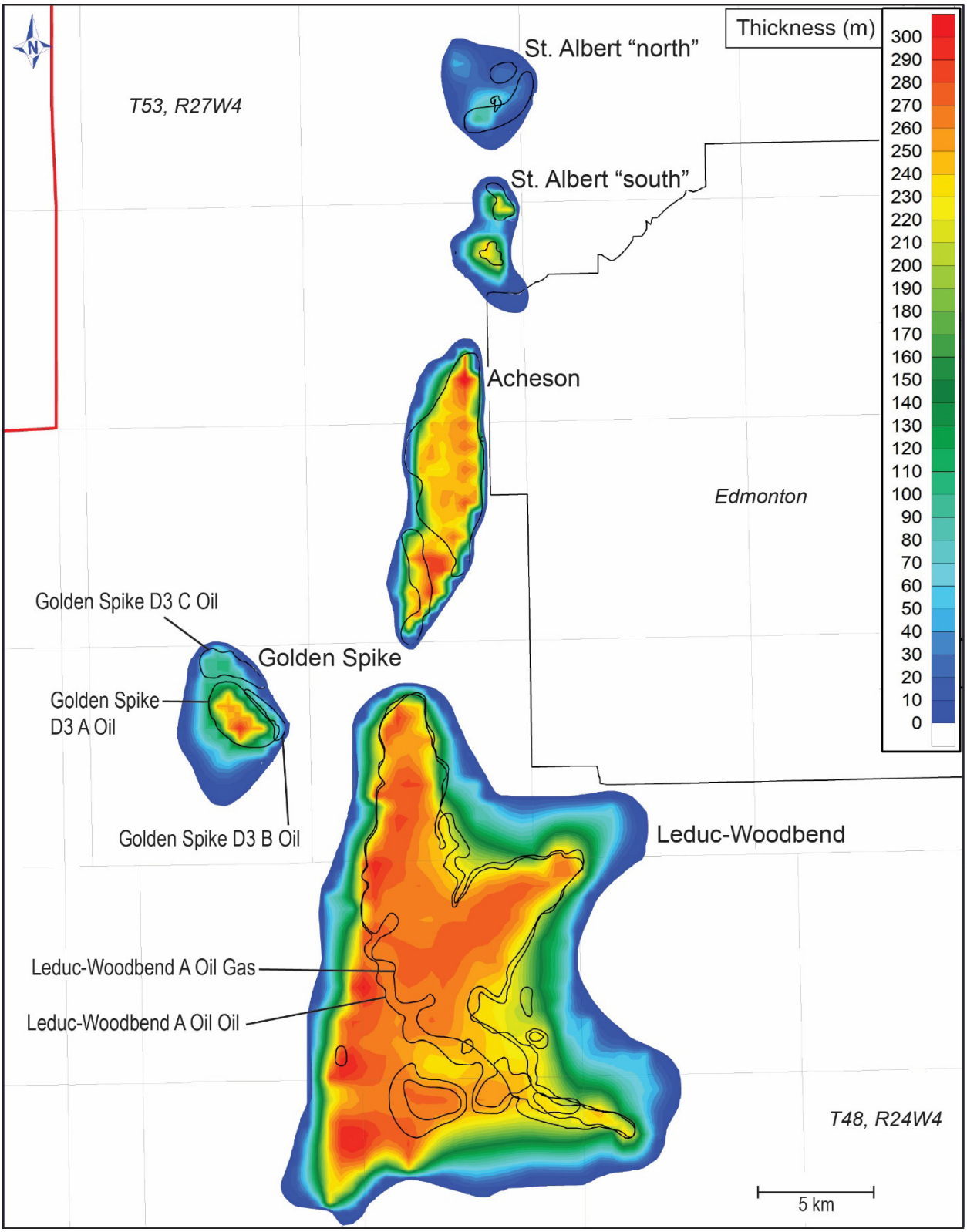


Figure 3. Variation in Leduc Formation buildup thicknesses near the city of Edmonton. Hydrocarbon pools are shown (in black) corresponding to various buildup levels (e.g., Golden Spike). Maximum thickness is 288 m on the southern end of the Leduc-Woodbend buildup.

The shales and argillaceous carbonates of the Ireton Formation are thickest in off-buildup positions as basin-filling strata, and thin considerably over the Leduc buildups (Figure 4). Ireton thickness over the buildups also generally decreases toward the southern parts of the study area. Ireton non-deposition was noted in several wells over buildups in the southern part of the study area (Figure 4). Post-depositional compaction of buildup interiors is evidenced by the location of non-depositional trends in the Ireton Formation over the buildup interiors (Figure 4). For example, in the case of the Bashaw complex, the Ireton was not deposited over parts of the buildup interior, whereas the present-day (subsurface) elevated buildup margins sit above the buildup interior. This indicates that the interior was closer to sea level than the buildup margin during deposition of the Ireton shales but later subsided during burial compaction (also see Hearn et al., 2011).

The Ireton Formation includes the Camrose Member (see Stoakes, 1980), formed of a biostromal carbonate near the top of the Ireton. This unit is mostly constrained to the eastern half of the study area, being deposited over the Bashaw complex, and thinning west of this buildup. Over the Leduc buildups the Camrose can be very difficult to differentiate from the overlying carbonates of the Nisku Formation (Gilhooly, 1987). For the purposes of this study, where the Camrose has been mapped over the Leduc buildups, it is not included in the thickness of the Ireton Formation as it is not considered part of the caprock succession.

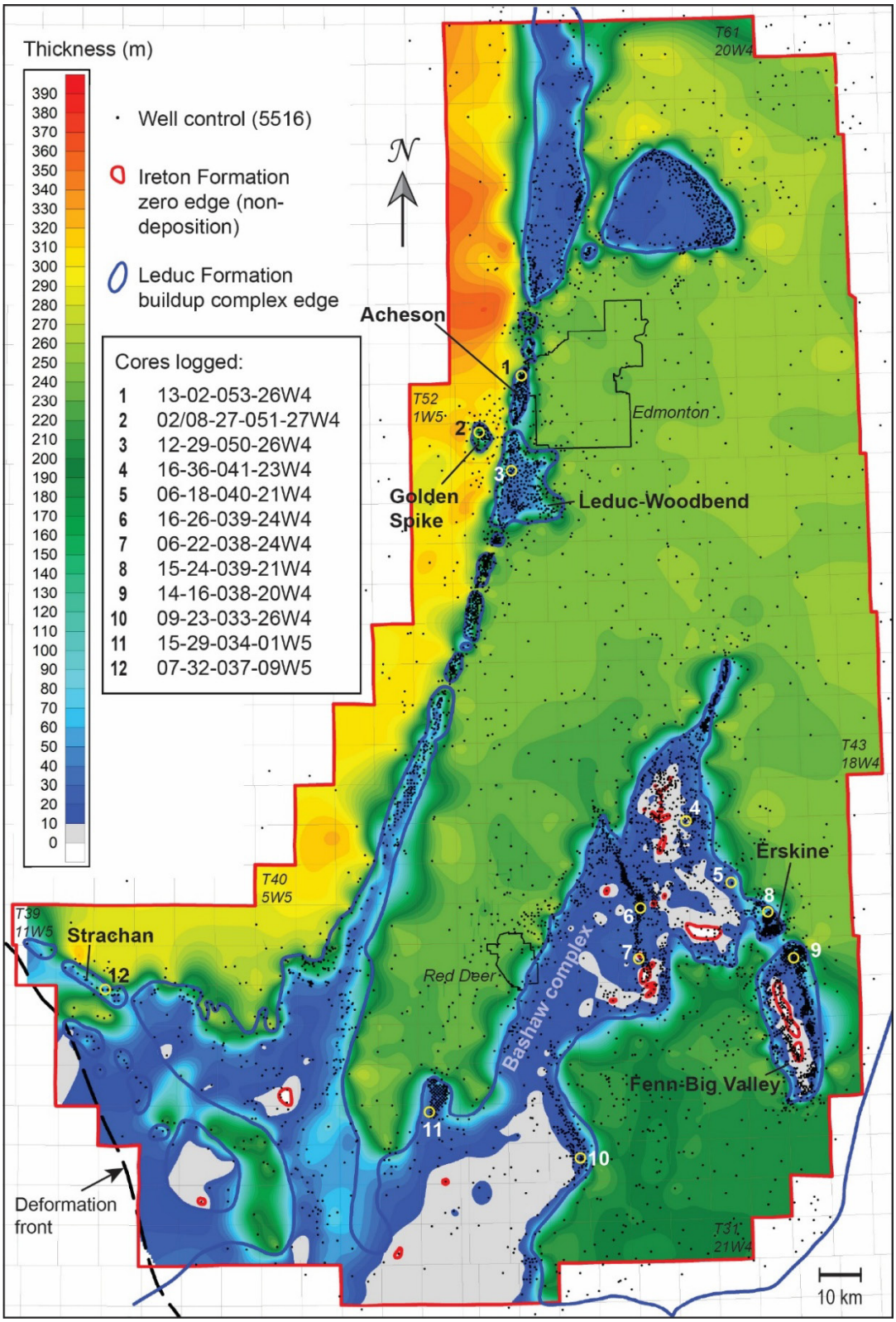


Figure 4. Thickness of the Ireton Formation (caprock) within the study area. Areas shaded in light grey are interpreted as having an Ireton thickness below 10 m. The location and buildup name over which the 12 Ireton Formation cores were reviewed for lithofacies and sampled for mercury injection capillary pressure analysis are shown.

3.2 Stratigraphic Modelling

The framework of the property model was built using the stratigraphic tops from the mapping discussed above, interpreted depositional edges or erosional inliers, and version 3 of the Geological Framework of Alberta. A 100 m horizontal grid cell size was used to better capture the geometry of the Leduc buildups, including local variations in relief. This resolution is finer than the 500 m cell size used in the Geological Framework of Alberta model.

The stratigraphic surfaces were modelled in SLB Petrel using the convergent interpolation or conformal gridding algorithms. The base (Beaverhill Lake Group surface) and top (sub-Cretaceous unconformity) of the model were created first, then the remaining surfaces were built from the deepest upwards (Table 1).

Figure 5 shows an isometric view of the surfaces from the top of the Leduc Formation downwards. The compacted lagoon characteristics of the larger buildups are clearly visible. Each zone was initially created as a single layer in the model. The Leduc model zone was discretized to 5 m thick layers for 3D modelling, to better portray the vertical variability within the Leduc Formation.

Table 1. Petrophysical methods and calibration parameters.

Property	Parameter	Units	Leduc	Ireton
V_{SH}	V_{SH} Method	-	Stieber	Stieber
	GR_{CLEAN}	GAPI	5	5
	GR_{SHALE}	GAPI	130	130
$PhiT_{LS}$	$PhiT_{DEN}$ Method	-	Neutron-density	-
	ρ_{FL}	kg/m^3	1000	-
	ρ_{MA}	kg/m^3	2710	-
$PhiT_{DL}$	$PhiT_{DEN}$ Method	-	Density	-
	ρ_{MA}	kg/m^3	2870	-
	ρ_{FL}	kg/m^3	1000	-
	$PhiT_{DT}$ Method	-	Sonic	-
	DT_{MA}	µs/m	144	-
	C_EXP	-	0.67	-
PhiT	Method	-	Lith-weighted avg of $PhiT_{DL}$, $PhiT_{LS}$	-
PhiE	Method	-	Shale-reduced	-
S_W	Method		Archie	-
	a		1	-
	m		2	-
	n		2	-
	R_{w_fixed}	ohmm	0.1	

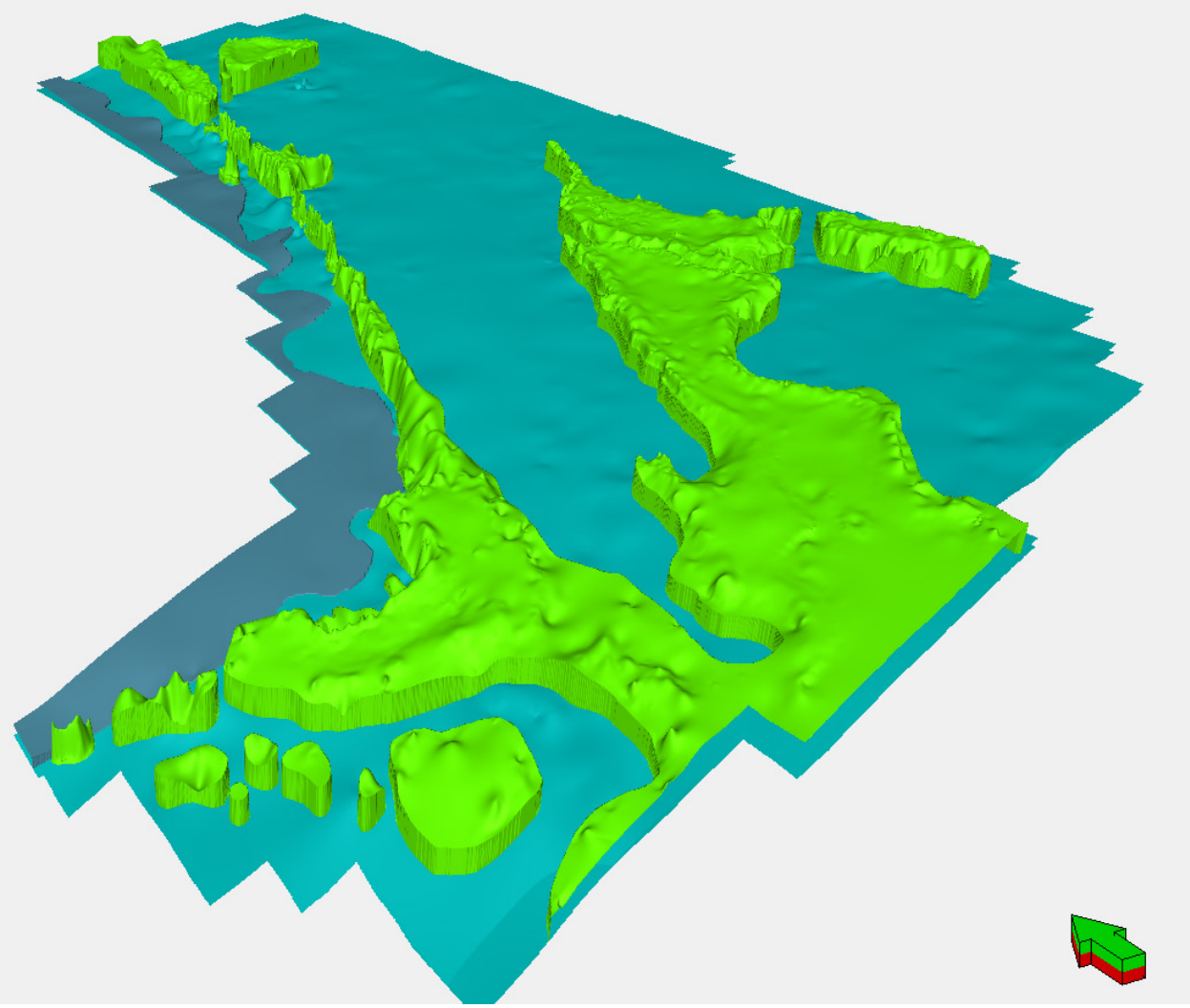


Figure 5. An isometric view of the geological model horizons from top Leduc horizon down. Leduc surface: green; Majeau Lake: dark blue; Cooking Lake: light blue-green. Vertical exaggeration = 25X.

3.3 Petrophysical Evaluation

Petrophysical well log analysis was performed on the Leduc and Ireton formations. In the Leduc Formation, limestone and dolostone lithology, shale volume (V_{SH}), total porosity (PhiT), effective porosity (PhiE), and matrix lithology were estimated in 136 wells with full penetration of the formation and 805 wells with partial penetration. The Archie water saturation (S_W) was calculated in 872 wells where data allowed; however, the results contained a high degree of uncertainty.

Leduc Formation buildups are widely but not completely dolomitized, which is known to influence rock properties such as porosity and permeability (Amthor et al., 1994). As such, the lithology was estimated to improve the quality of the estimation of rock properties. A two end-member (limestone and dolostone) lithology was assumed for the rock matrix (shale content is negligible), which is supported by well log values and core data. The limestone and dolostone end-members were defined along an axis of neutron-density separation, allowing for estimation of a limestone-to-dolomite ratio (MA_{LS}) for the matrix:

$$ND_{sep} = NPDL - DPDL \quad (1)$$

$$MA_{LS} = \frac{\left(ND_{sep_{DL}} - ND_{sep}\right)}{\left(ND_{sep_{DL}} - ND_{sep_{LS}}\right)} = \frac{\left(0 - ND_{sep}\right)}{\left(0 - (-0.11)\right)} = \frac{ND_{sep}}{-0.11} \quad (2)$$

where ND_{sep} is the log-derived neutron-density separation at a given depth value, NPDL is the neutron porosity in dolostone units, DPDL is the density porosity assuming dolostone matrix, ND_{sepDL} and ND_{sepLS} are the positions of dolostone and limestone endmembers, respectively, in the neutron-density separation domain. The limestone-to-dolomite ratio was bound between 0 and 1. While gas and shale content introduce error into neutron-density lithology estimation, these two factors were judged to be minor.

In the Ireton Formation, shale volume (V_{SH}) was estimated in 2633 wells using both a Leduc Formation and Ireton Formation top. V_{SH} was estimated non-linearly from gamma-ray (GR) logs using a Stieber (1970) transform of the linear GR V_{SH} index:

$$IGR = \frac{(GR - GR_{clean})}{(GR_{shale} - GR_{clean})} \quad (3)$$

$$V_{SH} = \frac{IGR}{3 - 2IGR} \quad (4)$$

where IGR is the linear gamma-ray V_{SH} index, GR is the log gamma-ray value, GR_{clean} is the GR value of clean (0% shale) rocks, and GR_{shale} is the GR value of 100% shale.

Shale volume was estimated for the Leduc and Ireton formations together because x-ray diffraction (XRD) calibration data was sparse for both formations and the presence of shale is rare in the Leduc Formation, limiting the feasibility of determining an adequate GR_{shale} value from the Leduc GR distribution. GR_{clean} and GR_{shale} were set to 5 and 130 GAPI, respectively. These values were adjusted to optimize the fit between calculated V_{SH} and core XRD results in seven wells. Table 1 summarizes methods and calibration parameters. Calibration data were sourced from AER databases and included porosity, water saturation, and XRD mineralogy from core.

Two porosities were output from this work: total porosity (PhiT) and effective porosity (PhiE). Total porosity was separately estimated for limestone-dominated and dolostone-dominated rocks and calibrated to core data. Limestone porosity ($PhiT_{LS}$) was calculated using a neutron-density method. Dolostone porosity ($PhiT_{DL}$) was calculated as density porosity, except where the density correction (D_{RHO}) flag is greater than 150; in those cases, sonic-log-derived porosity was used, although it has recognized limitations in vuggy lithologies..

$$PhiT_{DEN_{DL}} = \frac{(\rho_{ma} - \rho_b)}{(\rho_{ma} - \rho_f)} = \frac{(2870\ kg/m^3 - RHOB)}{(2870\ kg/m^3 - 1000\ kg/m^3)} \quad (5)$$

$$PhiT_{SON_{DL}} = C\frac{(\Delta t - \Delta t_{ma})}{\Delta t} = 0.67\frac{(\mathrm{DT} - 144\ \mu s/m)}{144\ \mu s/m} \quad (6)$$

where ρ_{ma} is dolostone matrix density, ρ_b is the formation bulk density (RHOB log), ρ_f is the density of water, Δt is the sonic travel time (DT log), Δt_{ma} is travel time of the matrix, and C is a variable meant to account for fluid properties and is in the range of 0.625 to 0.70 for most reservoirs.

The total porosity for limestone ($PhiT_{LS}$) was calculated using a neutron-density porosity method:

$$PhiT_{DEN_{LS}} = \frac{(\rho_{ma} - \rho_b)}{(\rho_{ma} - \rho_f)} = \frac{(2710\ kg/m^3\ -\ RHOB)}{(2710\ kg/m^3 - 1000\ kg/m^3)} \quad (7)$$

$$PhiT_{LS} = \sqrt{\frac{NPHI_{LS}{}^2 + PhiT_{DEN_{LS}}{}^2}{2}} \quad (8)$$

The final PhiT was calculated as a lithology-weighted average of $PhiT_{LS}$ and $PhiT_{DL}$ and was bound between 0 and 0.25 v/v:

$$PhiT\ =\ (PhiT_{LS} * MA_{LS})\ +\ (PhiT_{DL} * (1\ -\ MA_{LS})) \quad (9)$$

Effective porosity was calculated by subtracting clay-bound water (CBW) from PhiT, assuming shale porosity of 0.15 v/v, and limited at 0:

$$PhiE =\ PhiT\ -\ CBW = PhiT - (V_{sh} * 0.15) \quad (10)$$

The effective porosity (PhiE) is not a true effective porosity but instead provides an estimate of non-shale porosity. Usually, PhiE is similar to total porosity (PhiT) because Leduc Formation carbonates do not contain much shale. True effective porosity is difficult to estimate in carbonates without information on facies pore-throat characteristics, pore-network connectivity, and capillary pressure behaviour.

3.4 Property Modelling

The Cooking Lake Formation top surface is the base of the Leduc Formation property model; the top Leduc Formation surface is the top of the model. Each cell in the property model is 100 m by 100 m by (nominally) 5.0 m in size. There are 44.4 million active cells in the model.

3.4.1 Hydrocarbon-Water Contacts

There are differences in the way that CO_2 sequestration capacity is estimated in hydrocarbon pools versus saline aquifers. For this reason, it was necessary to distinguish between the two in the property model; the hydrocarbon zones were distinguished from the aquifers using contact points in 1885 evaluated wells (Figure 6).

A surface was interpolated from the hydrocarbon-water contact points using the minimum curvature algorithm in Petrel. The Leduc pool outlines which are administrative boundaries assigned by the regulator were used as the surface boundary, then the surfaces were extended beyond the administrative pool boundaries to the geological buildup edges, where necessary, to avoid artificial discontinuities. This process produced a discontinuous surface with mostly near-flat portions within each defined Leduc pool. This hydrocarbon-water contact surface is slightly tilted in some pools and not entirely flat in others

where local lithology and aquifer drive have large effects. The surface was used to divide the cells within the property model into hydrocarbon and aquifer zones. Figure 7 shows an isometric view of the fluid model and herein ‘saline aquifer’ refers to the portions that sit below the hydrocarbon zones and within the Leduc buildup edges shown previously in Figure 1.

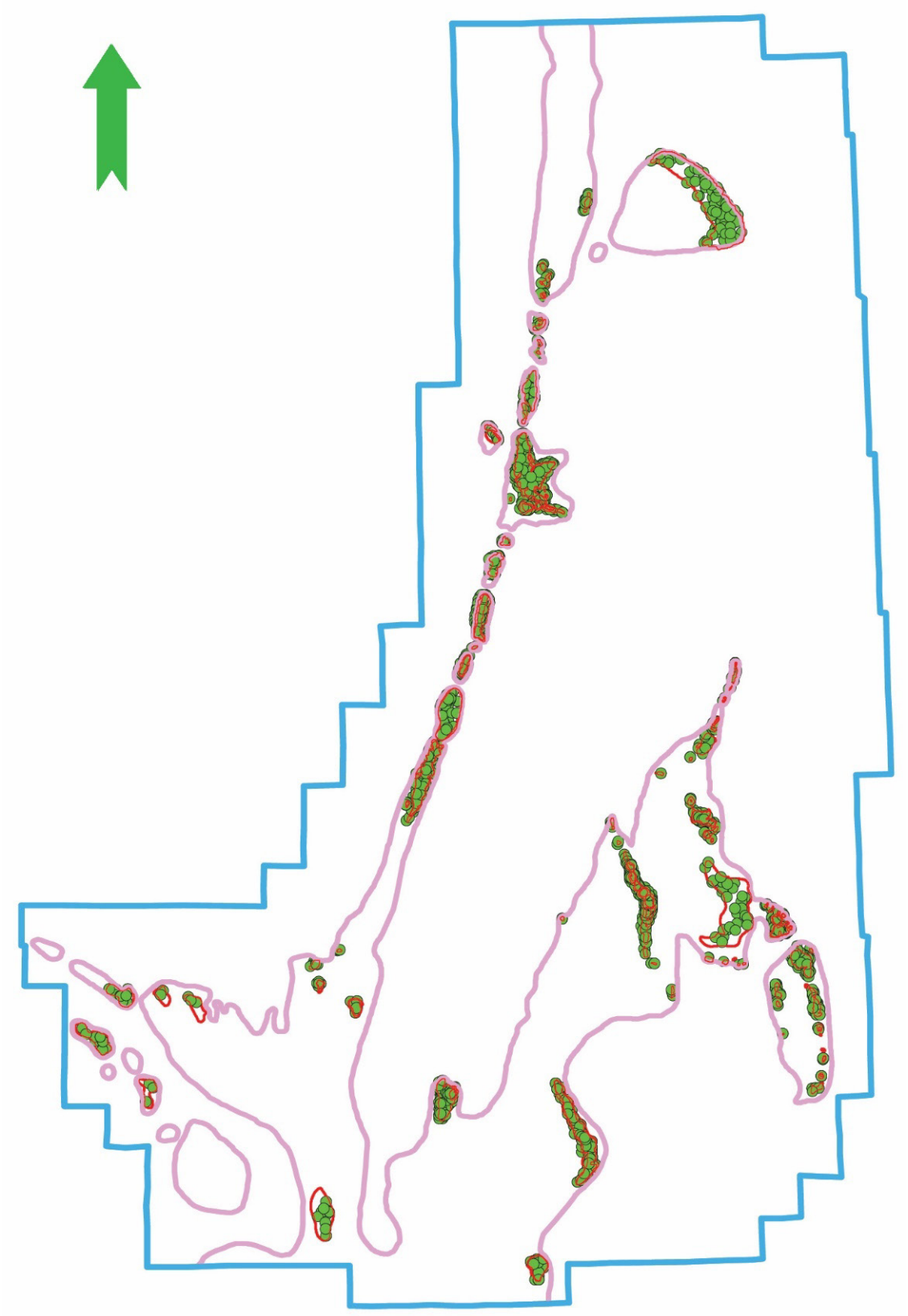


Figure 6. Map view of the hydrocarbon-water contact data points (green), Leduc Formation pool outlines (red), geological model area (blue), and Leduc buildup outlines (pink).

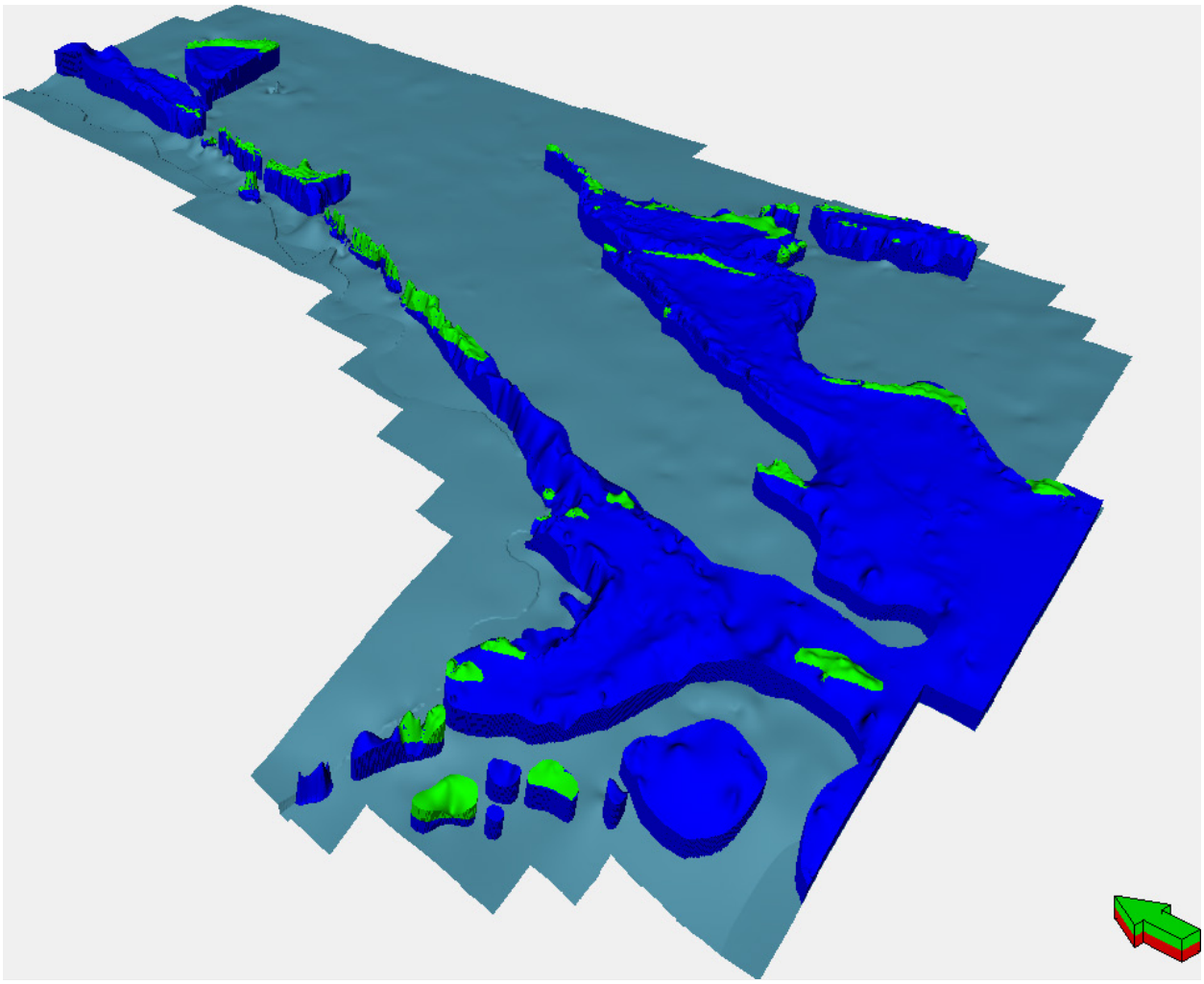


Figure 7. An isometric view of the hydrocarbon-water zone model within the Leduc Formation. Green: hydrocarbon zone; blue: water zone. Vertical exaggeration = 25X.

3.4.2 Upscaling 3D Properties

The upscaling process averages the log readings within a modelling cell to a single mean value. In the property model, with 5 m vertical cell sizes, the arithmetic mean of the log values was used. The mean of the properties is not changed by the arithmetic averaging used in this model, only the variances are affected. Table 2 shows summary statistics for the upscaled cells of the four properties. Effective porosity was not modelled for the non-hydrocarbon model cells; total porosity was used in these cells and the difference between total and effective porosity shown in Table 2 is a function of the different spatial distributions.

Table 2. Summary statistics for upscaled 3D properties in the property model.

Property	Unit	Zone	Count	Mean	Std Dev	Min	Max
Total porosity	Fraction	All	11209	0.075	0.040	0.000	0.250
Effective porosity	Fraction	Hydrocarbon	2552	0.093	0.040	0.000	0.241
Water saturation	Fraction	Hydrocarbon	2310	0.315	0.253	0.023	1.000
Matrix limestone	Fraction	All	10949	0.236	0.306	0.000	1.000

3.4.3 Pressure and Temperature

Reservoir conditions have significant impact on the amount of a fluid that can be contained in pore space. The Leduc Formation within the study area varies from a depth of 900 m to almost 5000 m; over this wide range there are major differences in pressure and temperature. The varying reservoir conditions were modelled by extracting well test data from an AER database for wells with tests within the Leduc Formation. This source is the same as for AER/AGS Digital Data 2021-0028 (Brinsky, 2023) but with pressure in units of kPa instead of hydraulic head in metres; and temperature data are also included. The data were clipped to the study area and the remaining 117 pressure and 91 temperature data points along with test depth were used to calculate gradients. These point data were upscaled to a single-layer version of the property model. Table 3 shows summary statistics of the upscaled gradient properties.

Table 3. Summary statistics for upscaled 2D properties in the property model.

Property	Unit	Count	Mean	Std Dev	Min	Max
Pressure gradient	kPa/m	99	8.48	0.81	6.92	9.70
Temperature gradient	°C/km	77	33.1	4.9	17.6	43.3

3.4.4 Quantifying Uncertainty

Subsurface modelling relies on sparse data due to the expense of collecting subsurface data. In this modelling work, the data used are all from industry-submitted wireline logs and tests and so no additional information could be gathered. In cases like this it is important to properly quantify the uncertainty in the model to account for the wide range of possible outcomes that are consistent with the data.

3.4.4.1 Spatial Variables

The six spatial variables (total porosity, effective porosity, water saturation, matrix limestone fraction, pressure gradient, and temperature gradient) were simulated using a geostatistical, variogram-based method. The method used was Gaussian random function simulation (GRFS) in Petrel. This method produces realizations that honour the input data and reproduce the univariate distributions and spatial structure (i.e., variograms) of the input. For this work, 20 simulated realizations were used to quantify the range of the spatial uncertainty. It was found through this work that the Archie-calculated Sw did not produce reliable results. Water saturation in the aquifer zones was therefore assigned as ‘1’. To assign a Sw in the hydrocarbon zones that was deemed more accurate than what was calculated, the AER database of water saturation for the different pools was used. The Sw in the database, amassed over several years at the regulator, considered production history and other data and is deemed reliable. To correct the Archie-calculated Sw, the entire distribution of simulated data in each pool was scaled to match the target mean value from the AER database. This resulted in Sw values with higher confidence given the known pool production history (i.e., a lower water saturation than that calculated with the Archie method), while at the same time maintaining the shape of the data distribution.

The 2D variables (pressure and temperature gradients) were also modelled with GRFS but in the one-layer, 2D model. The gradient values at every (x, y) location in the model were multiplied by the depth of each cell at that location to calculate pressure and temperature; the uncertainty in the pressure and temperature values are quantified by the uncertainty in the corresponding gradients.

3.4.4.2 CO_2 Density

The density of CO_2 is a critical parameter in storage capacity estimation because it varies strongly with temperature and pressure and changes phase depending on the in-situ conditions. The critical point of pure CO_2 is approximately 304 K and 7377 kPa (Span and Wagner, 1996). Across most of the Leduc-Ireton storage complex, modelled reservoir pressure and temperature indicate that injected CO_2 would be stored under supercritical conditions. A portion of the Redwater buildup is shallow enough that some

model realizations fall below the CO_2 critical pressure and/or temperature. Approximately 580 000 cells, representing 1.3% of the model have a non-zero probability of subcritical CO_2 density. Because the remaining 98.7% of model cells are predicted to be above the critical point, this study assumes supercritical CO_2 conditions for regional-scale capacity estimation.

To quantify the CO_2 density in the property model in a computationally efficient workflow, a set of equations fitted by Bahadori et al. (2009) were used. This approach is simpler to implement in a workflow than solving the equations of state from Span and Wagner (1996). Checks at several locations confirm that the results are within acceptable levels of uncertainty between the two methods.

3.5 CO_2 Capacity Estimation

For this study, we employed three methodologies to determine CO_2 capacity estimates for the Leduc Formation: 1) the fluid substitution method, 2) the United States Department of Energy-National Energy Technology Laboratory (DOE-NETL) saline aquifer method, and 3) the DOE-NETL oil and gas method. The saline aquifer methodology is applied to the formation in areas below the reservoirs defined by hydrocarbon-water contacts as they existed at discovery.

3.5.1 Fluid Substitution

The fluid substitution method is a volumetric approach used to estimate the storage capacity within hydrocarbon pools. The method uses production databases (production data required by the AER from oil companies in Alberta) to calculate the volume of CO_2 that could theoretically replace the volume of oil and gas that has been extracted from pools under reservoir conditions (e.g., pressure and temperature), and the filling up of that reservoir to initial pressure at discovery (see Haagsma et al., 2020). As such, the total volume in each of the Leduc Formation buildups is equivalent to the sum of CO_2, oil, and gas above the oil-water contact (OWC). In this case, water (brine) is not accounted for in the fluid substitution equation, shown as:

Total volume of oil in a given reef above OWC = **Volume of CO_2** + **Volume of gas** + **Volume of oil**

$$N^*B_{o,i} = [G_{CO_2}]^*B_{g,CO_2,p} + B_{g,p}{}^* \left\{ [N^*R_{so,i} - [(N - N_p)^*R_{so,p}] - G_p \right\} + [(N - N_p)]^*B_{o,p} \quad (11)$$

where N is the original oil in place (OOIP) in stock barrels (STB), $B_{o,i}$ is the oil formation volume factor at initial pressure, G_{CO_2} is the CO_2 volume at surface conditions, $B_{g.CO2,p}$ is the CO_2 formation volume factor at storage pressure, $B_{g,p}$ is the associated gas formation volume factor at storage pressure p in reservoir cubic feet per standard cubic foot (rcf/scf), $R_{so,i}$ is the solution-gas-oil ratio at initial pressure in standard cubic feet/STB, N_p is the cumulative volume of oil produced from the reservoir up until abandonment pressure p in STB, $R_{so,p}$ is the solution-gas-oil ratio at storage pressure in standard cubic feet/STB, G_p is the cumulative volume of associated gas produced up to abandonment pressure p in standard cubic feet, and $B_{o,p}$ is the oil formation volume factor at storage pressure in reservoir barrel/STB.

For gas pools without associated oil, the equation can be simplified (following Haagsma et al., 2020) to:

$$\left[G_p - \left[N_p * R_{so,i}\right]\right] * B_{g,p} = G_{CO_2} * B_{g,CO_2,p} \quad (12)$$

For oil, associated oil and gas pools, and non-associated gas pools, CO_2 volume estimates were derived using these equations. Limitations of the fluid substitution approach include: 1) it does not account for produced water (Haagsma et al., 2020), and 2) it does not account for encroaching water and its pressure maintenance effect. Another important limitation to the use of the fluid substitution method is abandonment pressure—current conditions are not fully understood in the Leduc Formation pools as many have been abandoned for decades. Furthermore, the Leduc Formation is known to have strong aquifer support (in most cases) provided by the underlying Cooking Lake Formation aquifer (e.g., Bachu et al., 2011). This aquifer support would act to re-pressurize the Leduc hydrocarbon voidance over time.

3.5.1.1 Reservoir Pressure, Volume, and Temperature

Four pools were found to have pressure, volume, and temperature (PVT) data for their fluids. From these, comparative plots of the oil formation volume factor (B_o), gas formation volume factor (B_g), and the solution-gas-oil ratio (R_s) versus pressure provided a representation of the average fluid characterization within the Leduc Formation reservoirs.

The fluid substitution method assumes filling up of the depleted reservoir with CO_2 up to initial reservoir pressures. Many of the Leduc pools were initially underpressured by appoximately 15–30% relative to hydrostatic pressure; however, a few deeper pools were initially overpressured. Capacity estimates are therefore based on the initial reservoir pressure at discovery, evaluated relative to the hydrostatic pressure expected at that depth using a gradient of 10.2 Kpa/m. Ostensibly, these initial reservoir pressures are those that allowed for the accumulation of hydrocarbons beneath the Ireton Formation seals and are therefore considered safe charge levels.

3.5.1.2 CO_2 Properties

For the fluid substitution method, CO_2 density (at supercritical state) and the formation volume factor were obtained using initial pressures and isothermal conditions through the National Institute of Standards and Technology website: Thermophysical Properties of Fluid Systems (nist.gov).

3.5.1.3 Leduc Formation Hydrocarbon Pools

Table 4 provides the Leduc Formation oil and gas pools in the study area with ultimate recoveries greater than 10 000 10^3m^3, including original oil in place (OOIP) and original gas in place (OGIP). Table 5 provides non-associated gas pool ultimate recoveries greater than 1000 10^6m^3. Additional tables for oil and gas, and non-associated gas pools with ultimate recoveries greater than 100 10^3m^3 (n=58) and 100 10^6m^3 (n=14), respectively, are provided in Appendix 1.

Table 4. Oil and gas reservoirs with ultimate recoveries greater than 10 000 10^3m^3.

Pool Name	Area	OOIP	OGIP	Ultimate Recovery
	(ha)	(10^3m^3)	(10^6m^3)	(10^3m^3)
Acheson D-3 A	2084.0	29 708.9	77.0	21 549.4
Bonnie Glen D-3 A	2759.0	124 998.6	0.0	82 749.1
Golden Spike D-3 A	596.0	50 173.4	0.0	29 060.3
Innisfail D-3-Oil	3136.0	19 486.4	0.0	13 601.5
Leduc-Woodbend Leduc A	8828.0	53 950.0	0.0	40 224.9
Redwater D-3	17 236.0	198 018.3	0.0	134 627.2
Westerose D-3	848.0	32 037.6	0.0	23 707.8
Wizard Lake D-3 A	1177.0	63 899.6	0.0	54 186.8
Total	36 664.0	572 272.8	77.0	399 752.0

Table 5. Non-associated gas reservoirs with ultimate recoveries greater than 1000 10^6m^3.

Pool Name	Area	OGIP	Ultimate Recovery
	(ha)	(10^6m^3)	(10^6m^3)
Ferrier D-3 A	2011.0	39 474.0	37 500.0
Ferrier D-3 C	1025.0	3625.0	2030.0
Harmattan-Elkton D-3 A	4613.0	10 833.0	3250.0
Ricinus D-3 A	1613.0	8635.0	3454.0
Ricinus D-3 B	64.0	2144.0	1822.0
Ricinus West D-3 A	2565.0	51 409.0	48 839.0
Ricinus West D-3 B	32.0	7222.0	6500.0
Total	11 923.0	123 342.0	103 395.0

3.5.2 Results: Fluid Substitution in Leduc Formation Hydrocarbon Pools

The fluid substitution method results for CO_2 storage in oil and gas reservoirs with ultimate recoveries greater than 10 000 10^3m^3 are presented in Table 6, and for non-associated gas reservoirs with ultimate recoveries greater than 1000 10^6m^3, in Table 7. Mass estimates for oil and gas, and non-associated gas pools with ultimate recoveries greater than 100 10^3m^3 and 10 10^6m^3, respectively, are provided in Appendix 2.

Table 6. Fluid substitution results (CO_2 volume and mass at storage pressure) for Leduc Formation oil and gas reservoirs with ultimate recoveries greater than 10 000 10^3m^3.

Pool Name	10^3m^3	Tonnes
Acheson D-3 A Oil	344 524.3	218 383 623.9
Bonnie Glen D-3 A	111 034.0	83 423 831.0
Golden Spike D-3 A	168 790.9	121 608 758.8
Innisfail D-3-Oil	25 704.0	21 276 779.0
Leduc-Woodbend Leduc A	44 236.0	29 957 203.0
Redwater D-3	95 061.3	15 304 861.5
Westerose D-3	34 229.0	26 546 381.0
Wizard Lake D-3 A	62 542.0	46 989 877.0
Total	888 121.5	563 491 315.2

Table 7. Fluid substitution results (CO_2 volume and mass at storage pressure) for Leduc Formation non-associated gas reservoirs with ultimate recoveries greater than 1000 10^6m^3.

Pool Name		10^6m^3	Tonnes
Ferrier D-3 A		60 748.6	59 243 899.7
Ferrier D-3 C		3331.0	3 248 477.0
Harmattan-Elkton D-3 A		8612.9	7 765 841.2
Ricinus D-3 A		7065.9	6 654 947.4
Ricinus D-3 B		3778.5	3 550 867.1
Ricinus West D-3 A		86 504.1	83 153 834.4
Ricinus West D-3 B		9402.1	9 104 954.8
	Total	179 443.2	172 722 821.6

3.5.3 DOE-NETL Methods

The DOE-NETL methodologies for oil and gas reservoirs are described in Goodman et al. (2011) and refined in Goodman et al. (2016). The DOE-NETL methodology uses volumetric equations to calculate the storage capacity of a reservoir.

3.5.3.1 Capacity Estimates

The equations for the saline aquifer and oil/gas methods, as applied here, are shown below:

$$G_{CO_2} = A_t \cdot h_g \cdot \varphi_t \cdot S_w \cdot \rho_{CO_2} \cdot E_{saline} \quad (13)$$

$$G_{CO_2} = A_n \cdot h_n \cdot \varphi_n \cdot (1 - S_w) \cdot \rho_{CO_2} \cdot E_{oil/gas} \quad (14)$$

Both of the methods require parameters including area, thickness, porosity, saturation, CO_2 density, and an efficiency factor. Table 8 lists the sources of values for these parameters and factors in each of the two methods.

Table 8. Terms in the capacity estimate equations as used in this work.

Term	Saline Aquifer Method	Oil/Gas Method	Source
Area, A	Buildup area	Pool area	Polygons
Thickness, h	Gross thickness	Net thickness	Stratigraphic model
Porosity, φ	Total porosity	Net porosity	Property model; shale-reduced porosity used for oil/gas method
Saturation, Sw or 1-Sw	Water saturation	Hydrocarbon saturation	Set to 1.0 for saline aquifer method; from property model then adjusted for oil/gas method
CO_2 density, ρ	At initial reservoir conditions	At initial reservoir conditions	Property model; calculated from P and T
Efficiency factor, E	E_{saline}	$E_{oil/gas}$	Property model; calculated from MA_{LS}

For each polygon that has a capacity estimate (saline aquifer portion of buildup or oil and gas pool), the average values for porosity, saturation, CO_2 density, and MA_{LS} were calculated from the property model

for each simulated realization. The 20 simulated realizations described in Section 3.4.4 provide a range of uncertainty for each of the spatial variables. A single thickness value was used for each polygon, calculated from the model above or below the fluid contacts as described in Section 3.4.1. Every cell in the property model was either used in the oil and gas method, or the saline aquifer method, to avoid double counting of potential sequestration volume.

3.5.3.2 Storage Efficiency Factors

The storage efficiency is a major variable in storage capacity and a large driver of the uncertainty in the capacity estimates. Goodman et al. (2011) define the efficiency factors for saline and oil and gas methods as:

$$E_{saline} = E_A \cdot E_h \cdot E_\varphi \cdot E_v \cdot E_d \quad (15)$$

$$E_{oil/gas} = E_v \cdot E_d \quad (16)$$

The saline aquifer efficiency factor accounts for both geological and displacement terms, while the oil and gas efficiency factor assumes greater localization in the geological volume and includes only displacement terms. Table 9 provides descriptions for each of the terms in the efficiency factors (Goodman et al., 2011).

Table 9. Description of the different terms in the efficiency factors (Goodman et al., 2011).

Term	Description
E_A	Fraction of total basin or region area with a suitable formation
E_h	Fraction of total geological unit that meets minimum porosity and permeability requirements for injection
E_φ	Fraction of total porosity that is effective, i.e., interconnected
E_v	Combined fraction of immediate volume surrounding an injection well that can be contacted by CO_2 and fraction of net thickness that is contacted by CO_2 as a consequence of the density difference between CO_2 and in situ water
E_d	Fraction of pore space unavailable due to immobile in situ fluids

The efficiency factors for the saline aquifer method and the oil/gas method were modelled using beta distributions fit on the P10/P50/P90 values for limestone and dolostone from Goodman et. al. (2011). Table 10 shows the input efficiency factor percentiles and the modelled percentiles used in this work. The input values for the efficiency factors are used in many other publications (Goodman et al., 2011, 2016; International Energy Agency Greenhouse Gas R&D Programme [IEAGHG], 2009; Sanguinito et al., 2020).

Table 10. Input efficiency factor distributions and simulated total efficiency factor results; input values are from Goodman et al. (2011).

Factor	Term	Source	Limestone			Dolomite		
			P_{10}	P_{50}	P_{90}	P_{10}	P_{50}	P_{90}
Geological and displacement terms	E_{saline}	Goodman et al., 2011	0.004	0.015	0.041	0.006	0.022	0.055
Saline aquifer efficiency	E_{saline}	Beta distribution	0.004	0.015	0.041	0.006	0.022	0.055
Displacement terms only	$E_{oil/gas}$	Goodman et al., 2011	0.100	0.150	0.210	0.160	0.210	0.260
Oil and gas efficiency	$E_{oil/gas}$	Beta distribution	0.101	0.150	0.211	0.161	0.218	0.261

To quantify the uncertainty in the efficiency factor, the beta distributions for dolomite and limestone were sampled at each decile, from P10 to P90. The nine values for efficiency were then used to get the efficiency for each polygon based on the average fraction of matrix limestone in each of the 20 simulated realizations.

Evaluating the MA_{LS} model in areas known to be fully limestone or dolomite, endpoints of 0.1 and 0.6 were applied; that is, any MA_{LS} value below 0.1 is considered entirely dolomite and any value above 0.6 is fully limestone. Figure 8 shows a cross-section illustrating this. This results in the following equation for the efficiency factor:

$$E_{polygon} = E_{LS} \cdot \frac{MA_{LS} - 0.1}{0.5} + E_{DM} \cdot \left(1 - \frac{MA_{LS} - 0.1}{0.5}\right) \quad (17)$$

where $E_{polygon}$ is the efficiency factor of a polygon with storage potential, E_{LS} is the limestone storage efficiency factor, E_{DM} is the dolomite storage efficiency factor, and MA_{LS} is the average simulated fraction of limestone in the matrix for the polygon.

To quantify the uncertainty in the efficiency factors, each of the 20 simulated realizations of the spatial variables were combined with the nine deciles of the efficiency beta distributions. This resulted in a distribution of 180 sample points from the space of uncertainty. Figure 8 shows the matrix limestone fraction as modelled in Petrel, with inputs from the petrophysical analysis.

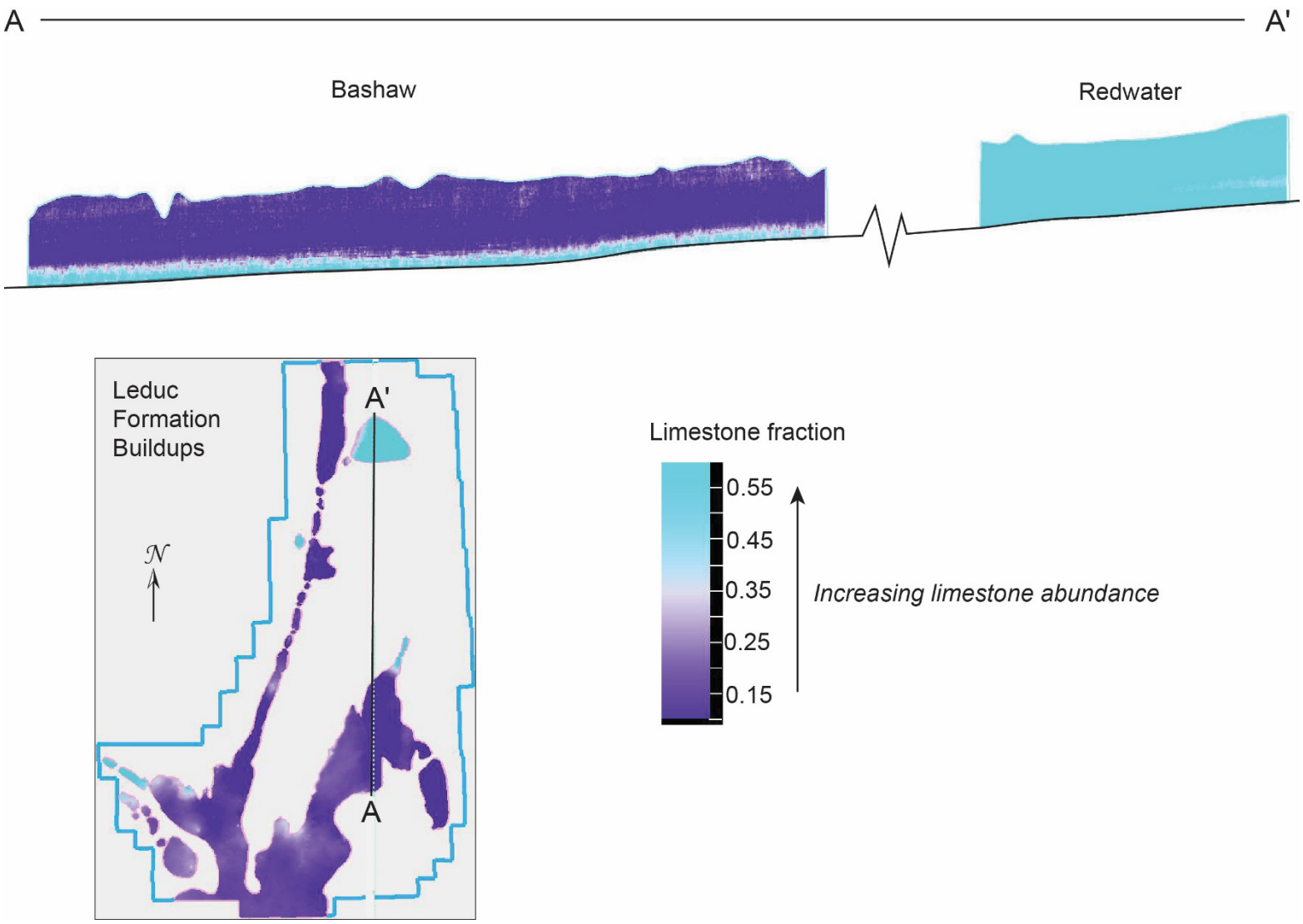


Figure 8. Matrix limestone fraction (0.1 to 0.6, with 0.6 representing pure limestone, 0.1 representing pure dolostone) within the Bashaw and Redwater (Leduc Formation) buildups. Note that the Redwater buildup is mostly limestone along with the base of the Bashaw buildup as shown in the cross-section A-A'. Vertical exaggeration = 25X.

3.5.4 Oil and Gas Methodology Results

Available Leduc Formation oil and gas pool polygons for the study area include instances of overlapping oil and gas pools within the same reservoir (i.e., a gas leg and an oil leg; associated pools; see Figure 2). In these cases, the pool polygons were amalgamated to the largest extent of the overlapping pool boundaries, resulting in a total of 80 evaluated pools (Appendix 3). Of these, 22 have a median (P50) estimate of at least 1 Mt of CO_2 storage capacity and were evaluated by at least one other method for comparison. Figure 9 shows a comparison of the DOE-NETL method, the fluid substitution method, and previous work from Bachu (2004) for comparison.

The widely different assumptions between the methods cause some variability. The purely volumetric DOE-NETL method assumes that the fraction of useable pore space is from the same underlying uncertainty distribution for all pools unless calibrated to actual injection. The fluid substitution method uses only the pore space made available by production.

Considering the 22 pools with the largest estimated capacity, the DOE-NETL method produces a P_{50} estimate of 307.2 Mt of CO_2, with a P_{10} to P_{90} range of 237.2 to 396.6 Mt. The fluid substitution method for these 22 pools produces an estimate of 601.6 Mt. For all 80 evaluated oil and gas pools, the DOE-NETL method P_{50} estimate is 348.9 Mt, with a P_{10} to P_{90} range of 267.2 to 445.5 Mt.

The reported aggregate percentiles (P_{10}, P_{50}, and P_{90}) of capacity estimates are not equal to the sums of the corresponding percentiles over smaller areas, such as individual pools or buildups. This is because the study-area percentiles are calculated from the aggregated uncertainty distribution after pool- or buildup-scale results are combined. Therefore, summing the P_{10}, P_{50}, or P_{90} estimates for all 80 evaluated oil and gas pools listed in Appendix 3 will not reproduce the corresponding aggregate values reported in the text.

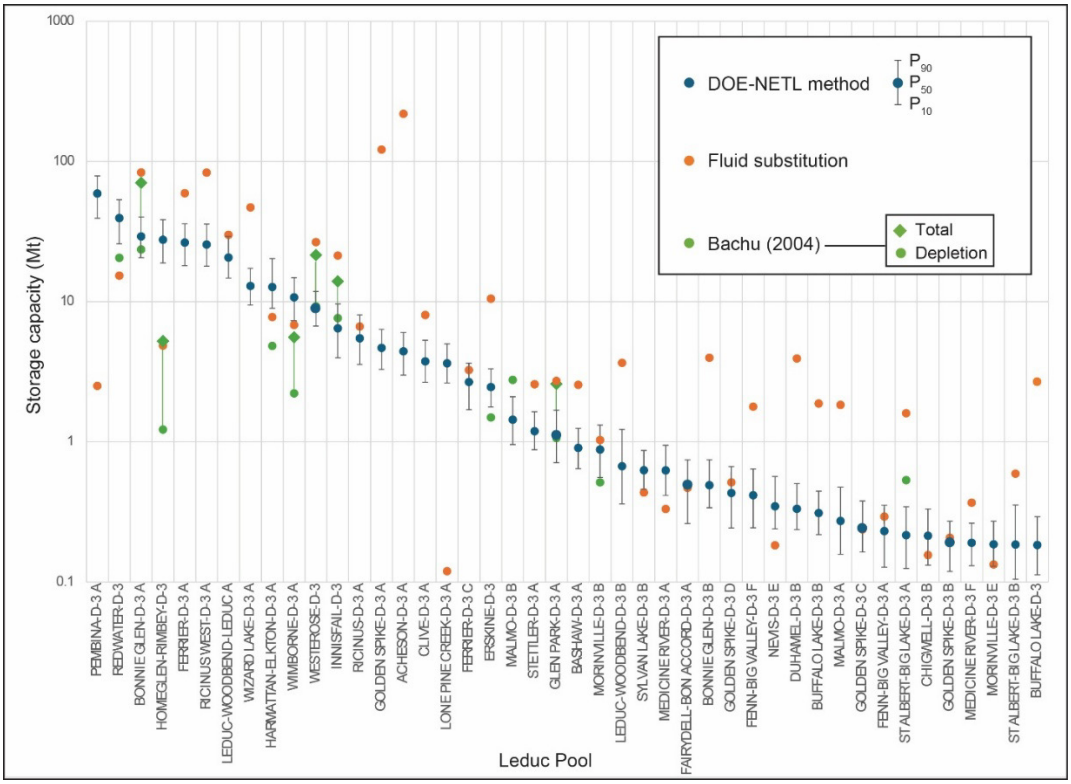


Figure 9. Forty-four Leduc Formation oil and gas pools evaluated by at least two estimation methods (DOE-NETL and fluid substitution). See Figure 2 for location of pools. For the Bachu (2004) estimates, "depletion" represents values without enhanced recovery schemes, whereas "total" represents values after CO_2-EOR has further increased potential sequestration volumes through enhanced recovery.

3.5.5 Saline Aquifer Methodology Results

Twenty-three defined Leduc buildup polygons are within the study area (the Homeglen-Rimbey-Bashaw complex is considered all one contiguous unit; see Figures 10 and 11). The aggregated P_{50} CO_2 storage capacity estimate of the saline aquifer portion of the buildups is 1655.5 Mt with a P_{10} to P_{90} range of uncertainty of 471.9 to 4006.0 Mt.

The Homeglen-Rimbey-Bashaw complex makes up the largest portion of the storage, with a P_{50} estimate of 1218.6 Mt. The Morinville (170.4 Mt), Fenn-Big Valley (81.5 Mt), and Redwater (75.7 Mt) buildups also have P_{50} estimates over 50 Mt of CO_2 storage capacity. There are six buildups with P_{50} estimates of at least 10 Mt (Figure 10).

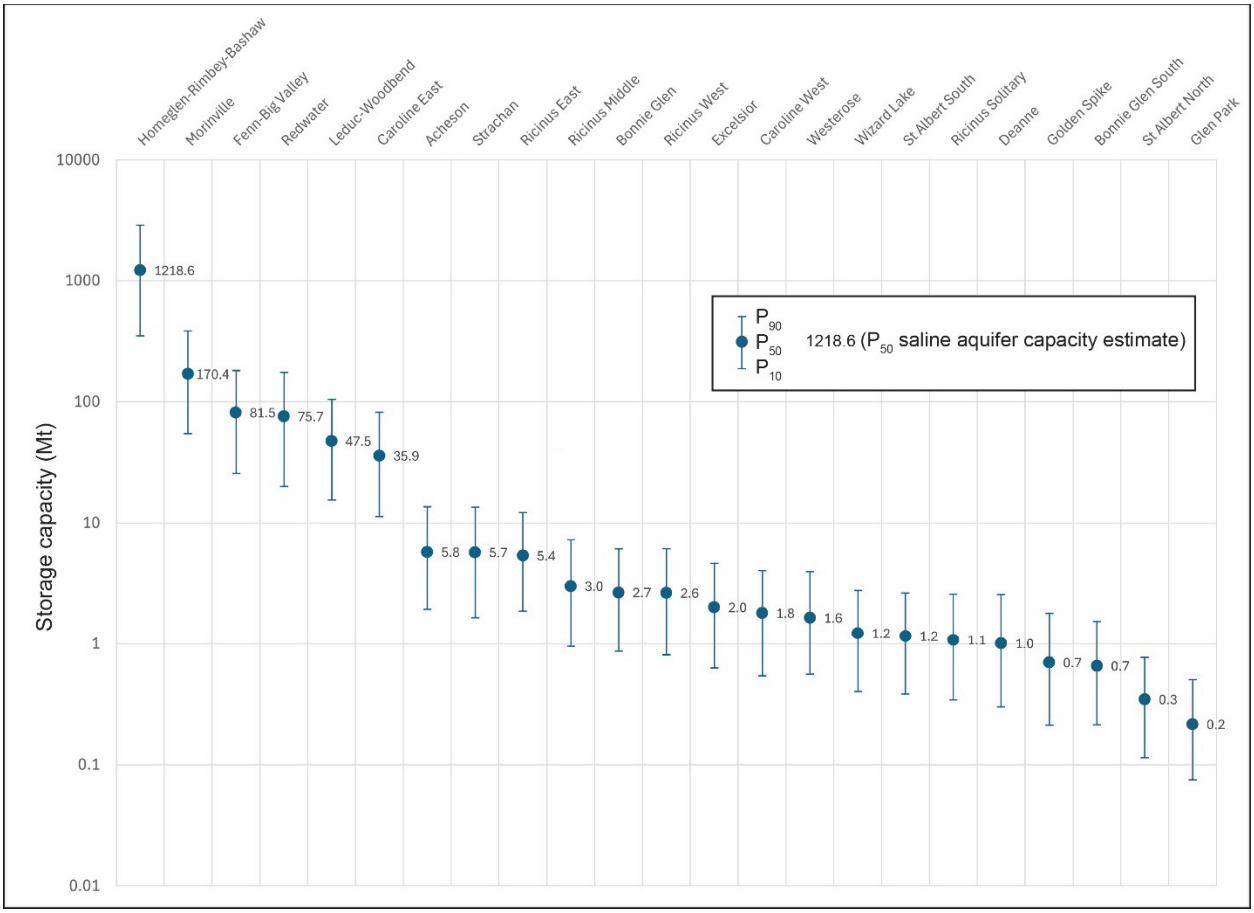
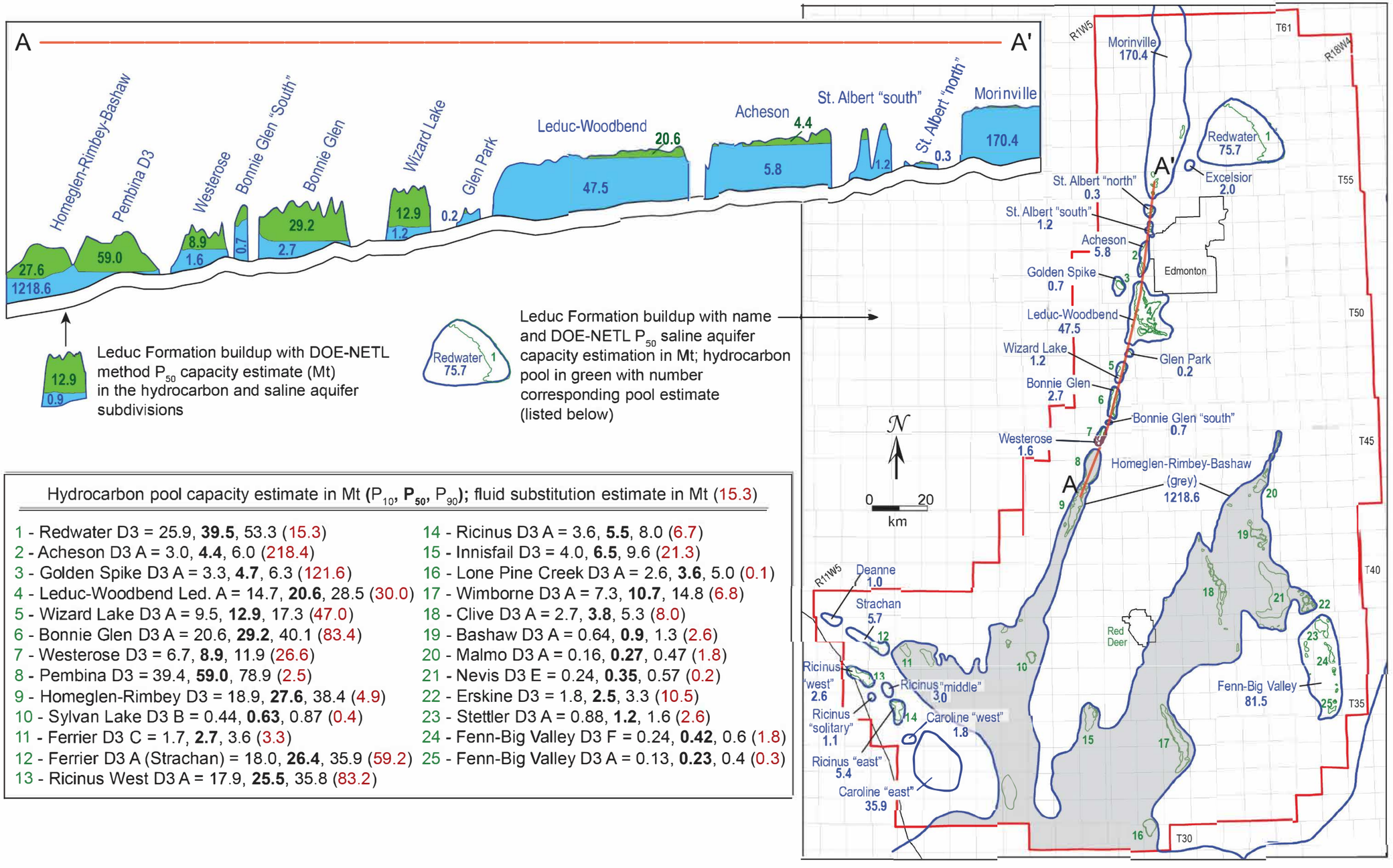


Figure 10. DOE-NETL saline aquifer volumetric estimates for 23 Leduc Formation buildups (excluding hydrocarbon pools) in the study area. See Figure 11 for location of buildups.



Hydrocarbon pool capacity estimate in Mt (P_{10}, **P_{50}**, P_{90}); fluid substitution estimate in Mt (15.3)

1 - Redwater D3 = 25.9, **39.5**, 53.3 (15.3)
2 - Acheson D3 A = 3.0, **4.4**, 6.0 (218.4)
3 - Golden Spike D3 A = 3.3, **4.7**, 6.3 (121.6)
4 - Leduc-Woodbend Led. A = 14.7, **20.6**, 28.5 (30.0)
5 - Wizard Lake D3 A = 9.5, **12.9**, 17.3 (47.0)
6 - Bonnie Glen D3 A = 20.6, **29.2**, 40.1 (83.4)
7 - Westerose D3 = 6.7, **8.9**, 11.9 (26.6)
8 - Pembina D3 = 39.4, **59.0**, 78.9 (2.5)
9 - Homeglen-Rimbey D3 = 18.9, **27.6**, 38.4 (4.9)
10 - Sylvan Lake D3 B = 0.44, **0.63**, 0.87 (0.4)
11 - Ferrier D3 C = 1.7, **2.7**, 3.6 (3.3)
12 - Ferrier D3 A (Strachan) = 18.0, **26.4**, 35.9 (59.2)
13 - Ricinus West D3 A = 17.9, **25.5**, 35.8 (83.2)
14 - Ricinus D3 A = 3.6, **5.5**, 8.0 (6.7)
15 - Innisfail D3 = 4.0, **6.5**, 9.6 (21.3)
16 - Lone Pine Creek D3 A = 2.6, **3.6**, 5.0 (0.1)
17 - Wimborne D3 A = 7.3, **10.7**, 14.8 (6.8)
18 - Clive D3 A = 2.7, **3.8**, 5.3 (8.0)
19 - Bashaw D3 A = 0.64, **0.9**, 1.3 (2.6)
20 - Malmo D3 A = 0.16, **0.27**, 0.47 (1.8)
21 - Nevis D3 E = 0.24, **0.35**, 0.57 (0.2)
22 - Erskine D3 = 1.8, **2.5**, 3.3 (10.5)
23 - Stettler D3 A = 0.88, **1.2**, 1.6 (2.6)
24 - Fenn-Big Valley D3 F = 0.24, **0.42**, 0.6 (1.8)
25 - Fenn-Big Valley D3 A = 0.13, **0.23**, 0.4 (0.3)

Figure 11. Volumetric CO2 capacity estimates from the Leduc Formation in the study area. The saline aquifers and the hydrocarbon pools were subdivided based on the hydrocarbon-water contacts at discovery. The saline aquifer portion of the Homeglen-Rimbey-Bashaw is considered as contiguous and is shaded in grey. Fluid substitution estimate values are listed in red. Listed hydrocarbon pool estimates are using the DOE-NETL method and may be associated or non-associated types.

3.6 Clive Field Benchmarking

The Clive Field east of Red Deer on the Bashaw buildup (previously presented in Figure 2) is currently undergoing enhanced oil recovery, where since 2020 Enhance Energy Inc. has used CO_2 in a miscible flood scheme to enhance the recovery of oil from the Clive D-3A Pool (Leduc Formation). At the time of writing, and assuming that any CO_2 produced with oil will be reinjected and eventually permanently stored, more than 8 Mt of CO_2 has been sequestered at Clive into the Leduc Formation (Enhance Energy Inc., 2026). Results from Enhance Energy Inc.'s operations provide a unique opportunity to compare the parameters used in this study, and the modelling results, with actual field data.

Enhance Energy Inc. and North West Redwater Partnership (2011) reported an OOIP of the Leduc and Nisku reservoirs (Nisku sits above the Leduc) at Clive of 166 million barrels (26.4 $10^6 m^3$). In the 2011 report they also provided CO_2 densities based on the original reservoir pressures for the Leduc and Nisku reservoirs aggregated together. Since injection commenced in 2020, submission of an annual progress report to the AER has been required and these reports contain updated information in addition to new information based on performance at the scheme. Whereas the 2011 report had Nisku-Leduc aggregated values, the annual progress reports are reservoir-interval specific, but as these reports meet different objectives from the 2011 report, they do not contain some of the CO_2 calculations. Comparison of the modelled CO_2 results from this study using the fluid substitution method with those at Clive Field has therefore relied on a combination of data from Enhance Energy Inc. (2011) and the most recent annual report submitted in 2025.

In the 2011 report, the operator published volumetric oil capacity (i.e., OOIP) in the Leduc at 97 million barrels of oil, and reservoir simulation by the operator suggested a recovery factor of 60%. This would equate to approximately 58 million barrels of oil (or 9.54 $10^6 m^3$) which could potentially be replaced by CO_2. In the same report, the measured aggregated reservoir temperature and pressure by the operator was reported as 69ºC and 12 500 kPa, respectively. At these conditions, the operator calculated the density of CO_2 at 382 kg/m^3 in a supercritical state. In addition, the operator presents the original discovery pressure at 16 595 kPa, with a corresponding density of the CO_2 at 579 kg/m^3, an increase of 51.6%.

Based on numbers derived from the operator of the Clive Field, the potential replacement of oil produced from Clive with CO_2 is 9.54 $10^6 m^3$ × (1.45) × (382 kg/m^3) × (tonne/1000kg) = 5 284 000 tonnes CO_2 (5.3 Mt), where one m^3 of oil occupies a subsurface volume 1.45 m^3 (due to liberation of solution gas during production before miscible flooding starts).

Under the 2011 reported original reservoir conditions, the volume of potential CO_2 stored increases from 5.3 Mt to 8.0 Mt. An additional 1.21 Mt of storage capacity was calculated by Enhance Energy Inc. (2011) due to produced gas from the Leduc Formation. The total storage capacity was therefore determined to be 6.51 Mt for produced oil and gas or 9.9 Mt using original reservoir pressure.

The AER has access to the results of all PVT characterization of reservoir fluids conducted in the hydrocarbon accumulation discoveries made in the province of Alberta. A detailed analysis of these datasets is normally only conducted in cases where secondary or tertiary recovery techniques are implemented, with the consequent need for the use of the characterization of the fluids under pressure and temperature to assess its performance. Of the Leduc reservoirs in the area of interest, four were found to have had secondary or tertiary recovery techniques implemented that had usable PVT tables.

Comparative plots of the respective oil formation volume factor (Bo), gas formation volume factor (Bg) and the solution gas-oil ratio (Rs) against pressure provided a visual representation of the average curve. This was then used to set up a PVT table to be used as an average representation of the fluid characterization of all the Leduc reservoir fluids.

Under the conditions outlined in the 2011 report, a PVT-characterization-derived CO_2 density of 768 kg/m^3 was used in the substitution method. This is a variance from the operator-derived density. The method used by the operator to calculate CO_2 density was not provided.

Applying the fluid substitution technique results in a CO_2 replacement volume of 8.04 Mt. The 8.04 Mt is less than the 9.9 Mt of CO_2 replacement volume calculated by Enhance Energy Inc. (2011), at original reservoir pressure, but provides a degree of validity on the values derived through the fluid substitution methodology.

The Leduc Formation reservoir pressure submitted in the annual progress report (Enhance Energy Inc., 2025) is 13 655 kPa and discovery pressure of the Clive D-3A in the Leduc is reported as 17 593 kPa. Introducing the new 2025 values of pressures provided a new PVT-derived CO_2 density value of 783 kg/m^3 but had little impact on the calculated replacement volume of 8.05 Mt (Table 11). In the 3D geocellular model, which was used for estimating capacity with the DOE-NETL method, the simulated CO_2 density at Clive has a mean of 570 kg/m3 (range of 470–690 kg/m^3) which represents discovery conditions. This modelling result is not comparable to the 768 kg/m^3 from PVT characterization at discovery conditions (used for the fluid substitution method) but is comparable to the 579 kg/m^3 at discovery conditions determined using parameters in the 2011 report from Enhance Energy Inc. Although the simulated CO_2 density at Clive is comparable to that calculated with parameters in Enhance Energy Inc. (2011), the CO_2 capacity estimates determined with the DOE-NETL method (P_{50} of 3.8 Mt; Table 11) are not comparable to Enhance Energy Inc. (2011). Furthermore, the current amount of sequestered CO_2 significantly exceeds the P90 estimate of 5.3 Mt using the DOE-NETL method. Factors that likely account for the poor results from the DOE-NETL method at Clive include (1) the efficiency factor, (2) the resolution of the regional evaluation approach, and (3) the distribution of modelled porosity in that the distribution of porosity around the mean (recall Table 2) may be too narrow. At a broader level, these factors may suggest that the DOE-NETL results in this study have under-represented the CO_2 storage capacity of the Leduc buildups.

Table 11. Comparison of the Clive D-3A Pool reservoir parameters for the fluid substitution method and volumetric results.

Report	Reservoir P Type (kPa)	Reservoir P (kPa)	Reservoir T (^{0}C)	OOIP (10^3)	Production to Date (10^3)	RF	Bo	CO_2 Density (kg/m^3)	Fluid Substitution CO_2 Volume (Mt)	DOE-NETL Method (Mt)
2011 Enhance Energy Inc.	Current	12 500	69	12 355.2	8201.3	66%	1.45	382	6.51	
2011 Enhance energy Inc.	Initial pressure	16 595						579	9.9	
This study	Pressure differential (for FS method)	4095						768.02	8.04	
2025 Enhance Energy Inc.	Current	13 655								
2025 Enhance Energy Inc.	Initial pressure	17 593								
This study with 2025 data	Pressure differential (for FS method)	3938						782.59	8.05	
This study	Initial Pressure							570		P10 = 2.7 P50 = 3.8 P90 = 5.3

Abbreviations: P, pressure; T, temperature; aggr., aggregated; RF, recovery factor; Bo, formation volume factor; FS, fluid substitution

4 Ireton Formation Caprock Integrity Assessment

Lithofacies and X-ray fluorescence (XRF) analysis, and mercury injection capillary pressure (MICP) tests were conducted on samples from 12 Ireton Formation cores to provide information on sealing capacity across the study area (Table 12; Appendix 4). Being a shale, the Ireton is typically not cored, and most of the cores represent small portions of the overall thickness of the formation. Cores are usually found at the base of the formation, as they represent the interval where coring began with intentions of retrieving cores from the underlying hydrocarbon-producing Leduc Formation. Where possible, fully cored intervals through the Ireton were selected and these tend to be where the Ireton is thinnest, corresponding to the Bashaw complex (previously presented in Figure 4).

Table 12. Ireton Formation cores logged for the study, and their location with respect to the underlying Leduc Formation buildups.

Unique Well Identifier (UWI)	Ireton Formation Core Depths (m; MD)	Underlying Leduc Formation Buildup Name (Field)
102/08-27-051-27W4/00	1628.7 to 1632.5	Golden Spike
100/12-29-050-26W4/00	1608.25 to 1615	Leduc-Woodbend
100/13-02-053-26W4/00	1505.4 to 1516	Acheson
100/16-26-039-24W4/00	1846.8 to 1855.3 (entire Ireton)	Bashaw (Clive)
100/06-22-038-24W4/00	1877.5 to 1883.8 (entire Ireton)	Bashaw (Clive)
100/06-18-040-21W4/00	1642.6 to 1668 (entire Ireton)	Bashaw
100/14-16-038-20W4/00	1598.4 to 1615.3	Fenn-Big Valley (Stettler)
100/15-29-034-01W5/00	2622.9 to 2633.8	Bashaw (Innisfail)
100/09-23-033-26W4/00	2246.9 to 2253.2	Bashaw (Wimborne)
100/15-24-039-21W4/00	1630.9 to 1643	Erskine
100/16-36-041-23W4/00	1720.5 to 1726.4	Bashaw
100/07-32-037-09W5/00	4060.4 to 4076.1	Strachan (Ferrier)

Abbreviations: MD, measured depth

4.1 Lithofacies

Seven lithofacies were identified in the Ireton Formation (Table 13). Lithofacies range from shale (pure terrigenous clastics) to floatstones with variable argillaceous content (allochthonous carbonate). Facies are often found as interbedded combinations of terrigenous clastics and carbonate (marls), or as admixed varieties through intense bioturbation. Dark-coloured mudstones typical of toe-of-slope settings (Stoakes, 1980) were not observed in the studied cores, as all the cores were from intervals overlying the Leduc buildups, deposited in shallower water settings than Duvernay-type deposits. Dolomitic limestone and dolomite were observed rarely within the cores but occur more commonly within carbonate-rich Ireton facies where the formation is thin over the Bashaw complex. Rare occurrences of *Thamnopora* floatstone were observed—the only carbonate facies interpreted to be close to in situ.

Table 13. Ireton Formation lithofacies and associated MICP sample numbers from cores overlying Leduc Formation buildups.

	Lithofacies Number						
	LF1	**LF2**	**LF3**	**LF4**	**LF5**	**LF6**	**LF7**
Lithology	Shale (rare)	Calcareous shale	Calcareous shale interbedded with argillaceous lime mudstone	Argillaceous lime or dolomudstone	Argillaceous lime- or dolomudstone interbedded with grainy (recrystallized?) limestone	Crinoid floatstone; bioclastic argillaceous wackestone to mudstone matrix	*Thamnopora* floatstone; grey-black argillaceous lime- or dolomudstone
Sedimentary structures	None observed; mostly rubble	Planar laminations; lesser wavy laminations; rare argillaceous lime mudstone beds	Wavy bedded to nodular argillaceous carbonates (subtle nodular banding); planar laminations in calcareous shale unless disturbed by carbonate lithification	Mottled to wavy bedded to stylonodular to massive; some nodular and burrow nodular textures; wavy bedding or nodular textures enhanced by presence of argillaceous-rich beds	Wavy limestone beds; lenses of limestone	Nodular to nodular banded; common anastomosing shaly partings; bioclastic debris associated with mudstones	Similar to LF3; nodular banding accentuated by argillaceous laminae
Fossils	-	Rare brachiopods	Crinoids	Rare brachiopods; rare crinoids	Rare brachiopods (some articulated)	Abundant crinoids; disarticulated brachiopods	*Thamnopora*; skeletal debris
Lithic accessories	-	-	Rare phosphatic rip-up clasts	Common phosphatic rip-up clasts	-	Common phosphatic rip-up clasts	-
Bioturbation index	0	0-2	0–3	0–5	0	0-2	0-1
Diagenetic features	-	Common pyrite cubes	Common pyrite and anhydrite nodules (commonly associated)	Rare to common stylolites; anhydrite nodules	Common calcite nodules; common calcite replacement by anhydrite; common pyrite	Common anhydrite and calcite nodules	Dolomitization of bioclasts
MICP sample numbers	13-2-1	16-18-3 07-32-1 12-29-1 14-16-1 15-29-1	16-18-2 09-23-1 8-27-1 15-24-1 13-2-2	16-18-1 06-22-1 09-23-2 16-36-1 16-26-1 16-26-3	16-36-2	15-24-2	16-26-2

4.2 MICP Analysis

When CO_2 is injected into a reservoir the pore space is generally filled with water. As CO_2 is lighter than the formation water, CO_2 would migrate upwards through the reservoir via buoyancy. Buoyancy pressure drives the movement of CO_2 (non-wetting phase) in the subsurface and forces it into the pore throats of a rock, subsequently displacing water (wetting phase). The upward movement of the CO_2 through the pore system is resisted by capillary pressure. If the buoyancy surpasses the capillary pressure, the CO_2 will keep moving upwards until it is stopped by the low-permeability caprock. When a trap is filled to its seal capacity, the upward buoyancy of CO_2 is balanced by the capillary pressure of the caprock. The buoyancy is determined by the density contrast (g/cc) between CO_2 and water, multiplied by the column height (ft) and the gravitational constant (0.433 psi/ft):

$$\boldsymbol{P_b = (\rho_{b2} - \rho_{CO2})gH = P_C} \tag{18}$$

where P_b is buoyancy pressure in pounds per square inch (psi), P_c is capillary pressure in psi, ρ_{b2} is the density of brine (g/cm^3), ρ_{CO2} is the density of CO_2 (g/cm^3), H is the height of the CO_2 column above the free water level in feet, and g is the gravitational constant (0.433 psi/ft).

Since the capillary pressure data are measured in the lab using mercury injection, to evaluate the seal capacity for CO_2 the data must be converted from the mercury-air system to the CO_2-brine system using the equation below:

$$\boldsymbol{Pc_{CO2-Brine} = -Pc_{Hg-Air}\frac{\sigma_{CO2-Brine}\cos\theta_{CO2-Brine}}{\sigma_{Hg-Air}\cos\theta_{Hg-Air}}} \tag{19}$$

where $Pc_{CO2-Brine}$ is the capillary pressure in the water-CO_2 system, Pc_{Hg-Air} is the capillary pressure in the air-mercury system, $\sigma_{CO2-Brine}$ and σ_{Hg-Air} are the interfacial tensions of the water-CO_2 and the air-mercury systems, respectively, and $\theta_{CO2-Brine}$ and θ_{Hg-Air} are the contact angles of the water-CO_2-substrate and air-mercury-substrate systems, respectively (see Table 14).

Two capillary pressures are derived from MICP analysis after correcting for closure pressure (conformance): entry and threshold pressures. Entry pressure refers to the pressure at which the non-wetting phase begins to penetrate the pore system. This is indicated by the first point of non-zero, non-wetting saturation on the capillary pressure curve. Threshold pressure is the pressure level at which a continuous filament of non-wetting phase extends through the pore network, enabling the non-wetting phase to traverse through the seal. The threshold pressure is considered the most representative point of seal failure and has been widely used for estimating caprock seal capacity (Kivior et al., 2002; Dewhurst et al., 2002; Daniel and Kaldi, 2008; Gray, 2017). As capillary pressure is an indicator of pore throat size, entry pressure corresponds to the largest pore throat, while threshold pressure is associated with a pore throat close to the mean or mode pore throat size. For homogeneous samples with well-sorted pore throats, entry pressure and threshold pressure are likely to be very close. The difference between entry and threshold pressures arises from the heterogeneity of the rock.

The height (H) of the CO_2 column corresponding to a specific capillary pressure (P_c) is calculated as:

$$\boldsymbol{H = \frac{P_C}{(\rho_b - \rho_{CO2})g}} \tag{20}$$

where ρ_b is the density of brine (g/cm^3), ρ_{CO2} is the density of CO_2 (g/cm^3), and g is the gravitational constant (0.433 psi/ft).

The pressure data have been converted to the CO_2-brine system using Equation 2 and the parameters in Table 14. For evaluation of these properties in the Ireton Formation, 20 samples were selected for MICP analysis. Samples (~2 cm thick pieces cut from core plugs/~15 grams) were analyzed at AGAT Laboratories with a Micromeritics Autopore IV instrument. The capillary pressure data of all samples are summarized in Figure 12 and Table 15. Figure 12a presents the original mercury injection data, characterizing the process of mercury penetrating the pore system and displacing air as pressure increases. Conformance correction was performed by the vendor. Figure 12b represents the process of CO_2 intruding into the pore space and displacing brine. The samples are colour-coded by lithofacies, and there is an apparent overlap in capillary pressure data across different lithofacies. As shown in Table 15, most entry pressures range from 114 to 225 psi, with three more porous samples exhibiting lower entry pressures ranging from 16.3 to 53.3 psi. Similarity in entry pressures is noted from five of the MICP tests despite variable lithofacies (Table 15). Identical entry pressures may arise from the step-rate pressure increase during mercury intrusion and/or the similarity in the largest pore throats from various Ireton lithofacies.

Table 14. Interfacial tension and contact angle values (from Kawaura et al., 2013) used in this study.

	Hg/Air	Supercritical CO_2/Brine
Interfacial tension (mN/m)	480	27
Contact angle (°)	140	34

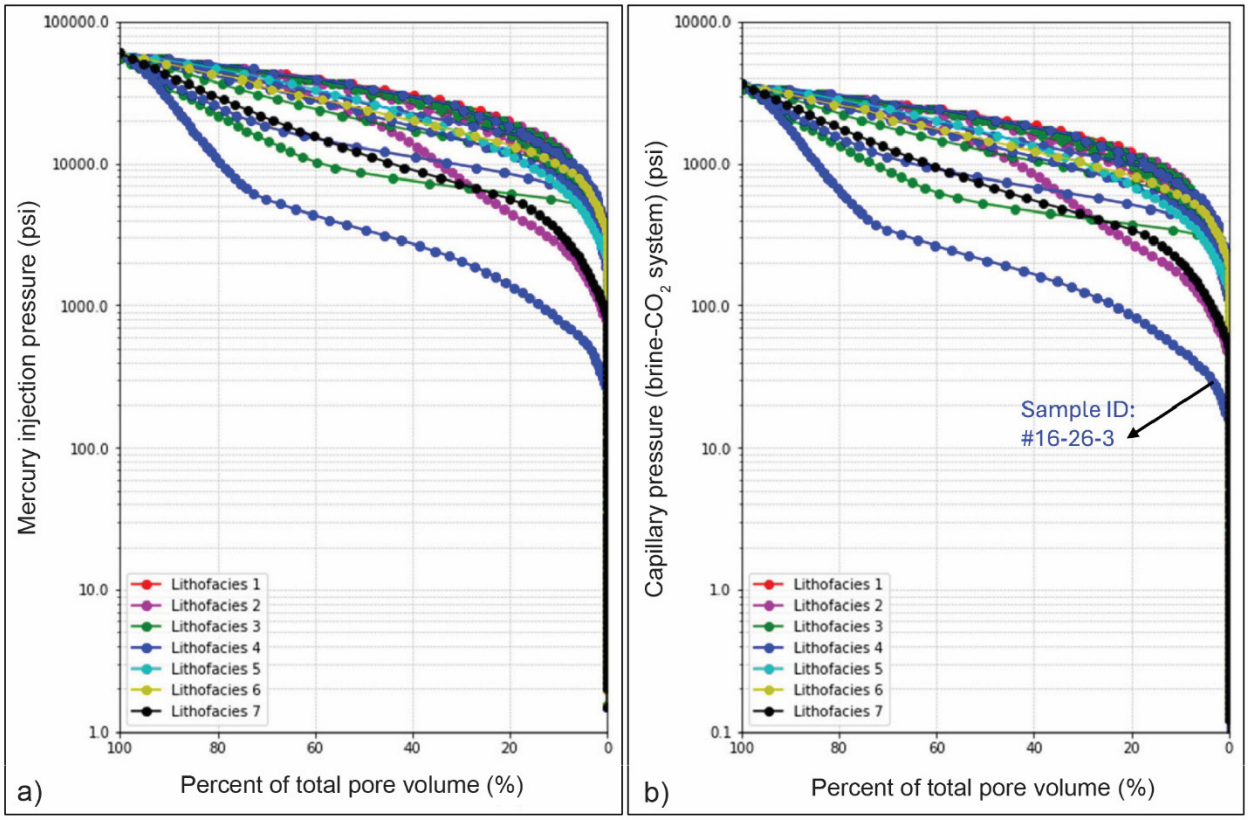


Figure 12. Capillary pressure data of 20 MICP samples from the Ireton Formation: a) mercury-air system, and b) CO_2-brine system.

Table 15. Capillary pressure data and calculated CO_2 column height from the 20 MICP samples taken from the Ireton Formation.

UWI	Sample #	Lithofacies	Depth (m)	Porosity (%)	Permeability (mD)	Entry Pressure	CO_2-Brine Calculated Threshold Pressure	CO_2 Column Height (from entry P in m)	CO_2 Column Height (from threshold P in m)
100061804021W400	6-18-1	LF4	1665.8	1.08	$2.04e^{-5}$	224.6	480.4	385.6	824.7
100061804021W400	6-18-2	LF3	1659.5	1.46	$6.93e^{-5}$	174.4	797.7	299.4	1369.5
100061804021W400	6-18-3	LF2	1650.1	2.21	$2.09e^{-4}$	114.4	1118.7	196.4	1920.6
100062203824W400	6-22-1	LF4	1881.2	1.56	$7.66e^{-5}$	206.3	944.6	354.2	1621.8
100073203709W500	7-32-1	LF2	4060.6	0.90	$5.02e^{-5}$	174.4	733.1	299.4	1258.7
100092303326W400	9-23-1	LF3	2251.4	1.19	$9.86e^{-5}$	174.4	673.6	299.4	1156.5
100092303326W400	9-23-2	LF4	2249.4	2.11	$1.22e^{-4}$	114.2	372.7	196.1	639.9
100122905026W400	12-29-1	LF2	1614.7	1.84	$8.81e^{-5}$	160.2	733.1	275.0	1258.6
100130205326W400	13-2-1	LF1	1515.8	2.39	$1.29e^{-4}$	174.3	673.6	299.3	1156.5
100130205326W400	13-2-2	LF3	1511.6	3.19	$3.48e^{-5}$	160.0	441.4	274.7	757.8
100141603820W400	14-16-1	LF2	1615.0	2.93	$1.11e^{-4}$	135.2	944.6	232.1	1621.8
100152403921W400	15-24-1	LF3	1641.2	3.74	$1.17e^{-4}$	135.2	342.5	274.9	588.0
100152403921W400	15-24-2	LF6	1635.4	1.64	$2.64e^{-5}$	206.4	441.4	354.4	757.8
100152903401W500	15-29-1	LF2	2633.2	1.12	$3.11e^{-4}$	49.0	160.1	84.2	274.9
100162603924W400	16-26-1	LF4	1854.0	3.90	$8.39e^{-5}$	160.1	342.5	274.9	588.0
100162603924W400	16-26-2	LF7	1853.2	3.47	$1.21e^{-3}$	53.3	206.3	91.35	354.3
100162603924W400	16-26-3	LF4	1850.1	3.37	$1.34e^{-2}$	16.3	32.1	27.9	55.0
100163604123W400	16-36-1	LF4	1726.2	1.76	$1.60e^{-4}$	147.1	733.0	252.6	1258.5
100163604123W400	16-36-2	LF5	1723.5	1.03	$5.59e^{-5}$	135.4	569.0	232.4	976.9
102082705127W400	8-27-1	LF3	1632.2	2.66	$1.40e^{-4}$	174.4	568.8	299.4	976.6

Most Ireton samples can retain a CO_2 column height ranging from 196.4 to 385.6 m (based on entry pressures) before any CO_2 intrusion occurs. However, three potentially more porous samples can only retain a shorter CO_2 column height ranging from 27.9 to 91.5 m (see Table 15 above). CO_2 column heights measured from threshold pressures are much higher, with most in the range of 345.3 to 1920.6 m, but with two low heights measured at 55 and 274.9 m; however, 274.9 m is greater than the thickness of most of the Leduc buildup thicknesses in the study area.

4.3 Petrography

Fourteen thin sections taken from the Ireton Formation, representing all identified facies, were reviewed to assess porosity and characterize mineralogy. Due to the fine-grained nature of some of the collected samples, two of them failed during the thin section fabrication process (i.e., thin sections from corresponding MICP analyses 6-18-3 and 13-2-2). Images and observations were taken with a Zeiss AxioImager microscope and AxioCam 705 Colour camera under transmitted and reflected light settings. In addition to blue-dyed epoxy saturation for porosity determination, the thin sections were stained with Alizarin Red S dye for calcite versus dolomite determination. However, no thin sections seemed to have taken on the Alizarin Red S dye, even though two attempts were made, at two separate labs. As such, despite much of the core-based work suggesting a strong calcitic component within the various Ireton facies, very few thin sections reveal any staining, except for coarse crystalline calcite spar within larger pores.

Except for lithofacies (LF)1 (shale), all thin sections are a mixture of fine-grained terrigenous clastics and carbonates, with lesser pyrite and anhydrite (Figures 13–15). Where carbonates are present, either in distinct laminae (e.g., Figure 15a) or as part of the general matrix (Figures 13b, e, and 14a), calcite usually forms very-finely crystalline anhedral to subhedral textures. A general observation is an increasing crystal size from LF2 and 3 to LF4 through LF7. Bioclasts are generally rare except in thin sections taken from LF6 and 7 (Figure 15c, e), which had bioclasts observed in core.

Dolomite is abundant in thin sections from LF2–LF7 but is commonly localized along the edges of pores (or former pores) as coarsely crystalline rhombohedral varieties (Figures 13c, d, 14b, c, and 15d, e, and f). These former pores are commonly occluded by coarse, blocky calcite spar (Figures 13c, d, 14b, and 15e, f), and less commonly by anhydrite (Figures 14f and 15f) and pyrite (Figure 13d). LF5 shows abundant diagenetic alteration in carbonate-rich laminae through the presence of coarsely crystalline anhydrite (Figure 14b).

Abundant dolomite is found in thin sections taken from above the Bashaw complex in wells 100/06-22-038-24W4/00 and 100/16-26-039-24W4/00 (previously presented in Figure 4). Here, dolomite is abundant as a matrix phase and can be associated with intercrystalline porosity (Figure 14e). However, intercrystalline porosity is rarely observed at thin-section scale, and is associated with more coarsely crystalline lithofacies commonly affected by dolomitization (Figures 14e and 15c).

The most common porosity type observed in the thin sections is an *intra*crystalline variety associated with dolomite rhombs near former pores (Figure 13c, d) or in dolomite clusters that do not display evidence of former pores (Figures 13f and 14d). This type of porosity appears to follow distinct zonation within the dolomite rhombs (e.g., Figure 14d).

Overall, as expected, porosity is very low in most of the thin sections, especially within areas rich in terrigenous clastics. Porosity increases in more coarsely crystalline carbonate-rich areas. Large pores are observed (e.g., Figure 14c), but they are commonly occluded by calcite, anhydrite, and pyrite. Unstained "pores" were observed, but many of these lacked any pore-lining phases and were associated with the terrigenous component. As such, they are considered to be a result of "plucking" during thin-section preparation.

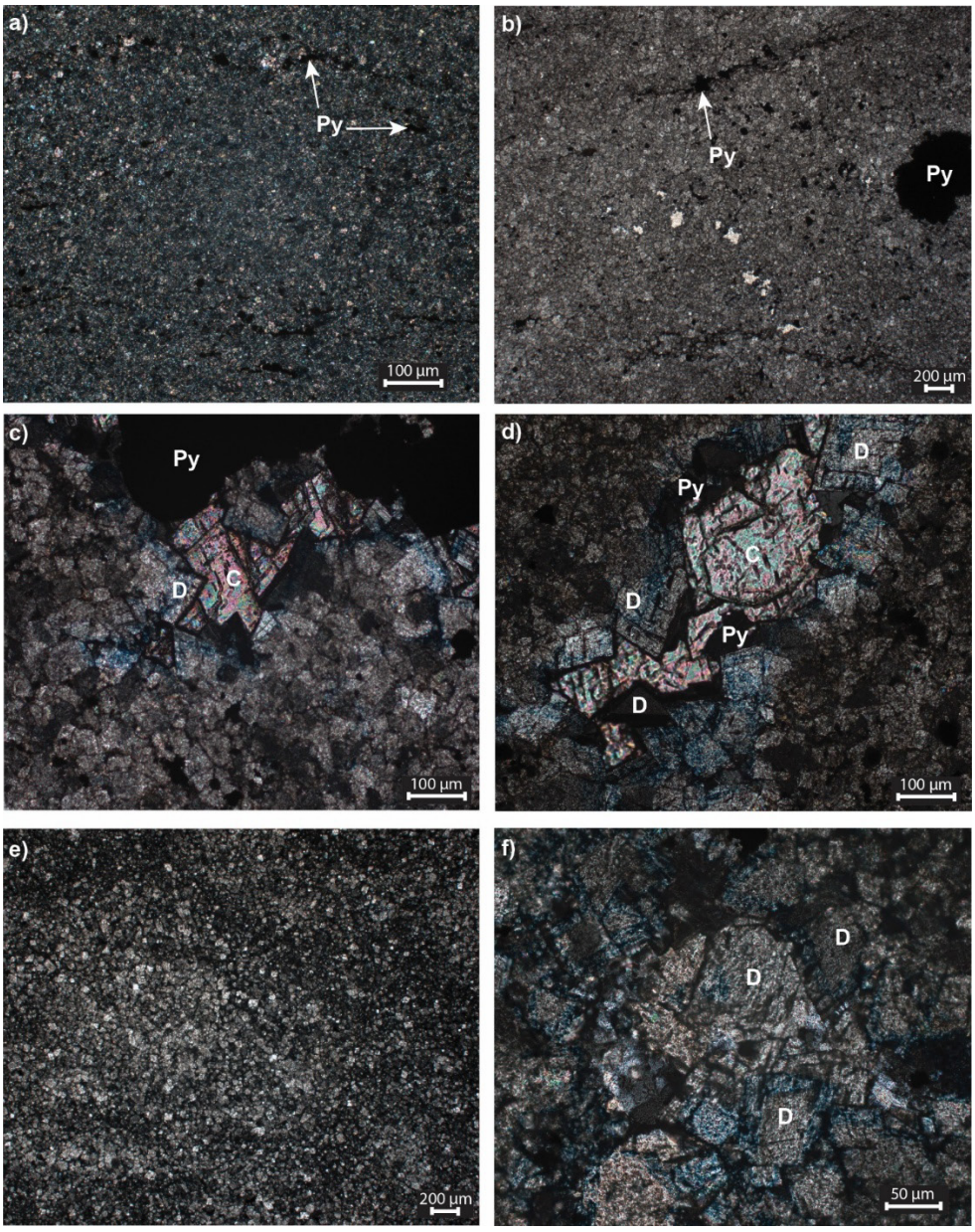


Figure 13. Photomicrographs of Ireton Formation lithofacies LF1 to LF3. a) LF1: Very fine-grained terrigenous clastics with abundant finely disseminated pyrite (Py) throughout. One possible conical, pyrite-coated tentaculitid was noted from this section. Well 100/13-02-053-26W4/00, 1515.8 m, 10X, crossed polars. b) LF2: Similar to a) but with more coarsely crystalline subhedral to anhedral calcite and abundant euhedral dolomite present. Abundant pyrite (Py) throughout with large masses present. Well 100/15-29-034-01W5/00, 2633.15 m, 2.5X, plane polarized. c) LF2: Birefringent blocky calcite spar (C) and pyrite (Py) occluding a former pore with coarse dolomite rhombs (D) on edge of pore. Dolomite rhombs show intracrystalline porosity (blue). Well 100/15-29-034-01W5/00, 2633.15 m, 10X, crossed polars. d) LF2: Same as c) with well developed intracrystalline porosity within dolomite rhombs, possibly following crystal zonation. Well 100/15-29-034-01W5/00, 2633.15 m, 10X, crossed polars. e) LF3: Very finely crystalline anhedral to euhedral carbonates mixed with fine terrigenous clastics. Well 100/15-24-039-21W4/00, 1641.15 m, 2.5X, crossed polars. f) LF3: Anhedral to euhedral dolomite (D) with intracrystalline porosity, possibly following crystal zonation in the rhombs. Well 100/15-24-039-21W4/00, 1641.15 m, 20X, crossed polars.

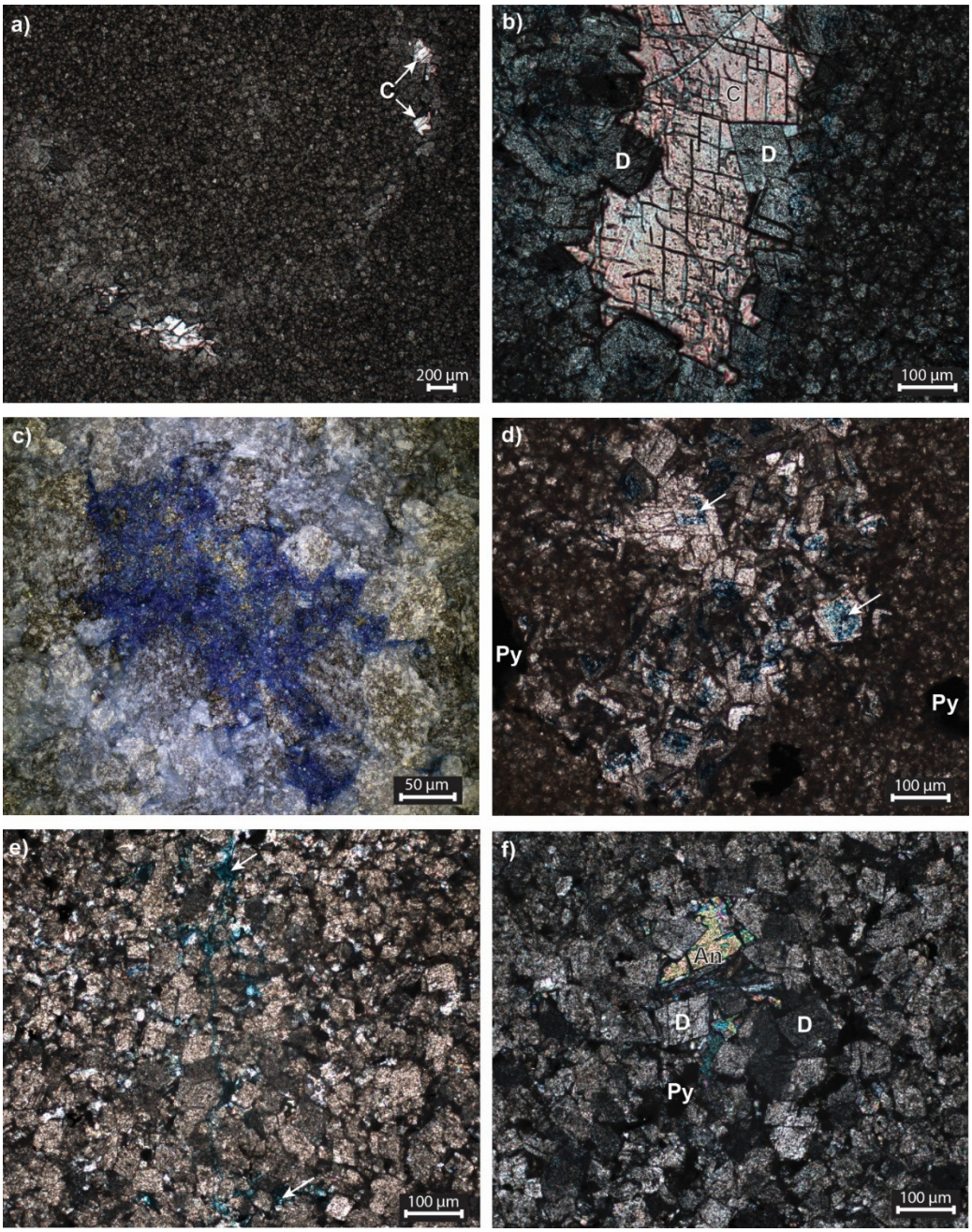


Figure 14. Photomicrographs of Ireton Formation lithofacies LF4. a) Finely crystalline, anhedral to subhedral carbonates mixed with fine terrigenous clastics with larger pores (up to 250 µm) occluded by blocky calcite spar (C). Well 100/06-22-038-24W4/00, 1881.2 m, 2.5X, plane polarized. b) Rhombohedral dolomite (D) lining a large pore occluded by blocky calcite spar (C). Well 100/06-22-038-24W4/00, 1881.2 m, 10X, crossed polars. c) Large (>250 µm) irregular pore lined with rhombohedral dolomite. Well 100/06-18-040-21W4/00, 1665.8 m, 20X, reflected light with barrier filter. d) Very finely crystalline matrix with pyrite (Py), and more coarsely crystalline rhombic dolomite displaying intracrystalline porosity (blue) that appears to be within interior zones of the rhombs (white arrows). Well 100/06-22-038-24W4/00, 1881.2 m, 10X, crossed polars. e) Subhedral to anhedral calcite (smaller crystals) to euhedral dolomite (rhombic) displaying intercrystalline porosity (blue). Well 100/16-26-039-24W4/00, 1850.05 m, 10X, crossed polars. f) Rhombic dolomite (D) with fine pyrite (Py) near a small pore occluded by brightly birefringent anhydrite (An). Well 100/16-26-039-24W4/00, 1850.05 m, 10X, crossed polars.

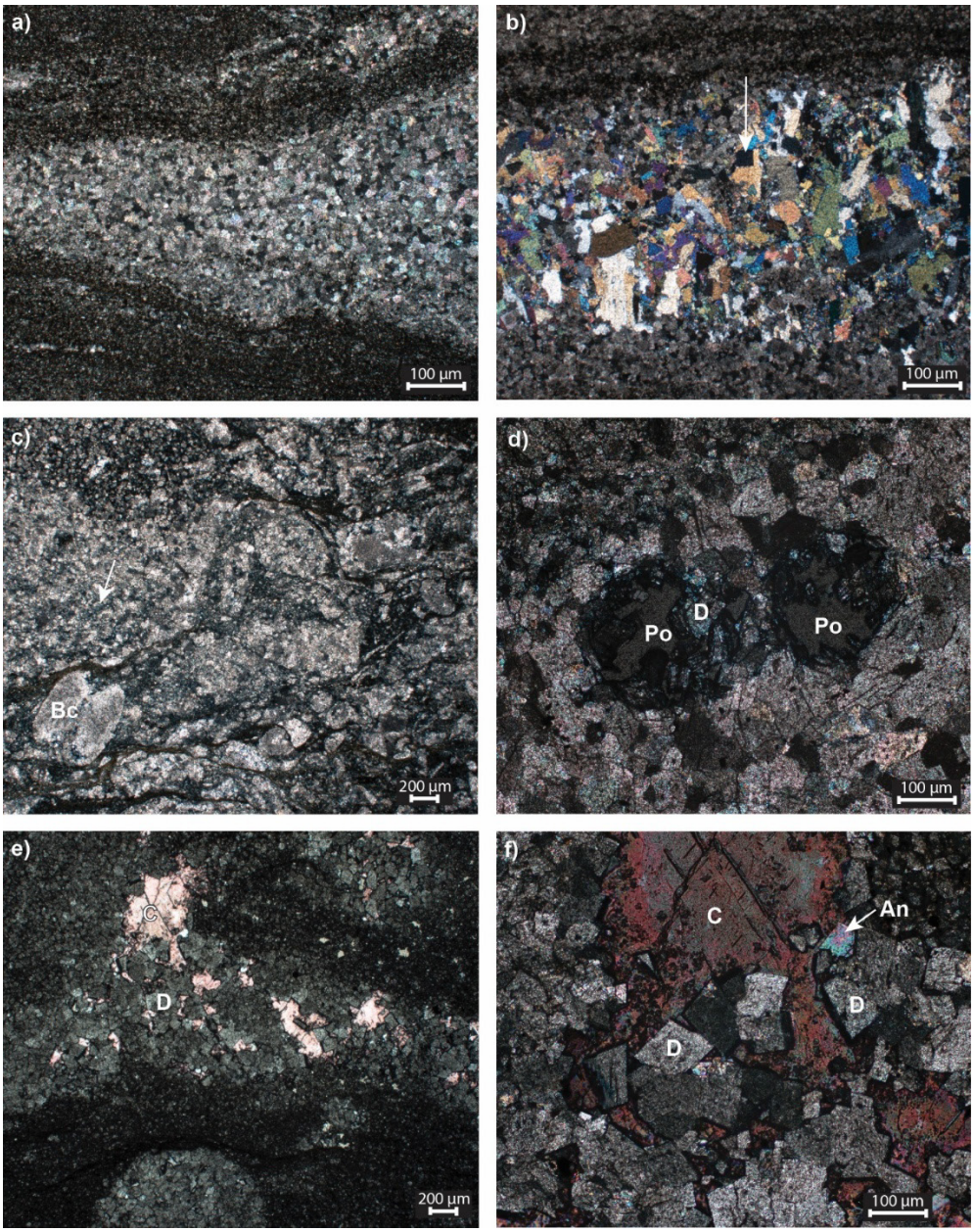


Figure 15. Photomicrographs of Ireton Formation lithofacies LF5 to LF7. a) LF5: Fine-grained terrigenous clastics draping around a calcite-rich lamination. Very little porosity is observed. Well 100/16-36-041-23W4/00, 1723.5 m, 10X, cross polars. b) LF5: Coarsely recrystallized anhydrite, some with pseudo-cubic habit (white arrow), within laminae as in a). Crystals can be >100 µm in length. Well 100/16-36-041-23W4/00, 1723.5 m, 10X, cross polars. c) LF6: Abundant bioclastic debris (Bc), including small brachiopod fragments and crinoid columnals, and fine terrigenous clastics. Calcite-rich areas show intercrystalline porosity (white arrow). Well 100/15-24-039-21W4/00, 1635.55 m, 2.5X, crossed polars. d) LF6: 100 µm pores (Po; missing blue epoxy) surrounded by rhombic dolomite (D) showing intracrystalline porosity. Well 100/15-24-039-21W4/00, 1635.55 m, 10X, crossed polars. e) LF7: Fine-grained terrigenous clastics (dark) surrounding coarse dolomite (D), some defining circular bioclasts or burrows. Stained coarse, blocky calcite spar (C) occludes porosity in the dolomite. Well 100/16-26-039-24W4/00, 1853.2 m, 2.5X, plane polarized. f) LF7: Dolomite rhombohedrons (D) surrounding a pore occluded by coarse, blocky calcite spar (C) and lesser brightly birefringent anhydrite (An). Well 100/16-26-039-24W4/00, 1853.2 m, 10X, crossed polars.

5 Discussion and Future Work

5.1 Leduc Formation CO_2 Capacity Estimates

The distribution of the Leduc Formation buildup complexes within the study area is well-known, as these carbonates have been the focus of conventional oil exploration and production for many decades. Previous CCUS studies focussing specifically on the Leduc Formation within Alberta are limited (Gunter et al., 2009; Bachu et al., 2011), with most of the work including the Leduc within regional-scale suitability studies focussing on the sedimentary basin as a whole (Bachu et al., 2000). Other studies have focused on existing oil and gas pools, including those in the Leduc Formation, proximal to point-source emitters (Bachu, 2003; Bachu and Shaw, 2005; Bachu et al., 2014; Hares, 2020). The Heartland Area Redwater Project (Bachu et al., 2011) is the most detailed study on one of the Leduc-Ireton storage complexes in Alberta. It included a multi-year core logging and mapping program to define facies belts within the buildup, supporting improved correlation between rock properties and associated fluid properties. This subdivision allows for a more effective capacity estimation of CO_2 storage by capturing the complexity of these Devonian buildups, which can then be modelled more accurately (Bachu et al., 2011). The other capacity estimation studies only consider depleted oil and gas pools within a small number of Leduc buildups (Bachu, 2003, 2004; Jafari and Bachu, 2014). These hydrocarbon pools comprise only a limited portion of the Leduc Formation (recall Figure 12), and therefore this present study provides a more complete picture of CO_2 sequestration potential, in saline aquifer systems, across a large part of central Alberta.

CO_2 storage capacity within the Leduc Formation carbonates was estimated using the fluid substitution and DOE-NETL volumetric methods (see Appendix 3 for results). Each method has its limitations for assessing storage capacity but the results from the DOE-NETL method in this study may underestimate storage capacity. This is suggested by the benchmarking against CO_2 injection and sequestration results at Clive Field and comparison against the results obtained with the fluid substitution method. Assumptions related to the efficiency factor are probably the main cause for underestimation, but other factors may include model resolution, mapping of the buildup edges, and modelling of the log-calculated porosity.

The fluid substitution methodology requires knowledge of recoveries from the various oil and gas pools (associated and non-associated) within the Leduc Formation. The pools across the study area have produced a significant amount of hydrocarbons. The cumulative oil and gas reserves in pools with recoveries >10 000 10^3m^3 approach 400 000 10^3m^3 (2516 mmbbl; million oil barrels) (recall Table 4). The Redwater Leduc buildup produced more than 134 000 10^3m^3 (842 mmbbl). Significant non-associated gas has also been recovered from accumulations across the study area. Recoveries in these gas pools >1000 10^6m^3 total more than 103 000 10^6m^3 (3637 bcf; billion standard cubic feet), with the Ricinus "West" gas pool (previously presented in Figure 2) producing more than 48 000 10^6m^3 (1695 bcf) (recall Table 5).

Mass estimates of the CO_2 storage capacity from the fluid substitution method surpass 632.9 million tonnes (Mt) within the Leduc oil or associated oil and gas pools (Appendix 2, Table B3), and 184.5 Mt within the gas pools (Appendix 2, Table B5). Estimates for the largest oil and gas pool by recovery, Redwater Leduc, are greater than 15.3 Mt of CO_2. Estimates from the largest non-associated gas pool, Ricinus 'west', are greater than 83 Mt of CO_2. This only reflects a small portion of the total potential when the saline aquifer portion of the buildups is considered.

The DOE-NETL methodology for oil and gas reservoirs was applied to 80 pools (associated and non-associated). The aggregated P_{50} estimate for the total mass of sequestered CO_2 for these pools is 348.9 Mt, with a P_{10} to P_{90} range of 267.2 to 445.5 Mt. The P_{50} estimate is considerably lower than the 793 Mt estimated using the fluid substitution method for the 53 pools common to both analyses (Appendix 3, Table C1). Comparing the results of the two methods at individual buildups (recall Figure 9 and Figure 11), it is found that the fluid substitution method generally yields larger storage-capacity estimates than the DOE-NETL method. Obvious exceptions are noted at the Redwater, Pembina D3-A, Homeglen-Rimbey, and Lone Pine Creek pools, but the cause of these exceptions is not known. Interestingly, the

discrepancy between the capacity estimate trends, with the fluid substitution method generally providing larger estimates, tends to expand towards the smaller hydrocarbon pools (previously presented in Figure 9). The substitution results are broadly consistent with those reported by Bachu (2004), which is expected given the similarity of the underlying methodologies (Figure 9). A possible explanation for the growing discrepancy toward smaller pool sizes between the DOE-NETL and fluid substitution results (Figure 9) may lie in the resolution of the 3D geocellular model. As the pool sizes decrease, so does the polygon used to define the boundaries of these pools (recall Figure 2). A small polygon may produce a small number of cells within the model, especially if the hydrocarbon pool height is also small, such that the representative volume of Leduc is underestimated.

Mass estimates for CO_2 within the saline aquifer portions of the Leduc buildups are immense, totalling 1.66 gigatonnes (Gt) for the P_{50} estimate, with a P_{10} to P_{90} range of 471.9 Mt to 4006.0 Mt, respectively. There are 23 separate buildups that were considered contiguous during the modelling stage (recall Figure 10). The largest individual saline aquifer within the Leduc is the Homeglen-Rimbey-Bashaw complex that is interpreted to be connected through the southernmost part of that complex (recall Figure 11). This saline aquifer alone has a P_{50} mass estimate of 1218.6 Mt, representing 74% of the total estimated saline aquifer capacity in the study area. The next largest buildup is Morinville (P_{50} = 170.4 Mt), followed by Redwater (P_{50} = 75.7 Mt) (Figure 10 and Figure 11). The Morinville buildup is not fully characterized in this study, as its northern part was truncated for the purposes of constraining the study area to the 1000 m depth constraint for supercritical CO_2 storage considerations. Depending on the hydrocarbon accumulations within the individual Leduc buildups along the Rimbey-Meadowbrook reef trend, the saline aquifer versus the hydrocarbon pool estimates vary considerably, with a number of the buildups having the greatest capacity within the hydrocarbon leg (e.g., Bonnie Glen and Wizard Lake, Figure 11). When compared to the hydrocarbon portion, the saline aquifer estimations contain the most uncertainty, largely due to the paucity of deeper well control outside of the pools. Future work involving capacity estimations should involve considerations of facies tied to rock properties. This would greatly enhance the understanding of flow units tied to buildup architecture within the Leduc Formation.

An important consideration for CO_2 sequestration in depleted hydrocarbon reservoirs within the Leduc Formation is the potential for aquifer support to the buildups from the underlying Cooking Lake aquifer. The Cooking Lake Formation is a broad carbonate platform complex that underlies all Leduc buildups within the study area (recall Figure 1 and Figure 11). Previous studies have shown that in the region that includes the Redwater Leduc and Morinville buildups (recall Figure 2), the Leduc and Cooking Lake are in strong hydrodynamic communication (Bachu et al., 2011). This study suggests that the aquifer support is predominantly through the westernmost part of the Redwater buildup where it is dolomitized along with the underlying Cooking Lake. Hydrogeological studies of pre- and post-production hydraulic heads show changes in water-flow directions in the Cooking Lake toward the Redwater buildup after production (Bachu et al., 2011). Since many of the Leduc buildups in the study area are heavily dolomitized along with the underlying Cooking Lake (i.e., all the Rimbey-Meadowbrook reef trend), they are also likely in hydrodynamic communication with significant aquifer support (Potma, *pers. comm.*). Strong aquifer support can reduce storage capacity of oil pools and gas pools by up to 50% and 30%, respectively (Bachu and Shaw, 2005). Such aquifer support will also be relevant for sequestration within the saline aquifer portions of the Leduc buildups.

A limitation of the current study is the delineation of the hydrocarbon versus saline aquifer portions of the Leduc buildups. Production databases provide information on hydrocarbon-water contacts at the time of discovery and therefore represent only an early snapshot of the petroleum-aquifer system. Considering these pools have been producing for multiple decades, the encroachment of the saline aquifer system during and after production means that present-day fluid distributions differ considerably from those at discovery. As a result, the hydrocarbon-water contacts used to subdivide the buildups for capacity estimations are unlikely to represent current conditions.

5.2 Ireton Formation Caprock Assessment

The presence of a competent aquitard in the form of the Ireton Formation is an important component of a potential CO_2 sequestration project within the Leduc-Ireton storage complex. The thickness of the Ireton Formation varies greatly over the Leduc buildup complexes (recall Figure 5). In addition to areas with no Ireton deposited, many areas have Ireton thicknesses less than 10 m. All of these areas are found in the southern part of the study area roughly south of Township 43, as marked in Figure 5. Although areas on the Bashaw complex have Ireton less than 10 m—even missing in regions—the Leduc has still trapped hydrocarbons for geological time in regions proximal to the thin or missing Ireton (cf. Hearn et al. 2011). For example, the Clive Field (Number 26, recall Figure 2) has trapped oil and gas within the Leduc Formation despite having an Ireton thickness of less than 10 m (Figure 5). Hearn et al. (2011) point to strong evidence for the breaching of the Ireton aquitard in areas proximal to this field. Therefore, containment by the Ireton Formation is a complex phenomenon that requires more than an arbitrary thickness cut-off for perceived aquitard competency. Areas with thin Ireton and relatively carbonate-rich facies still have the capacity to trap a CO_2 plume, albeit a CO_2 column with smaller heights relative to thicker, shalier Ireton intervals. There are numerous hydrocarbon accumulations across the Bashaw complex where the Ireton is relatively thin to absent (recall Figure 4) and contains an abundance of carbonate-rich lithofacies. Many of these accumulations have relatively small hydrocarbon column heights relative to pools from the Rimbey-Meadowbrook reef trend (see Figure 17 of Hearn et al., 2011). The lack of significant column heights here may point to hydrocarbon breaching of the Ireton Formation (Hearn et al., 2011). Indeed, the three lowest threshold pressures measured from the Ireton come from this area (samples 16-26-3, 15-29-1, and 16-26-2, recall Table 14). Since one of these samples (i.e., sample 15-29-2, lithofacies 2) is relatively clay-rich and dolomitized, dolomitization must play a role in porosity and permeability development within the Ireton in these areas.

Based on logged core, the Ireton Formation over top of Leduc buildups consists of seven lithofacies (LF1–LF7), ranging from pure terrigenous clastics (see litholog 100/06-22-038-24W4/00 in Appendix 4 and corresponding XRF-derived values for LF1) to fossil-bearing floatstones. These facies do not include the deeper water facies that are present in the Ireton Formation from off-platform deeper water depositional environments (Stoakes, 1980; Hearn et al., 2011). Fluctuations in relative sea level during Ireton deposition over the buildups likely resulted in pronounced shifts in facies due to the relative low accommodation compared to basinal areas. These fluctuations can be pronounced in areas of thin Ireton (e.g., lithologs 100/06-22-038-24W4/00 and 100/15-29-039-21W4/00 in Appendix 4).

Based on thin sections and XRF analyses, the Ireton is composed of the minerals calcite, dolomite, quartz, potassium feldspar, clays (illite), pyrite, and anhydrite. The proportion of carbonates to siliciclastics is controlled by original depositional processes and resulting facies. Dolomite, pyrite, and anhydrite are early- to late-stage diagenetic minerals. Some level of dolomitization was noted in all carbonate-bearing Ireton facies from across the study area, although it was most pervasive in locations on the Bashaw and Fenn-Big Valley complexes. Here, dolomitization was likely a syndepositional to early burial event through brine reflux from the overlying evaporitic Nisku Formation (Tan, 1998; Potma et al., 2001; Hearn et al., 2011).

Microscopic textures from the Ireton Formation reveal that much of the calcite component consists of anhedral to subhedral mosaics mixed with siliciclastics—either separately laminated/bedded or admixed through bioturbation. In these areas porosity tends to be too small to observe at the scale of microscopy (up to 200X magnification), with the exception of thin sections from LF6 displaying intercrystalline porosity, which is bioclastic and therefore may be more prone to fluid flow and diagenesis (recall Figure 15c). Thin sections that are heavily dolomitized show intercrystalline porosity (e.g., recall Figure 14e). Distinct rhombohedral fabrics in dolomite are pervasive near and along the edges of previous pores—which are most often occluded by later-stage cements such as calcite, anhydrite, and pyrite (recall Figures 13c, d, 14a, b, f, and 15e, f). While anhydrite acts to occlude pores, it is not a common phase, except for LF5 where it forms diagenetic nodules replacing areas within distinct calcite laminae

(Figures 12 and 15b). More rarely pores remain open (Figure 14c), which may be associated with a dissolution event that culminated in a common porosity type: intracrystalline porosity within dolomite rhombs (Figures 13c, d, f, 14d and 15d). In many dolomite rhombs this intracrystalline porosity appears to align with zones parallel to the rhombohedral crystal axes (Figures 13d and 14d). This may indicate that the dolomite rhombs are compositionally zoned—either with low- to high-calcium (calcian) dolomite or iron-bearing (ferroan) dolomite—that was subjected to fluctuations in pore-water chemistry that dissolved particular zones during later stages of diagenesis (Jones, 2004).

The MICP results are variable as expected since they were measured in seven lithofacies from the Ireton Formation. The MICP results generally track the trend in relative carbonate and clay content, with higher entry and threshold pressures correlating to more clay-rich facies, although not always. As capillary pressure is an indicator of pore throat size, entry pressure corresponds to the largest pore throat. In the Ireton samples, measured entry pressures show no clear relationship with Ireton lithofacies (recall Table 14). Clay-rich facies can have lower entry pressures than carbonate-rich facies. For example, sample 15-29-1 is from LF2 and has slightly lower entry pressures than sample 16-26-1 from LF7 (Table 14). From thin section, it is apparent that sample 15-29-1 is heavily dolomitized (recall Figure 13b), and with abundant intracrystalline porosity within dolomite rhombs (Figure 13c, d). These observations suggest that porosity and permeability trends are influenced by diagenesis, even in clay-rich samples where carbonate components may be susceptible to dolomitization. However, higher carbonate content may also promote porosity reduction through replacive anhydritization (e.g., LF5, recall Figure 15a, b).

Entry pressures and threshold pressures can be quite different (recall Table 14), which reflects the complexity in pore throats and ultimately permeability within the Ireton samples. While threshold pressures are always higher than entry pressures, small differences reflect homogeneity within pores in a given sample. For example, sample 16-26-3 was taken from LF4 near the Clive Field in the Bashaw complex (recall Figure 4). This sample is carbonate-rich (clay-lean), and in thin section displays relatively coarse mosaics of dolomite with intercrystalline porosity (recall Figure 14e)—a fabric that appears to homogenize the pores within this sample. Lucia (2004) suggests that dolomitization can result in dolomite crystals that are larger than the precursor limestone mud, which can substantially improve porosity and permeability. This appears to be the case in samples with pervasive dolomitization in carbonate-rich facies of the Ireton Formation.

Hydrocarbon accumulations within isolated Leduc buildups along the Rimbey-Meadowbrook reef trend have been effectively sealed by the Ireton despite having hydrocarbon column heights in excess of 200 m (see Stoakes and Creaney, 1985). Within the Strachan buildup (recall Figure 2), the Leduc displays abundant evidence of intense pressures from hydrocarbon maturation from oil to gas in the form of bitumen-stained microfractures (Márquez and Mountjoy, 1996). Despite the overpressuring within this buildup, the overlying Ireton (~25 m thick) has formed an effective seal. Entry pressures and threshold pressures from this work at Strachan are some of the highest measured, at 174.4 psi and 733.1 psi, respectively, which suggests sufficient sealing capacity despite reservoir overpressuring.

5.3 Summary

This study has enhanced our understanding of the potential for CO_2 sequestration in both hydrocarbon pools and saline aquifer intervals of the Leduc Formation, including the first regional CO_2 sequestration capacity estimate for saline aquifer portions of these Devonian carbonate buildups. The results show that there is substantial potential capacity for CO_2 sequestration within the Leduc Formation in central Alberta, whether by sequestration in saline aquifers or through enhanced oil recovery in abandoned/depleted oil pools. The total P_{50} capacity estimate for the hydrocarbon pools and saline aquifers within the Leduc Formation in the study area is greater than 2.01 gigatonnes of CO_2. This estimate far exceeds the annual emissions in Alberta at 260 megatonnes as of 2024 and demonstrates the formation's potential to significantly contribute to Canada's net-zero emissions plans. Capacity estimations across the entirety of

the Leduc Formation, not just the hydrocarbon pools, may also aid in evaluating other pore-space or fluid-use activities in these buildups outside of CO_2 sequestration, including geothermal development, lithium recovery from brines, and water disposal.

The Leduc Formation has been a prolific oil and gas reservoir across the study area. This fact alone points to the competency of the overlying Ireton Formation as a seal to these fluids. The results of lithofacies and MICP analyses together suggest that much of the Ireton contains facies with high entry and threshold pressures that can contain significant CO_2 column heights. In the southern part of the study area, the Ireton Formation thins considerably and can become more carbonate-rich. In these areas, certain parts of the Ireton have lower capillary entry pressures where the calculated CO_2 column heights are significantly reduced.

6 References

Amthor, J.E., Mountjoy, E.W. and Machel, H.G. (1994): Regional-scale porosity and permeability variations in Upper Devonian Leduc buildups: implications for reservoir development and prediction in carbonates; Bulletin of the American of Petroleum Geologists, v. 78, p. 1541–1558.

Andrichuck, J.M. (1958): Stratigraphy and facies analysis of Upper Devonian reefs in Leduc, Stettler, and Redwater areas, Alberta; American Association of Petroleum Geologists Bulletin, v. 24, p. 1–93.

Atchley, S.C., West, L.W. and Sluggett, J.R. (2006): Reserves growth in a mature oil field: the Devonian Leduc Formation at Innisfail field, south-central Alberta, Canada; American Association of Petroleum Geologists Bulletin, v. 90, p. 1153–1169.

Bachu, S. (2003): Capacity for carbon dioxide sequestration in Alberta's oil and gas reservoirs; Final Report to Alberta Science and Research Authority, EUB-AGS, 59 p.

Bachu, S. (2004): Evaluation of CO_2 sequestration capacity in oil and gas reservoirs in the Western Canada Sedimentary Basin; Client Report to AERI and NRCan, 77 p.

Bachu, S. and Gunter, W.D. (2004): Acid-gas injection in the Alberta Basin, Canada: a CO_2-storage experience; Geological Society of London, Special Publication 233, p. 225–234.

Bachu, S. and Shaw, J.C. (2005): CO_2 storage in oil and gas reservoirs in western Canada: effect of aquifers, potential CO_2-flood enhanced oil recovery and practical capacity; *in* E.S. Rubin, D.W. Keith, and C.F. Gilboy (ed.), Proceedings of the 7th International Conference on Greenhouse Gas Control Technologies (GHGT-7), v. 1: Peer-Reviewed Papers and Overviews; Elsevier, p. 361–369.

Bachu, S., Brulotte, M., Grobe, M. and Stewart, S. (2000): Suitability of the Alberta subsurface for carbon-dioxide sequestration in geological media; Alberta Energy and Utilities Board, EUB/AGS Earth Sciences Report 2000-11, 88 p.

Bachu, S., Buschkuehle, B.E., Haug, K. and Michael, K. (2008): Subsurface characterization of the Edmonton-area acid-gas injection operations; Energy Resources Conservation Board, ERCB/AGS Special Report 092, 134 p.

Bachu, S., Brydie, J., Hauck, T.E., Lakeman, B., Palombi, D., Stoakes, F., Wendte, J., Lawton, D., Darvish, M-P., Hawkes, C., Chalaturnyk, R., Krawec, T. and Sawchuk, W. (2011): The Heartland Area Redwater CO_2 storage project (HARP): results of Phase I site characterization; Energy Procedia, GHGT 10, v. 4, p. 4559–4566.

Bachu, S., Melnik, A. and Bistran, R. (2014): Approach to evaluating the CO_2 storage capacity in Devonian deep saline aquifers for emissions from oil sands operations in the Athabasca area, Canada; Energy Procedia, GHGT 12, v. 63, p. 5093–5102.

Bahadori, A., Vuthaluru, H.B., and Mokhatab, S. (2009): New correlations predict aqueous solubility and density of carbon dioxide; International Journal of Greenhouse Gas Control, v. 3, p. 474-480.

Brinsky, J. (2023): Distribution of hydraulic head in the Leduc hydrostratigraphic unit (tabular data, tab-delimited format); Alberta Energy Regulator / Alberta Geological Survey, AER/AGS Digital Data 2021-0028.

Daniel, R.F. and Kaldi, J.G. (2009): Evaluating seal capacity of cap rocks and intraformational barriers for CO_2 containment; *in* M. Grobe, J. C. Pashin, and R. L. Dodge (ed.), Carbon Dioxide Sequestration in Geological Media—State of the Science, AAPG Studies in Geology 59, p. 335–345.

Davies, G.R. and Smith, L.B.Jr. (2006): Structurally controlled hydrothermal dolomite reservoir facies: an overview; American Association of Petroleum Geologists Bulletin, v. 90, p. 1641–1690.

Dewhurst D.N., Jones, R.M. and Raven, M.D. (2002): Microstructural and petrophysical characterization of Muderong Shale: application to top seal risking; Petroleum Geoscience, v. 8, p. 371–383.

Drivet, E. and Mountjoy, E.W. (1997): Dolomitization of the Leduc Formation (Upper Devonian), southern Rimbey-Meadowbrook reef trend, Alberta; Journal of Sedimentary Research, v. 67, p. 411–423.

Enhance Energy Inc. and North West Redwater Partnership (2011): Division B: detailed report; 145 p.

Enhance Energy Inc. (2025): Clive D-2A and D-2A Enhanced Oil Recovery Project; 2025 Annual Report, 319 p.

Enhance Energy Inc. (2026): Clive D-2A and D-2A Enhanced Oil Recovery Project; 2025 Annual Report, 354 p.

Gilhooly, M.G. (1987): Sedimentology and geologic history of the Upper Devonian (Frasnian) uppermost Ireton and Nisku formation, Bashaw area, Alberta; M.Sc. thesis, University of Calgary, Alberta, 220 p.

Goodman, A., Hakala, A., Bromhal, G., Deel, D., Rodosta, T., Frailey, S., Small, M., Allen, D., Romanov, V., Fazio, J., Huerta, N., McIntyre, D., Kutchko, B, and Guthrie, G. (2011): US DOE methodology for the development of geologic storage potential for carbon dioxide at the national and regional scale; International Journal of Greenhouse Gas Control, v. 5, p. 952-965.

Goodman, A., Sanguinito, S. and Levine, J.S. (2016): Prospective CO_2 saline resource estimation methodology: refinement of existing US-DOE-NETL methods based on data availability; International Journal of Greenhouse Gas Control, v. 54, p. 242–249, doi:10.1016/j.ijggc.2016.09.009.

Gray, M.E. (2017): Analytical techniques for evaluating seal capacity for carbon dioxide storage in selected Australian basins; Ph.D. thesis, University of Adelaide, Australian School of Petroleum, 488 p.

Green, D.G. and Mountjoy, E.W. (2005): Fault and conduit controlled burial dolomitization of the Devonian west-central Alberta deep basin; Bulletin of Canadian Petroleum Geology, v. 53, p. 101–129.

Gunter, W.D., Bachu, S., Buschkuehle, M., Michael, K., Ordorica-Garcia, G. and Hauck, T. (2009): Reduction of GHG emissions by geological storage of CO_2: anatomy of the Heartland Aquifer Redwater Carbon Capture and Geological Storage Project (HARP), Alberta, Canada; International Journal of Climate Change Strategies and Management, v. 1, p. 160–178. doi:10.1108/1756869091955621.

Haagsma, A., Main, J., Pasumarti, A., Valluri, M., Scharenberg, M., Larsen, G., Goodman, W., Harrison, W., Mishra, S., Pardini, R. and Gupta, N. (2020): A comparison of carbon dioxide storage resources estimate methodologies for a regional assessment of the Northern Niagaran Pinnacle Reef Trend in the Michigan Basin; Environmental Geosciences, v. 27, p. 9–23, doi:10.1306/eg.11051919019.

Hares, R. (2020): Feasibility of CCUS to CO_2-EOR in Alberta; Unpublished M.Sc. thesis, University of Calgary, 100 p.

Hearn, M.R., Machel, H.G. and Rostron, B.J. (2011): Hydrocarbon breaching of a regional aquitard: the Devonian Ireton Formation, Bashaw area, Alberta, Canada; American Association of Petroleum Geologists Bulletin, v. 95, p. 1009–1037.

International Energy Agency Greenhouse Gas R&D Programme (IEAGHG). (2009): Development of storage coefficients for CO_2 storage in deep saline formations; 2009-13, November 2009.

Security Classification: Protected A

Jafari, A. and Bachu, S. (2014): Evaluation of CO_2 storage capacity in Devonian hydrocarbon reservoirs for emissions from oil sands operations in the Athabasca area, Canada; Energy Procedia, v. 63, p. 5222–5230.

Jones, B. (2004): Petrography and significance of zoned dolomite cements from the Cayman Formation (Miocence) of Cayman Brac, British West Indies; Journal of Sedimentary Research, v. 74, p. 95–109.

Kawaura, K., Akaku, K., Nakano, M., Ito, D., Takahashi, T., and Kiriakehata, S., (2013): Examination of methods to measure capillary threshold pressures of pelitic rock samples; Energy Procedia, v. 37, p. 5411–5418.

Kivior T., Kaldi J.G. and Lang S.G. (2002): Seal potential in Cretaceous and late Jurassic rocks of the Vulcan sub-basin, Northwest shelf Australia; The APPEA Journal, v. 42, p. 203–224.

Klovan, J.E. (1964): Facies analysis of the Redwater reef complex, Alberta, Canada; Bulletin of Canadian Society of Petroleum Geologists, v. 12, p. 1–100.

Lucia, F.J. (2004): Origin and petrophysics of dolostone pore space, in C.J.R. Braithwaite, G. Rizzi and G. Darke (ed.), The geometry and petrogenesis of dolomite hydrocarbon reservoirs, Geological Society of London Special Publications, v. 235, p. 141–155.

Márquez, X.M. and Mountjoy, E.W. (1996): Microfractures due to overpressures caused by thermal cracking in well-sealed Upper Devonian reservoirs, deep Alberta Basin; American Association of Petroleum Geologists Bulletin, v. 80, p. 570–588.

McGillivray, J.G. and Mountjoy, E.W. (1975): Facies and related reservoir characteristics Golden Spike reef complex, Alberta; Bulletin of Canadian Petroleum Geology, v. 23, p. 753–809.

Mossop, G.D. (1972): Origin of the peripheral rim, Redwater Reef, Alberta. Bulletin of Canadian Petroleum Geology; v. 20, p. 238–280.

Mountjoy, E.W., Green, D.G., Machel, H.G., Duggan, J. and Williams-Jones, A.E. (1999): Devonian matrix dolomites and deep burial carbonate cements: a comparison between the Rimbey-Meadowbrook reef trend and the deep basin of west-central Alberta; Bulletin of Canadian Petroleum Geology, v. 47, p. 487–509.

Oliver, T.A. and Cowper, N.W. (1963): Depositional environments of the Ireton Formation, central Alberta; Bulletin of Alberta Society of Petroleum Geologists, v. 11, p. 183–202.

Potma, K., Wong, P.K., Weissenberger, J.A.W. and Gilhooly, M.G. (2001): Toward a sequence stratigraphic framework for the Frasnian of the Western Canada Basin; Bulletin of Canadian Petroluem Geology, v. 49, p. 37–85.

Sanguinito, S., Singh, H., Myshakin, E.M., Goodman, A.L., Dilmore, R.M., Grant, T.C., Morgan, D., Bromhal., G., Warwick, P.D., Brennan, S.T., Freeman, P.A., Karacan, C.Ö., Gorecki, C., Peck, W., Burton-Kelly, M., Dotzenrod, N., Frailey, S. and Pawar, R. (2020): Methodology for estimating the prospective CO_2 storage resource of residual oil zones at the national and regional scale; International Journal of Greenhouse Gas Control, v. 96, p. 1–8, doi:10.1016/j.ijggc.2020.103006.

Span, R. and Wagner, W. (1996): A new equation of state for carbon dioxide covering the fluid region from the triple-point temperature to 1100 K at pressures up to 800 MPa; Journal of Physical and Chemical Reference Data, v. 25, p. 1509–1596, doi:10.1063/1.555991.

Stacey, J., Hollis, C., Corlett, H. and Koeshidayatullah, A. (2020): Burial dolomitization driven by modified seawater and basal aquifer-sourced brines: insights from the Middle and Upper Devonian of the Western Canadian Sedimentary Basin; Basin Research, v. 33, p. 648–680.

Stieber, S.J. (1970): Pulsed neutron capture log evaluation – Louisiana Gulf Coast; American Institute of Mining, Metallurgical Petroleum Engineers, SPE 2961, 7 p.

Stoakes, F.A. (1980): Nature and control of shale basin fill and its effect on reef growth and termination: upper Devonian Duvernay and Ireton formations of Alberta, Canada; Bulletin of Canadian Petroleum Geology, v. 28, p. 345–410.

Stoakes, F.A. (1992): Woodbend megasequence; *in* J.C. Wendte, F.A. Stoakes and C.V. Campbell (ed.), Devonian–Early Mississippian carbonates of the Western Canada Sedimentary Basin: a sequence stratigraphic framework, Society of Economic Paleontologists and Mineralogists Short Course No. 28, Calgary, June 20–21, p. 207–224.

Stoakes, F.A. and Creaney, S. (1985): Sedimentology of a carbonate source rock: the Duvernay Formation of Alberta, Canada; *in* M.W. Longman, K.W. Shanley, R.G. Lindsay and D.E. Eby (ed.), Rocky Mountain carbonate reservoirs: a core workshop; SEPM Core Workshop Notes 7, doi:10.2110/cor.85.07.0343.

Stoakes, F.A. and Wendte, J.C. (1987): The Woodbend Group; *in* F.F. Krause and O.G. Burrowes (ed.), Devonian lithofacies and reservoir styles in Alberta, 13th Canadian Society of Petroleum Geologists Core Conference, Guidebook, p. 153–170.

Switzer, S.B., Holland, W.G., Christie, D.S., Graf, G.C., Hedinger, A.S., McAuley, R.J., Wierbicki, R.A. and Packard, J.J. (1994): Devonian Woodbend-Winterburn strata of the Western Canada Sedimentary Basin; *in* G. Mossop and I. Shetsen (comp), Geological atlas of the Western Canada Sedimentary Basin; Calgary, Canada, Canadian Society of Petroleum Geologists and Alberta Research Council, p. 165–202.

Tan, W. (1998): Origins of replacement dolomites, Upper Devonian Leduc, Nisku and Wabamun formations, southeastern Alberta, Western Canada Sedimentary Basin; PhD thesis, McGill University, Montreal, Canada. 348 p.

Walls, R.A., Mountjoy, E.W. and Fritz, P. (1979): Isotopic composition and diagenetic history of carbonate cements in the Devonian Golden Spike reef, Alberta; Geological Society of America Bulletin, v. 90, p. 41–88.

Wong, P.K., Weissenberger, J.A.W. and Gilhooly, M.G. (2016): Revised regional Frasnian sequence stratigraphic framework, Alberta outcrop and subsurface; *in* T.E. Playton, C. Kerans and J.A.W. Weissenberger (ed.), New advances in Devonian carbonates: outcrop analogs, reservoirs, and chronostratigraphy, SEPM Special Publication 107, doi:10.2110/sepmsp.107.05.

Appendix 1 – Leduc Formation Hydrocarbon Pool Ultimate Recovery Tables

Table A1. Oil and gas reservoirs with ultimate recoveries greater than 5000 10^3m^3.

Pool Name	Area	OOIP	OGIP	Ultimate Recovery
	(ha)	(10^3m^3)	(10^6m^3)	(10^3m^3)
ACHESON D-3 A	2084	29 708.9	77.0	21 549.4
BONNIE GLEN D-3 A	2759	124 998.6	0.0	82 749.1
CLIVE D-3 A	4280	12 355.2	0.0	8201.3
GOLDEN SPIKE D-3 A	596	50 173.4	0.0	29 060.3
HOMEGLEN-RIMBEY D-3	4 682	12 394.9	0.0	5205.9
INNISFAIL D-3	3 136	19 486.4	0.0	13 601.5
LEDUC-WOODBEND LEDUC A	8 828	53 950.0	0.0	40 224.9
REDWATER D-3	17 236	198 018.3	0.0	134 627.2
WESTEROSE D-3	848	32 037.6	0.0	23 707.8
WIMBORNE-D-3 A	6834	13 000.6	0.0	5460.3
WIZARD LAKE D-3 A	1177	63 899.6	0.0	54 186.8
Total	52 460	610 024.0	77.0	418 574.5

Table A2. Oil and gas reservoirs with ultimate recoveries greater than 1000 10^3m^3.

Pool Name	Area	OOIP	OGIP	Ultimate Recovery
	(ha)	(10^3m^3)	(10^6m^3)	(10^3m^3)
ACHESON D-3 A	2084	29 708.9	77.0	21 549.4
BASHAW D-3 A	1859	2588.3	0.0	1022.2
BONNIE GLEN D-3 A	2759	124 998.6	0.0	82 749.1
CLIVE D-3 A	4280	12 355.2	0.0	8201.3
DUHAMEL D-3 B	259	2238.4	0.0	1475.1
ERSKINE D-3	1865	6244.7	0.0	4121.5
FAIRYDELL-BON ACCORD D-3 A	425	2908.2	0.0	2006.7
FENN-BIG VALLEY D-3 F	637	2999.4	13.0	2339.5
GLEN PARK D-3 A	315	5727.9	0.0	3436.7
GOLDEN SPIKE D-3 A	596	50 173.4	0.0	29 060.3
HAYNES D-3 A	49	2841.6	0.0	1051.4
HOMEGLEN-RIMBEY D-3	4682	12 394.9	0.0	5205.9
INNISFAIL D-3	3136	19 486.4	0.0	13 601.5
LEDUC-WOODBEND LEDUC A	8828	53 950.0	0.0	40224.9
LEDUC-WOODBEND D-3 B	729	2380.5	0.0	1297.7
MORINVILLE D-3 B	329	3336.8	0.0	1780.0
PEMBINA D-3 A	5282	6502.0	0.0	2535.8
REDWATER D-3	17 236	198 018.3	0.0	134 627.2
ST ALBERT-BIG LAKE D-3 A	63	3699.5	0.0	2334.4
STETTLER D-3 A	1961	6266.4	0.0	3822.5

Pool Name	Area (ha)	OOIP (10^3m^3)	OGIP (10^6m^3)	Ultimate Recovery (10^3m^3)
WESTEROSE D-3	848	32 037.6	0.0	23 707.8
WIMBORNE D-3 A	6834	13 000.6	0.0	5460.3
WIZARD LAKE D-3 A	1177	63 899.6	0.0	54 186.8
Total	66 233.0	657 575.2	90.0	445 798.0

Table A3. Oil and gas reservoirs with ultimate recoveries greater than 100 10^3m^3.

Pool Name	Area (ha)	OOIP (10^3m^3)	OGIP (10^6m^3)	Ultimate Recovery (10^3m^3)
ACHESON D-3 A	2084	29 708.9	77.0	21 549.4
BASHAW D-3 A	1859	2588.3	0.0	1022.2
BONNIE GLEN D-3 A	2759	124 998.6	0.0	82 749.1
BUFFALO LAKE D-3	69	1410.2	0.0	915.2
BUFFALO LAKE D-3 B	111	1020.8	0.0	714.6
CHIGWELL D-3 B	124	639.1	0.0	180.6
CLIVE D-3 A	4280	12 355.2	0.0	8201.3
DUHAMEL D-3 B	259	2238.4	0.0	1475.1
ERSKINE D-3	1865	6244.7	0.0	4121.5
EWING LAKE D-3 A	339	573.1	0.0	332.4
FAIRYDELL-BON ACCORD D-3 A	425	2908.2	0.0	2006.7
FENN-BIG VALLEY D-3 A	370	730.6	0.0	365.3
FENN-BIG VALLEY D-3 B	132	335.3	0.0	124.1
FENN-BIG VALLEY D-3 E	187	362.4	0.0	116.0
FENN-BIG VALLEY D-3 F	637	2999.4	13.0	2339.5
FENN-BIG VALLEY D-3 I	254	450.5	0.0	279.3
FENN WEST D-3 C	32	375.0	0.0	109.9
FENN WEST D-3 E	52	1883.2	0.0	642.2
GARRINGTON LEDUC G	64	1067.0	0.0	276.0
GARRINGTON LEDUC H	32	805.6	0.0	101.4
GHOST PINE D-3 A	226	1489.8	0.0	908.8
GLEN PARK D-3 A	315	5727.9	0.0	3436.7
GOLDEN SPIKE D-3 A	596	50 173.4	0.0	29 060.3
GOLDEN SPIKE D-3 B	113	683.0	0.0	284.8
GOLDEN SPIKE D-3 C	263	860.5	0.0	301.2
GOLDEN SPIKE D-3 D	370	1071.5	0.0	697.5
HAYNES D-3 A	49	2841.6	0.0	1051.4
HOMEGLEN-RIMBEY D-3	4682	12 394.9	0.0	5205.9
HOMEGLEN-RIMBEY D-3 B	108	699.4	0.0	124.5
INNISFAIL D-3	3136	19 486.4	0.0	13 601.5
LEDUC-WOODBEND LEDUC A	8828	53 950.0	0.0	40 224.9
LEDUC-WOODBEND D-3 B	729	2380.5	0.0	1297.7

Pool Name	Area (ha)	OOIP (10^3m^3)	OGIP (10^6m^3)	Ultimate Recovery (10^3m^3)
LEDUC-WOODBEND D-3 F	49	1100.4	0.0	594.2
LONE PINE CREEK D-3 A	2044	2034.0	0.0	233.9
MALMO D-3 A	240	1600.5	0.0	649.8
MEDICINE RIVER D-3 A	358	1305.6	0.0	261.1
MEDICINE RIVER D-3 D	53	723.1	0.0	216.9
MEDICINE RIVER D-3 F	69	1168.8	0.0	409.1
MIKWAN D-3 B	64	612.1	0.0	232.6
MORINVILLE D-3 B	329	3336.8	0.0	1780.0
MORINVILLE D-3 C	321	1163.8	0.0	139.7
MORINVILLE D-3 E	207	1070.3	0.0	342.5
MORINVILLE D-3 H	56	288.1	0.0	100.8
MORINVILLE-D-3 K	17	559.4	0.0	123.1
NEVIS D-3 E	117	478.0	0.0	191.7
NEW NORWAY D-3	80	317.8	0.0	113.5
PEMBINA D-3 A	5282	6502.0	0.0	2535.8
REDWATER D-3	17 236	198 018.3	0.0	134 627.2
RICH D-3 A	57	1559.7	0.0	619.2
ST ALBERT-BIG LAKE D-3 A	63	3699.5	0.0	2334.4
ST ALBERT-BIG LAKE D-3 B	115	1516.1	0.0	904.6
STETTLER D-3 A	1961	6266.4	0.0	3822.5
STETTLER D-3 B	73	448.0	0.0	295.7
SYLVAN LAKE D-3 B	367	944.1	0.0	188.8
SYLVAN LAKE D-3 C	54	572.6	0.0	143.2
WESTEROSE D-3	848	32 037.6	0.0	23 707.8
WIMBORNE D-3 A	6834	13 000.6	0.0	5460.3
WIZARD LAKE D-3 A	1177	63 899.6	0.0	54 186.8
Total	73 420.0	68 967.6	90.0	458 032.2

Table A4. Non-associated gas reservoirs with ultimate recoveries greater than 500 10^6m^3.

Pool Name	Area (ha)	OIGP (10^6m^3)	Ultimate Recovery (10^6m^3)
BONNIE GLEN D-3 B	82	1129.0	903.0
FERRIER D-3 A	2011	39 474.0	37 500.0
FERRIER D-3 C	1025	3625.0	2030.0
HARMATTAN-ELKTON D-3 A	4613	10 833.0	3250.0
RICINUS D-3 A	1613	8635.0	3454.0
RICINUS D-3 B	64	2144.0	1822.0
RICINUS D-3 C	32	1175.0	940.0
RICINUS D-3 D	32	1055.0	897.0
RICINUS WEST D-3 A	2565	51 409.0	48 839.0

Pool Name		Area (ha)	OIGP (10^6m^3)	Ultimate Recovery (10^6m^3)
RICINUS WEST D-3 B		32	7222.0	6500.0
SYLVAN LAKE D-3 A		753	1034.0	517.0
	Total	12 822.0	127 735.0	106 652.0

Table A5. Non-associated gas reservoirs with ultimate recoveries greater than 100 10^6m^3.

Pool Name		Area (ha)	OGIP (10^6m^3)	Ultimate Recovery (10^6m^3)
BONNIE GLEN D-3 B		82	1129.0	903.0
FERRIER D-3 A		2011	39 474.0	37 500.0
FERRIER D-3 B		32	600.0	558.0
FERRIER D-3 C		1025	3625.0	2030.0
GARRINGTON LEDUC A		64	159.0	111.0
GARRINGTON LEDUC F		64	281.0	225.0
HARMATTAN-ELKTON D-3 A		4613	10 833.0	3250.0
RICINUS D-3 A		1613	8635.0	3454.0
RICINUS D-3 B		64	2144.0	1822.0
RICINUS D-3 C		32	1175.0	940.0
RICINUS D-3 D		32	1055.0	897.0
RICINUS WEST D-3 A		2565	51 409.0	48 839.0
RICINUS WEST D-3 B		32	7222.0	6500.0
SYLVAN LAKE D-3 A		753	1034.0	517.0
	Total	12 982.0	128 775.0	107 546.0

Appendix 2 – Fluid Substitution Results by Leduc Formation Pool

Table B1. Oil reservoirs with ultimate recoveries greater than 5000 10^3m^3.

Pool Name	CO_2 Capacity Estimate (at storage pressure)	
	G_{CO_2}	G_{CO_2}
	10^3m^3	Tonnes
ACHESON D-3 A	344 524.31	218 383 623.9
BONNIE GLEN D-3 A	111 034.0	83 423 831.0
CLIVE D-3 A	10 464.0	8 037 289.0
GOLDEN SPIKE D-3 A	168 790.87	121 608 758.8
HOMEGLEN-RIMBEY D-3	6062.0	4 859 199.0
INNISFAIL D-3	25 704.0	21 276 779.0
LEDUC-WOODBEND LEDUC A	44,236.0	29 957 203.0
REDWATER D-3	95 061.3	15 304 861.5
WESTEROSE D-3	34 229.0	26 546 381.0
WIMBORNE-D-3 A	8627.0	6 809 231.0
WIZARD LAKE D-3 A	62 542.0	46 989 877.0
Total	911 274.4	583 197 034.2

Table B2. Oil reservoirs with ultimate recoveries greater than 1000 10^3m^3.

Pool Name	CO_2 Capacity Estimate (at storage pressure)	
	G_{CO_2}	G_{CO_2}
	10^3m^3	Tonnes
ACHESON D-3 A	344 524.3	218 383 623.9
BASHAW D-3 A	3393.4	2 549 589.2
BONNIE GLEN D-3 A	111 034.0	83 423 831.0
CLIVE D-3 A	10 464.0	8 037 289.0
DUHAMEL D-3 B	5807.3	3 932 746.1
ERSKINE D-3	14 140.0	10 491 475.1
FAIRYDELL-BON ACCORD D-3 A	1391.2	469 533.3
FENN-BIG VALLEY D-3 F	2711.9	1 783 716.2
GLEN PARK D-3 A	3915.3	2 715 846.2
GOLDEN SPIKE D-3 A	168 790.9	121 608 758.8
HAYNES D-3 A	1428.2	1 073 061.1
HOMEGLEN-RIMBEY D-3	6062.0	4 859 199.0
INNISFAIL D-3	25 704.0	21 276 779.0
LEDUC-WOODBEND LEDUC A	44 236.0	29 957 203.0
LEDUC-WOODBEND D-3 B	5563.7	3 659 469.5

Pool Name		CO_2 Capacity Estimate (at storage pressure) G_{CO_2}	G_{CO_2}
		10^3m^3	Tonnes
MORINVILLE D-3 B		1519.6	1 029 084.9
PEMBINA D-3 A		3230.1	2 505 018.6
REDWATER D-3		95 061.3	15 304 861.5
ST ALBERT-BIG LAKE D-3 A		2653.2	1 600 300.3
STETTLER D-3 A		4063.1	2 575 475.5
WESTEROSE D-3		34 229.0	26 546 381.0
WIMBORNE D-3 A		8627.0	6 809 231.0
WIZARD LAKE D-3 A		62 542.0	46 989 877.0
	Total	961 091.5	617 582 350.1

Table B3. Oil reservoirs with ultimate recoveries greater than 100 10^3m^3.

Pool Name	CO_2 Capacity Estimate (at storage pressure) G_{CO_2}	G_{CO_2}
	10^3m^3	Tonnes
ACHESON D-3 A	344 524.3	218 383 623.9
BASHAW D-3 A	3393.4	2 549 589.2
BONNIE GLEN D-3 A	111 034.0	83 423 831.0
BUFFALO LAKE D-3	3925.8	2 582 136.9
BUFFALO LAKE D-3 B	2649.5	1 875 535.3
CHIGWELL D-3 B	203.1	155 982.3
CLIVE D-3 A	10 464.0	8 037 289.0
DUHAMEL D-3 B	5807.3	3 932 746.1
ERSKINE D-3	14 140.0	10 491 475.1
EWING LAKE D-3 A	352.0	238 354.0
FAIRYDELL-BON ACCORD D-3 A	1391.2	469 533.3
FENN-BIG VALLEY D-3 A	445.9	293 287.9
FENN-BIG VALLEY D-3 B	492.6	333 563.1
FENN-BIG VALLEY D-3 E	509.5	322 939.5
FENN-BIG VALLEY D-3 F	2711.9	1 783 716.2
FENN-BIG VALLEY D-3 I	335.0	220 345.9
FENN WEST D-3 C	101.2	70 195.0
FENN WEST D-3 E	654.9	443 477.8
GARRINGTON LEDUC G	593.7	506 571.7
GARRINGTON LEDUC H	191.2	162 403.7
GHOST PINE D-3 A	817.8	578 929.9
GLEN PARK D-3 A	3915.3	2 715 846.2

Pool Name	CO_2 Capacity Estimate (at storage pressure)	
	G_{CO_2}	G_{CO_2}
	$10^3 m^3$	Tonnes
GOLDEN SPIKE D-3 A	168 790.9	121 608 758.8
GOLDEN SPIKE D-3 B	292.9	207 350.1
GOLDEN SPIKE D-3 C	329.2	237 169.1
GOLDEN SPIKE D-3 D	852.5	514 188.4
HAYNES D-3 A	1428.2	1 073 061.1
HOMEGLEN-RIMBEY D-3	6062.0	4 859 199.0
HOMEGLEN-RIMBEY D-3 B	408.7	24 6515.8
INNISFAIL D-3	25 704.0	21 276 779.0
LEDUC-WOODBEND LEDUC A	44 236.0	29 957 203.0
LEDUC-WOODBEND D-3 B	5563.7	3 659 469.5
LEDUC-WOODBEND D-3 F	839.3	552 028.0
LONE PINE CREEK D-3 A	146.9	119 378.8
MALMO D-3 A	2893.0	1 833 794.7
MEDICINE RIVER D-3 A	411.2	331 917.0
MEDICINE RIVER D-3 D	271.4	219 086.3
MEDICINE RIVER D-3 F	478.9	367 821.0
MIKWAN D-3 B	280.1	198 297.8
MORINVILLE D-3 B	1519.6	1 029 084.9
MORINVILLE D-3 C	150.5	84 417.9
MORINVILLE D-3 E	267.6	133 331.5
MORINVILLE D-3 H	114.4	56 989.3
MORINVILLE-D-3 K	128.7	84 637.9
NEVIS D-3 E	288.6	182 957.8
NEW NORWAY D-3	541.2	269 655.7
PEMBINA D-3 A	3230.1	2 505 018.6
REDWATER D-3	95 061.3	15 304 861.5
RICH D-3 A	544.0	385 068.5
ST ALBERT-BIG LAKE D-3 A	2653.2	1 600 300.3
ST ALBERT-BIG LAKE D-3 B	983.0	592 906.5
STETTLER D-3 A	4063.1	2 575 475.5
STETTLER D-3 B	330.4	209 425.8
SYLVAN LAKE D-3 B	550.9	434 772.8
SYLVAN LAKE D-3 C	463.9	352 583.5
WESTEROSE D-3	34 229.0	26 546 381.0
WIMBORNE D-3 A	8627.0	6 809 231.0
WIZARD LAKE D-3 A	62 542.0	46 989 877.0
Total	983 930.8	632 980 367.1

Table B4. Non-associated gas reservoirs with ultimate recoveries greater than 500 $10^6 m^3$.

Pool Name		CO_2 Capacity Estimate (at storage pressure)	
		G_{CO_2}	G_{CO_2}
		$10^6 m^3$	Tonnes
BONNIE GLEN D-3 B		5290.1	3 974 578.3
FERRIER D-3 A		60 748.6	59 243 899.7
FERRIER D-3 C		3331.0	3 248 477.0
HARMATTAN-ELKTON D-3 A		8612.9	7 765 841.2
RICINUS D-3 A		7065.9	6 654 947.4
RICINUS D-3 B		3778.5	3 550 867.1
RICINUS D-3 C		2222.6	2 043 780.2
RICINUS D-3 D		2224.0	2 028 585.2
RICINUS WEST D-3 A		86 504.1	83 153 834.4
RICINUS WEST D-3 B		9402.1	9 104 954.8
SYLVAN LAKE D-3 A		1992.2	1 692 188.7
	Total	191 172.0	182 461 954.0

Table B5. Non-associated gas reservoirs with ultimate recoveries greater than 100 $10^6 m^3$.

Pool Name		CO_2 Capacity Estimate (at storage pressure)	
		G_{CO_2}	G_{CO_2}
		$10^6 m^3$	Tonnes
BONNIE GLEN D-3 B		5290.1	3 974 578.3
FERRIER D-3 A		60 748.6	59 243 899.7
FERRIER D-3 B		899.2	876 928.8
FERRIER D-3 C		3331.0	3 248 477.0
GARRINGTON LEDUC A		334.1	294 401.1
GARRINGTON LEDUC F		1088.8	866 221.7
HARMATTAN-ELKTON D-3 A		8612.9	7 765 841.2
RICINUS D-3 A		7065.9	6 654 947.4
RICINUS D-3 B		3778.5	3 550 867.1
RICINUS D-3 C		2222.6	2 043 780.2
RICINUS D-3 D		2224.0	2 028 585.2
RICINUS WEST D-3 A		86 504.1	83 153 834.4
RICINUS WEST D-3 B		9402.1	9 104 954.8
SYLVAN LAKE D-3 A		1992.2	1 692 188.7
	Total	193 494.1	184 499 505.7

Appendix 3 – CO_2 Mass Estimate Results

Table C1. Results of CO_2 mass estimates (in megatonnes) for the DOE-NETL oil and gas, and fluid substitution methods.

Pool Name	Field	Type	DOE-NETL Oil/Gas Method			Fluid Substitution
			P_{10}	P_{50}	P_{90}	
PEMBINA-D-3 A	PEMBINA	Oil	39.35	58.98	78.86	2.51
REDWATER-D-3	REDWATER	Oil	25.85	39.46	53.29	15.3
BONNIE GLEN-D-3 A	BONNIE GLEN	Oil	20.58	29.15	40.13	83.42
HOMEGLEN-RIMBEY-D-3	HOMEGLEN	Oil	18.88	27.64	38.37	4.86
FERRIER-D-3 A	FERRIER	Gas	18.04	26.35	35.84	59.24
RICINUS WEST-D-3 A	RICINUS WEST	Gas	17.91	25.53	35.77	83.15
LEDUC-WOODBEND-LEDUC A	LEDUC	Oil	14.69	20.64	28.48	29.96
NEVIS-DEVONIAN	NEVIS	Gas	14.34	19.72	26.18	
WIZARD LAKE-D-3 A	WIZARD LAKE	Oil	9.46	12.94	17.26	46.99
HARMATTAN-ELKTON-D-3 A	HARMATTAN	Gas	8.97	12.71	20.27	7.77
WIMBORNE-D-3 A	WIMBORNE	Oil	7.27	10.74	14.83	6.81
WESTEROSE-D-3	WESTEROSE	Oil	6.7	8.9	11.85	26.55
INNISFAIL-D-3	INNISFAIL	Oil	3.98	6.46	9.64	21.28
RICINUS-D-3 A	RICINUS	Gas	3.56	5.48	8.02	6.65
GOLDEN SPIKE-D-3 A	GOLDEN SPIKE	Oil	3.28	4.68	6.34	121.61
ACHESON-D-3 A	ACHESON	Oil	2.99	4.42	6.04	218.38
FERRIER-D-3 E	FERRIER	Gas	2.89	4.34	6.02	
CLIVE-D-3 A	CLIVE	Oil	2.66	3.75	5.3	8.04
LONE PINE CREEK-D-3 A	LONE PINE CREEK	Oil	2.63	3.64	5	0.12
FERRIER-D-3 C	FERRIER	Gas	1.7	2.67	3.64	3.25
ERSKINE-D-3	ERSKINE	Oil	1.77	2.46	3.32	10.49
SYLVAN LAKE-D-3 A	SYLVAN LAKE	Oil	1.52	2.34	3.64	
MALMO-D-3 B	MALMO	Gas	0.96	1.44	2.09	
STETTLER-D-3 A	STETTLER	Oil	0.88	1.19	1.64	2.58
GLEN PARK-D-3 A	GLEN PARK	Oil	0.71	1.12	1.68	2.72
NEVIS-D-3 G	NEVIS	Oil	0.61	1.03	1.45	
BASHAW-D-3 A	BASHAW	Oil	0.64	0.9	1.25	2.55
MORINVILLE-D-3 B	MORINVILLE	Oil	0.56	0.88	1.32	1.03
LEDUC-WOODBEND-D-3 B	LEDUC	Oil	0.36	0.67	1.23	3.66
SYLVAN LAKE-D-3 B	SYLVAN LAKE	Oil	0.44	0.63	0.87	0.43
MEDICINE RIVER-D-3 A	MEDICINE RIVER	Oil	0.41	0.63	0.94	0.33
JOFFRE-D-3 B	JOFFRE	Oil	0.36	0.54	0.74	
FAIRYDELL-BON ACCORD-D-3 A	FAIRYDELL	Oil	0.26	0.49	0.74	0.47
BONNIE GLEN-D-3 B	BONNIE GLEN	Gas	0.34	0.49	0.75	3.97
GOLDEN SPIKE-D-3 D	GOLDEN SPIKE	Oil	0.24	0.43	0.67	0.51
FENN-BIG VALLEY-D-3 F	FENN	Oil	0.24	0.42	0.64	1.78
NEVIS-D-3 E	NEVIS	Oil	0.24	0.35	0.57	0.18

Pool Name	Field	Type	DOE-NETL Oil/Gas Method			Fluid Substitution
			P_{10}	P_{50}	P_{90}	
DUHAMEL-D-3 B	DUHAMEL	Oil	0.24	0.33	0.5	3.93
BUFFALO LAKE-D-3 B	BUFFALO LAKE	Oil	0.22	0.31	0.45	1.88
MALMO-D-3 A	MALMO	Oil	0.16	0.27	0.47	1.83
GOLDEN SPIKE-D-3 C	GOLDEN SPIKE	Oil	0.16	0.24	0.38	0.24
FENN-BIG VALLEY-D-3 A	FENN	Oil	0.13	0.23	0.35	0.29
ST ALBERT-BIG LAKE-D-3 A	ST ALBERT	Oil	0.13	0.22	0.34	1.6
CHIGWELL-D-3 B	CHIGWELL	Oil	0.13	0.21	0.33	0.16
GOLDEN SPIKE-D-3 B	GOLDEN SPIKE	Oil	0.12	0.19	0.27	0.21
MEDICINE RIVER-D-3 F	MEDICINE RIVER	Oil	0.13	0.19	0.26	0.37
MORINVILLE-D-3 E	MORINVILLE	Oil	0.13	0.19	0.27	0.13
ST ALBERT-BIG LAKE-D-3 B	ST ALBERT	Oil	0.1	0.19	0.35	0.59
BUFFALO LAKE-D-3	BUFFALO LAKE	Oil	0.11	0.18	0.29	2.58
EWING LAKE-D-3 A	EWING LAKE	Oil	0.12	0.18	0.25	0.24
BASHAW-D-3 B	BASHAW	Oil	0.11	0.17	0.27	
NEVIS-D-3 B	NEVIS	Oil	0.09	0.17	0.28	
HOMEGLEN-RIMBEY-D-3 B	HOMEGLEN	Oil	0.09	0.15	0.24	0.25
LEDUC-WOODBEND-D-3 F	LEDUC	Oil	0.09	0.14	0.22	0.55
FENN-BIG VALLEY-D-3 I	FENN	Oil	0.07	0.12	0.16	0.22
MORINVILLE-D-3 C	MORINVILLE	Oil	0.06	0.11	0.18	0.08
FENN-BIG VALLEY-D-3 E	FENN	Oil	0.07	0.1	0.14	0.32
FENN-BIG VALLEY-D-3 B	FENN	Oil	0.07	0.09	0.13	0.33
WOOD RIVER-D-3 D	WOOD RIVER	Gas	0.03	0.09	0.16	
STETTLER-D-3 B	STETTLER	Oil	0.04	0.08	0.13	0.21
LEDUC-WOODBEND-D-3 E	LEDUC	Oil	0.04	0.08	0.11	
LEDUC-WOODBEND-D-3 C	LEDUC	Oil	0.05	0.07	0.11	
HAYNES-D-3 B	HAYNES	Oil	0.04	0.07	0.1	
NEVIS-D-3 C	NEVIS	Oil	0.05	0.07	0.1	
NEW NORWAY-D-3	NEW NORWAY	Oil	0.03	0.07	0.11	0.27
MALMO-D-3 D	MALMO	Oil	0.03	0.05	0.08	
MIKWAN-D-3 A	MIKWAN	Oil	0.03	0.05	0.07	
FENN-BIG VALLEY-D-3 C	FENN	Oil	0.03	0.04	0.07	
MORINVILLE-D-3 A	MORINVILLE	Oil	0.03	0.04	0.07	
CHIGWELL-D-3 E	CHIGWELL	Oil	0.03	0.04	0.06	
MALMO-D-3 C	MALMO	Oil	0.02	0.04	0.06	
MORINVILLE-D-3 I	MORINVILLE	Oil	0.02	0.03	0.04	
MORINVILLE-D-3 M	MORINVILLE	Oil	0.01	0.03	0.05	
EWING LAKE-D-3 B	EWING LAKE	Oil	0.02	0.03	0.04	
BASHAW-D-3 E	BASHAW	Oil	0.01	0.03	0.05	
MORINVILLE-D-3 H	MORINVILLE	Oil	0.01	0.02	0.04	0.06
DUHAMEL-D-3 A	DUHAMEL	Oil	0.01	0.02	0.02	

Pool Name	Field	Type	DOE-NETL Oil/Gas Method			Fluid Substitution
			P_{10}	P_{50}	P_{90}	
CHIGWELL-D-3 G	CHIGWELL	Oil	0.01	0.02	0.03	
FENN WEST-D-3 A	FENN WEST	Oil	0	0.01	0.02	
STETTLER-D-3 G	STETTLER	Oil	0	0	0.01	

Appendix 4 – Ireton Formation Lithologs

Abbreviations not captured in the lithology legends: U_Enrich, uranium enrichment; Mo_Enrich, molybdenum enrichment; Ni_Enrich, nickel enrichment; V_enrichment, vanadium enrichment; MICP, mercury injection capillary pressure (test)—see Table 14 for MICP sample numbers and associated values.



CARBONATE CORE DESCRIPTION FORM

LOGGED BY: Tyler Hauck

DATE: MArch 3, 2023

WELL NAME: Imperial Golden Spike IN 8-27L-51-27

CORE NO.:

KB:

LOCATION: 102/08-27-051-27W4/00

INTERVAL: Ireton

SLABBED:

STATUS:

FORMATION | FACIES ASSOCIATION | FACIES | POROSITY (EST: V G E P; TYPE) | U_Enrich (0 ppm 2000) | Mo_Enrich (0 ppm 2000) | Ni_Enrich (0 ppm 60) | V_Enrich (0 ppm 400) | CaO (0 wt% 100) | MgO (0 wt% 5) | SiO2 (0 wt% 60) | Zr (0 ppm 100) | Terrigenous_Input (0 ppm 30) | Wireline_GR (0 GAPI 150) | Chem_GR (0 API 300) | MICP (0 2) | DEPTH (1m:40m) | CONTACTS | SHALLOWING-UPWARD CYCLES | Lithology 1 / Lithology Accessories / Fossils / SILICICLASTIC GRAIN SIZE (cong, vc, c, m, f, vf, silt, shale) / Sedimentary Fabrics / Sedimentary Structures / Depositional Environment / LITHOLOGY#2 / CARBONATE FABRIC (Grain, Pack, Wacke, Mud, Sh/Evt) / #3 (0 100) / #5 | Fractures | LITHOLOGY | COLOUR | DESCRIPTION

IRETON
Middle to upper slope

LEDUC

LF3

8-27-1

Sharp
Sharp

1628.76
1628.7 to 1632.5: LF3: Nodular to wavy banded medium-grey calcareous shale and argillaceous carbonate nodules/beds. Abundant cronoid columnals, some articulated. Planar parallel to wavy laminae. No apparent bioturbation. Very fissile along bedding planes.

1632.24
1632.5 to 1632.65: Top Leduc. Thamnopora floatstone in a dark brown matrix. Abundant pyrite throughout. Edges of Thamnopora show fuzzy dolomite. Some dark black wavy shaley partings.

1633.05
1632.65 to 1638.65: Stromatoporoid rudstone/grainstone. Hemispherical to domal stroms. Thick tabular stroms; some thin wafer stroms. Stachyoides common. Light beige-grey. Porosity ~20%. Oil stained. Rubbly in places. Probable reef flat.

1638.26
1638.65 to 1639.3: Peloidal grainstone. Light grey-beige. Oil stained. Minor strom fragments (abraded). Sand apron or foreslope sands.

LEGEND:

Depositional Environments
- Reef Flat (grainstone to packstone, peloidal-coated grain, coid-skeletal)
- Basin (Grey nodular to nodular bedded wackestone to mudstone)

Sedimentary Structures
- Bioturbation
- Parallel Lamination

Sedimentary Fabrics
- Nodular
- Shale laminae

Fossils
- Stromatoporoids, Abraded
- Stromatoporoids, Bulbous
- Stromatoporoids, Cylindrical
- Stromatoporoids, Thick Tabular
- Crinoid
- Thamnopora

Lithology Accessories
- Peloid
- Pyrite Nodule



CARBONATE CORE DESCRIPTION FORM

LOGGED BY: Tyler Hauck

DATE: March 3, 2023

WELL NAME: Diasham Hughes Haynes 6-22-38-24W4

CORE NO.:

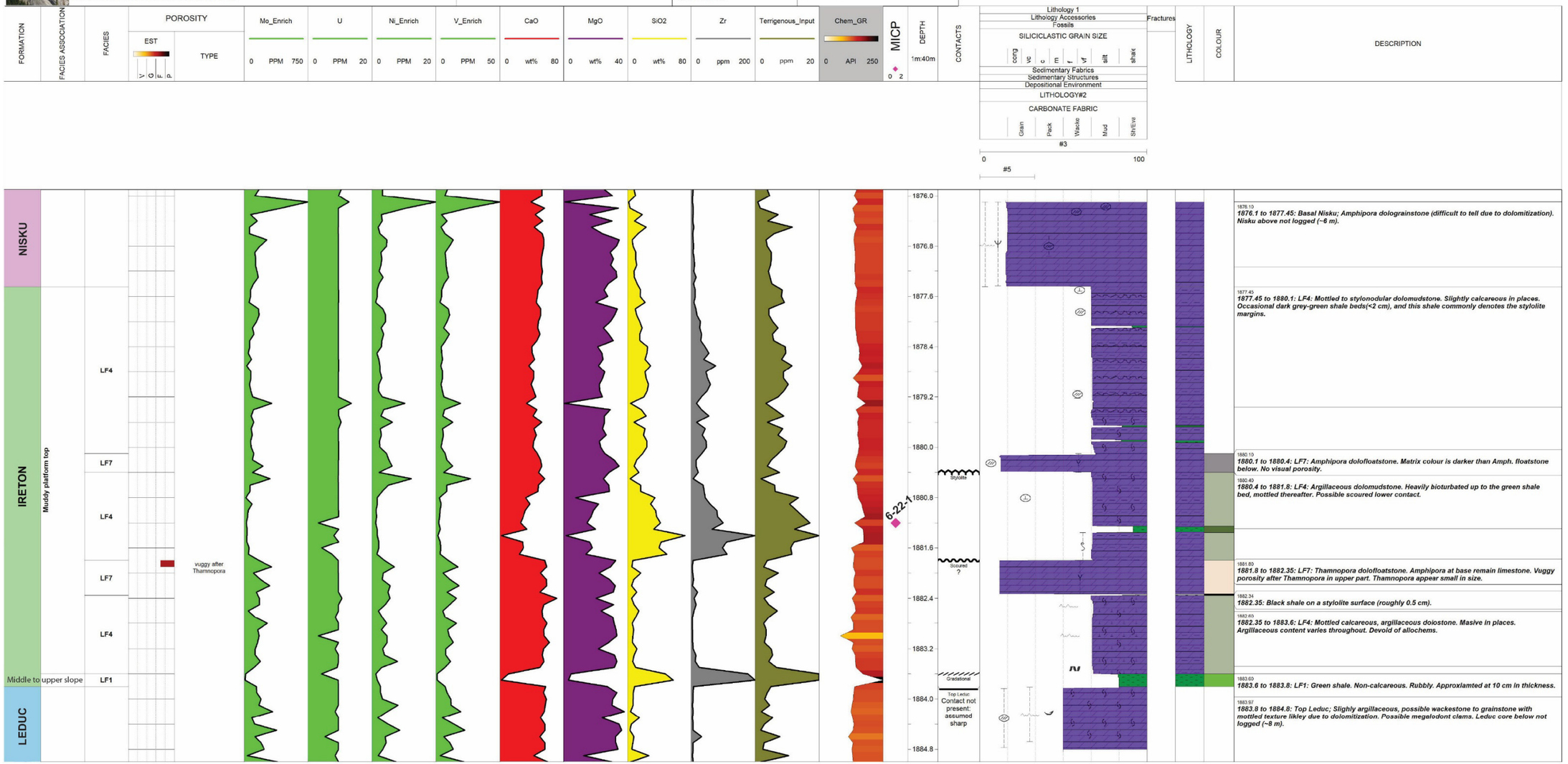
KB:

LOCATION: 100/06-22-038-24W4/00

INTERVAL:

SLABBED:

STATUS:



Sedimentary Structures

- Bioturbation
- Stylolite

Sedimentary Fabrics

- Stylolamina
- Mottled
- Shale laminae

Fossils

- Amphipora
- Bivalve
- Thamnopora

Lithology Accessories

- Anhydrite Nodule
- Calcite nodule
- Rip-up Clasts



CARBONATE CORE DESCRIPTION FORM

WELL NAME: CNRL Nevis 6-18-40-21

LOCATION: 100/06-18-040-21W4/00

LOGGED BY: Tyler Hauck

CORE NO.:

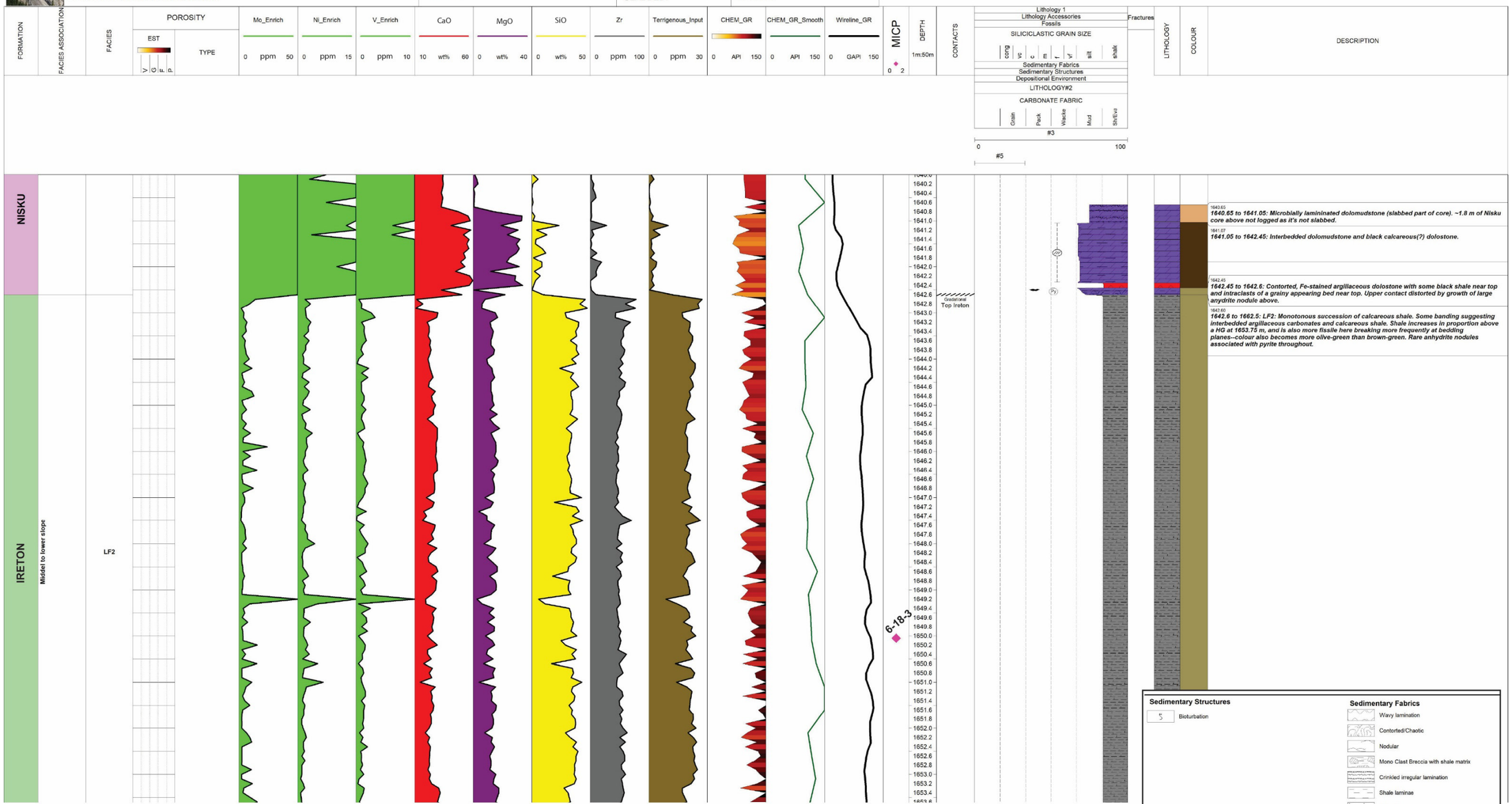
INTERVAL:

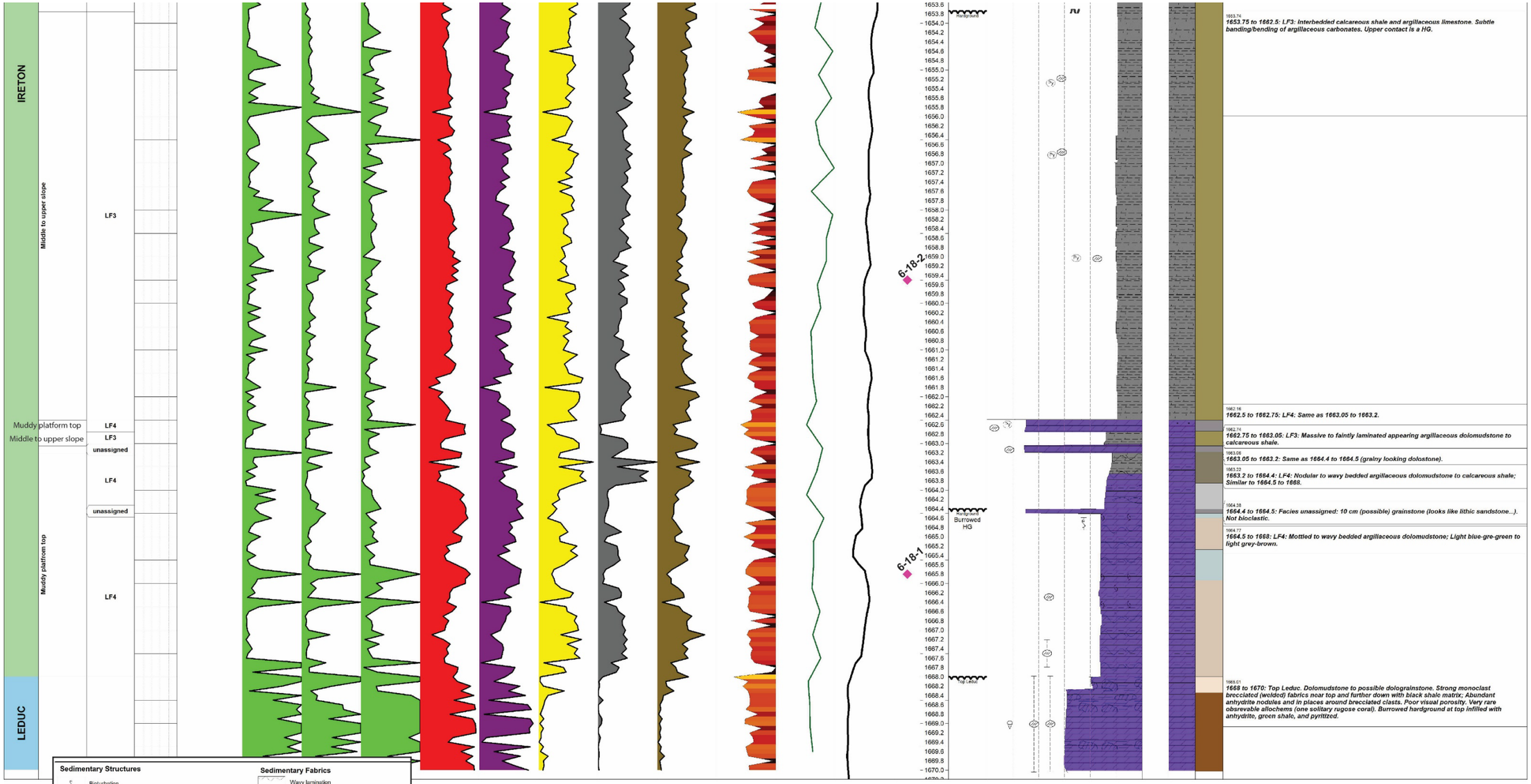
SLABBED:

DATE: March 1, 2023

KB:

STATUS:




IRETON
Middle to upper slope
Muddy platform top
LEDUC
LF3
LF4
unassigned
Muddy platform top
Middle to upper slope
6-18-2
6-18-1
Hardground
Burrowed HG
Top Leduc
1653.76
1653.75 to 1662.5: LF3: Interbedded calcareous shale and argillaceous limestone. Subtle banding/bending of argillaceous carbonates. Upper contact is a HG.
1662.16
1662.5 to 1662.75: LF4: Same as 1663.05 to 1663.2.
1662.74
1662.75 to 1663.05: LF3: Massive to faintly laminated appearing argillaceous dolomudstone to calcareous shale.
1663.06
1663.05 to 1663.2: Same as 1664.4 to 1664.5 (grainy looking dolostone).
1663.22
1663.2 to 1664.4: LF4: Nodular to wavy bedded argillaceous dolomudstone to calcareous shale; Similar to 1664.5 to 1668.
1664.38
1664.4 to 1664.5: Facies unassigned: 10 cm (possible) grainstone (looks like lithic sandstone...). Not bioclastic.
1664.77
1664.5 to 1668: LF4: Mottled to wavy bedded argillaceous dolomudstone; Light blue-gre-green to light grey-brown.
1668.01
1668 to 1670: Top Leduc. Dolomudstone to possible dolograinstone. Strong monoclast brecciated (welded) fabrics near top and further down with black shale matrix; Abundant anhydrite nodules and in places around brecciated clasts. Poor visual porosity. Very rare observable allochems (one solitary rugose coral). Burrowed hardground at top infilled with anhydrite, green shale, and pyritized.
Sedimentary Structures
Bioturbation
Sedimentary Fabrics
Wavy lamination
Contorted/Chaotic
Nodular
Mono Clast Breccia with shale matrix
Crinkled irregular lamination
Shale laminae
Mottled
Fossils
Coral, solitary
Lithology Accessories
Anhydrite Nodule
Rip-up Clasts
Pyrite Nodule
Intraclast



CARBONATE CORE DESCRIPTION FORM

WELL NAME: NAL Ferrier 7-32-37-9

LOCATION: 100/07-32-037-09W5/00

LOGGED BY: Tyler Hauck

CORE NO.:

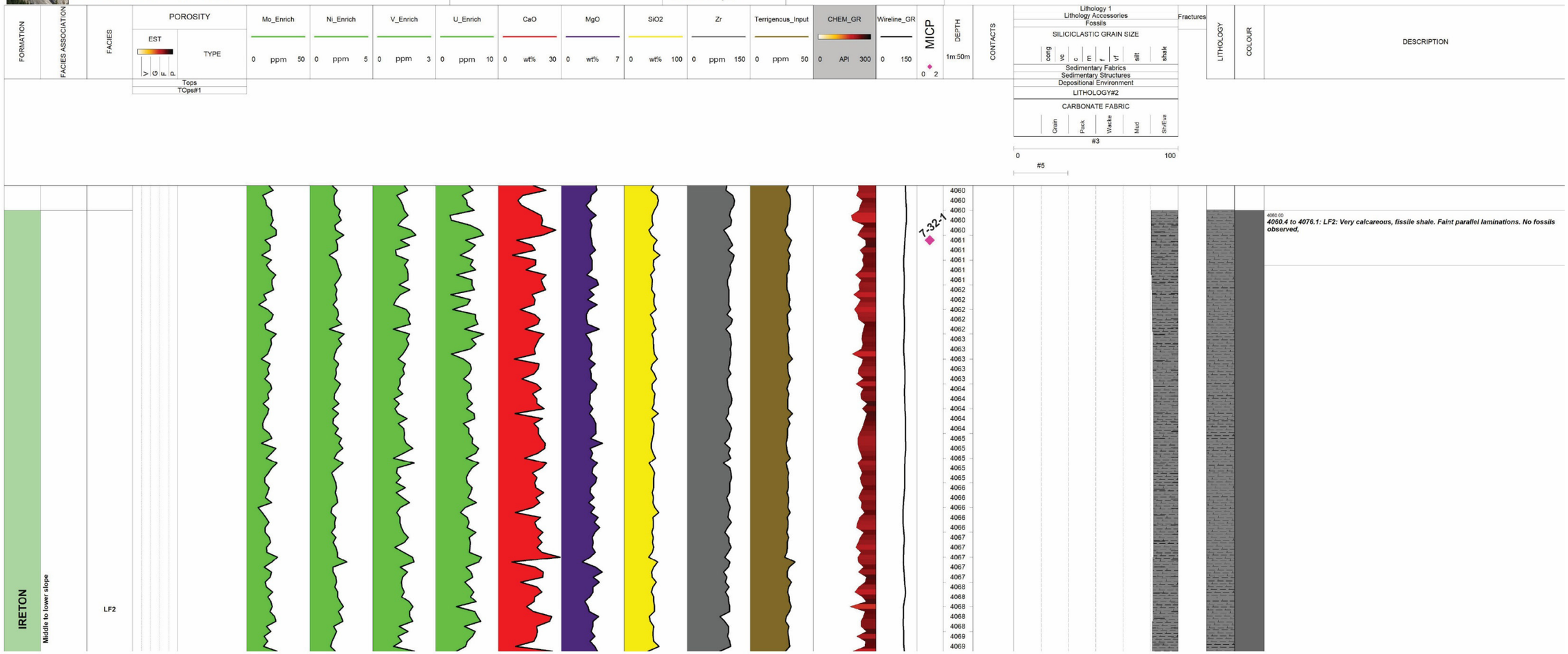
INTERVAL:

SLABBED: yes

DATE: March 2, 2023

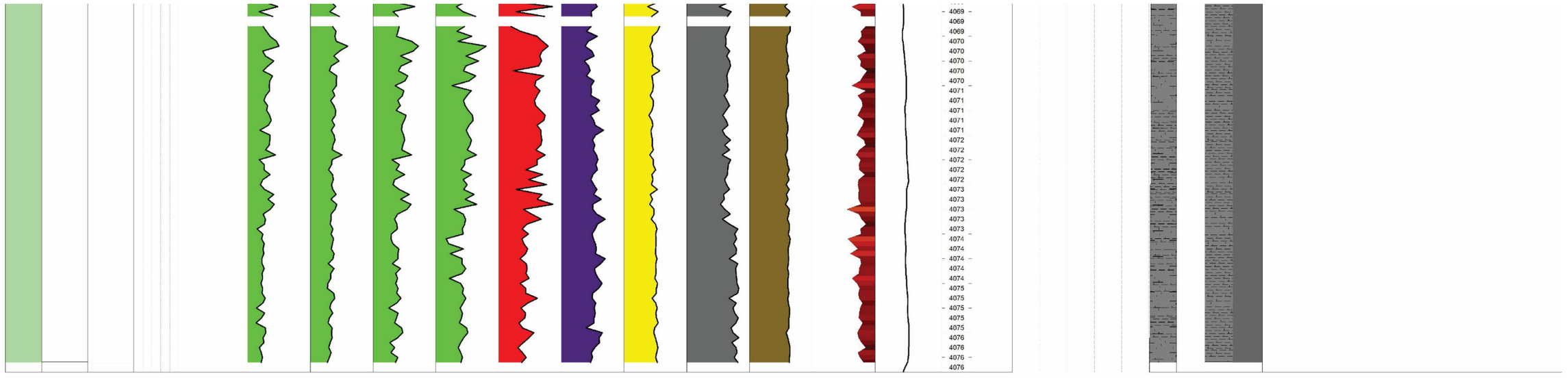
KB:

STATUS:



Sedimentary Fabrics

Shale laminae



Sedimentary Fabrics

Shale laminae



CARBONATE CORE DESCRIPTION FORM

WELL NAME: Vantage Wim. 9-23-33-36

LOCATION: 100/09-23-033-26W4/00

LOGGED BY: Tyler Hauck

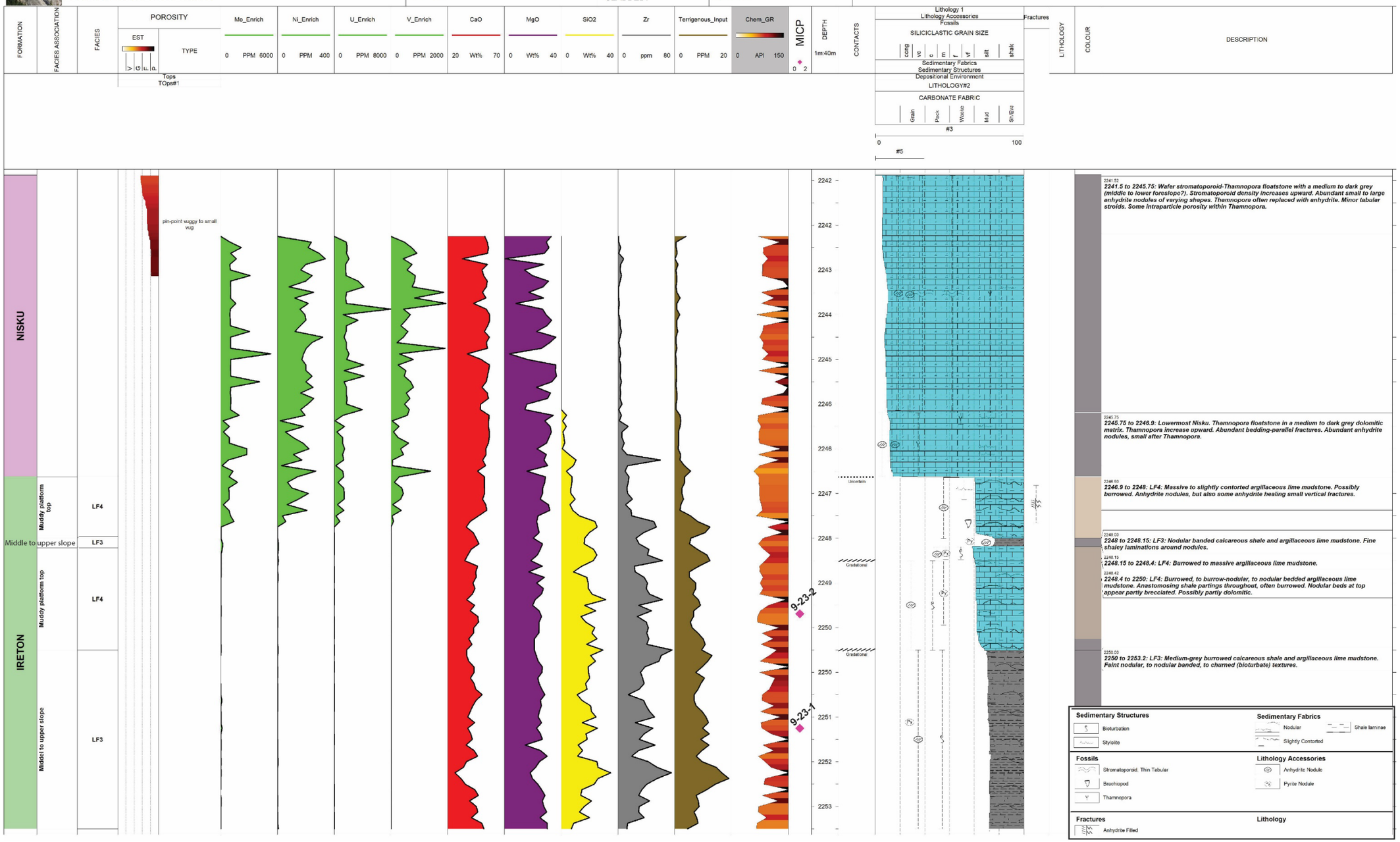
CORE NO.:

INTERVAL: SLABBED:

DATE: March 2, 2023

KB:

STATUS:





CARBONATE CORE DESCRIPTION FORM

LOGGED BY: Tyler Hauck

DATE: March 2, 2023

WELL NAME: Imperial Leduc No 345

CORE NO.:

KB:

LOCATION: 100/12-29-050-26W4/00

INTERVAL:

SLABBED: whole core

STATUS:

FORMATION | FACIES ASSOCIATION | FACIES | POROSITY (EST: V G F P; TYPE; Tops; TOps#1) | Mo_Enrich 0 PPM 3000 | Ni_Enrich 0 PPM 50 | U_Enrich 0 PPM 500 | V_Enrich 0 PPM 200 | CaO 10 Wt% 60 | MgO 0 Wt% 50 | SiO2 0 Wt% 50 | Zr 0 PPM 100 | Terrigenous_Input 0 PPM 40 | CHEM_GR 0 API 300 | GR 0 GAPI 250 | MICP 0 2 | DEPTH 1m:40m | CONTACTS | Lithology 1 / Lithology Accessories / Fossils / Fractures / SILICICLASTIC GRAIN SIZE (cong vc c m f vf silt shale) / Sedimentary Fabrics / Sedimentary Structures / Depositional Environment / LITHOLOGY#2 / CARBONATE FABRIC (Grain Pack Wacke Mud Str/Ext) #3 0 100 #5 | LITHOLOGY | COLOUR | DESCRIPTION

IRETON — Middle to lower slope — LF2

LEDUC

Fenestral and medium vuggy throughout

1609 1610 1610 1611 1612 1613 1614 1614 1615 1616 1617 1618

12-29-1

Gradational possibly sharp...

1608.26
1608.25 to 1615: LF2: Argillaceous, dark olive-green shale. Calcareous and bioturbated in lower 10 cm above Leduc. Faintly planar parallel laminated. Fissile with bedding-plane partings. Apparent lack of bioturbation and fossils (above lower 10 cm).

1615.00
1615 to 1619.25: Tidal flat dolomudstones. Slightly calcareous dolostone with good porosity. Common stylolites.

LEGEND:

Depositional Environments
- Tidal Flat

Sedimentary Structures
- Bioturbation
- Stylolite

Sedimentary Fabrics
- Parallel Lamination

Fossils

Lithology Accessories
- Pyrite Nodule



CARBONATE CORE DESCRIPTION FORM

WELL NAME: Tidewater Acheson 13-2-53-26

LOCATION: 100/13-02-053-26W4/00

LOGGED BY: Tyler Hauck

CORE NO.:

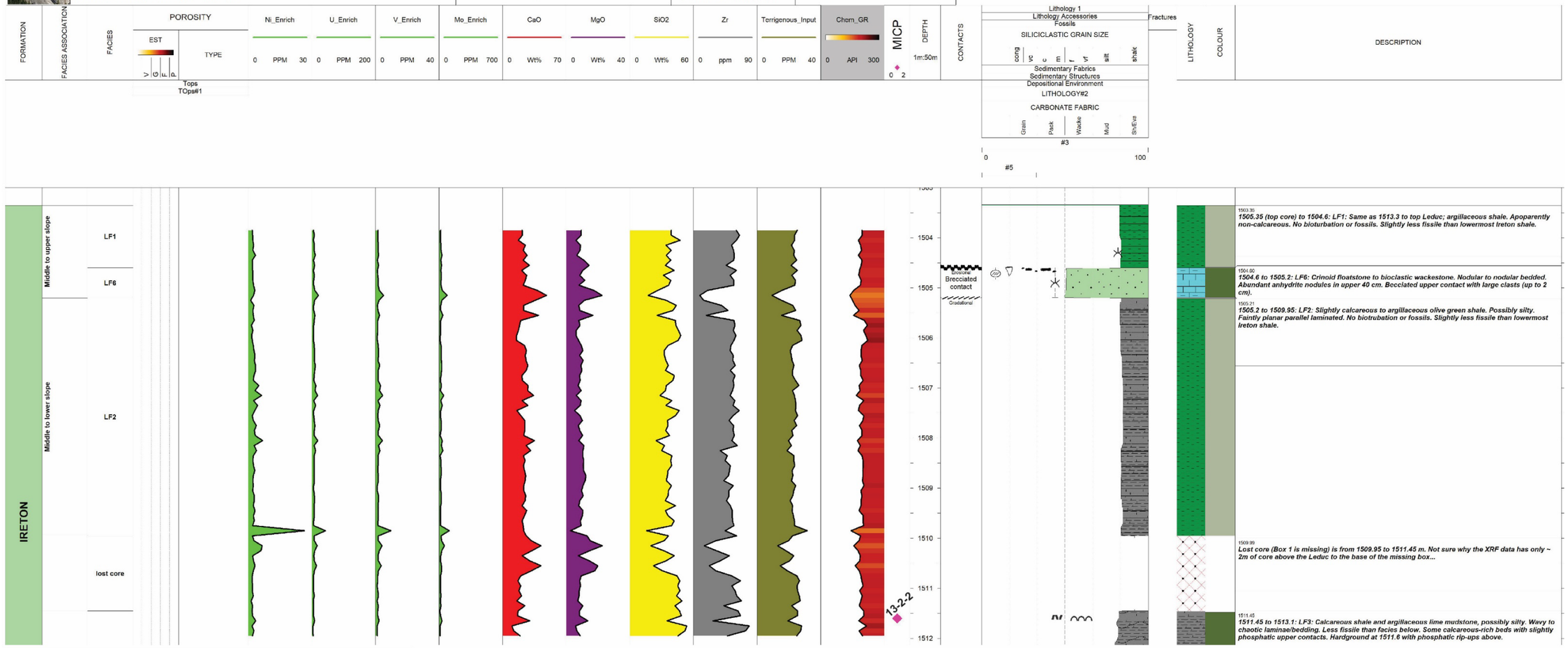
INTERVAL: Ireton

SLABBED: unslabbed

DATE: March 3, 2023

KB:

STATUS:



LEGEND:

Depositional Environments

- Basin (Green Arg, nodular to nodular bedded wackestone and mudstone)

Sedimentary Structures

- Hardground

Sedimentary Fabrics

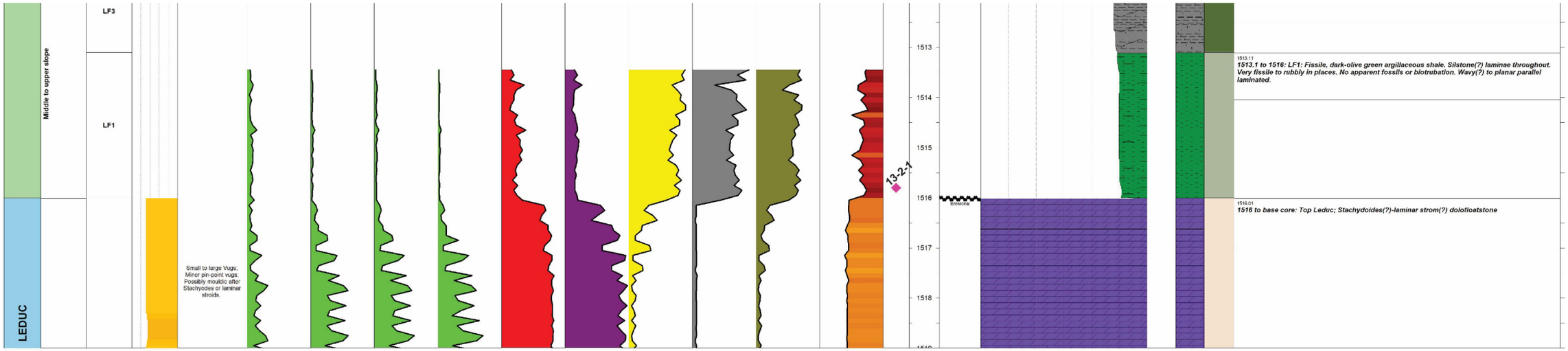
- Parallel Lamination
- Discontinuous Parallel Wavy Lamination
- Shale laminae

Fossils

- Brachiopod
- Crinoid

Lithology Accessories

- Anhydrite Nodule
- Mudstone clasts
- Rip-up Clasts



LEGEND:

Depositional Environments

- Basin (Green Arg, nodular to nodular bedded wackestone and mudstone)

Sedimentary Structures

- Hardground

Sedimentary Fabrics

- Parallel Lamination
- Discontinuous Parallel Wavy Lamination
- Shale laminae

Fossils

- Brachiopod
- Crinoid

Lithology Accessories

- Anhydrite Nodule
- Mudstone clasts
- Rip-up Clasts



CARBONATE CORE DESCRIPTION FORM

LOGGED BY: Tyler Hauck

DATE: March 10, 2023

WELL NAME: Gulf Stettler 14-16-38-20

CORE NO.:

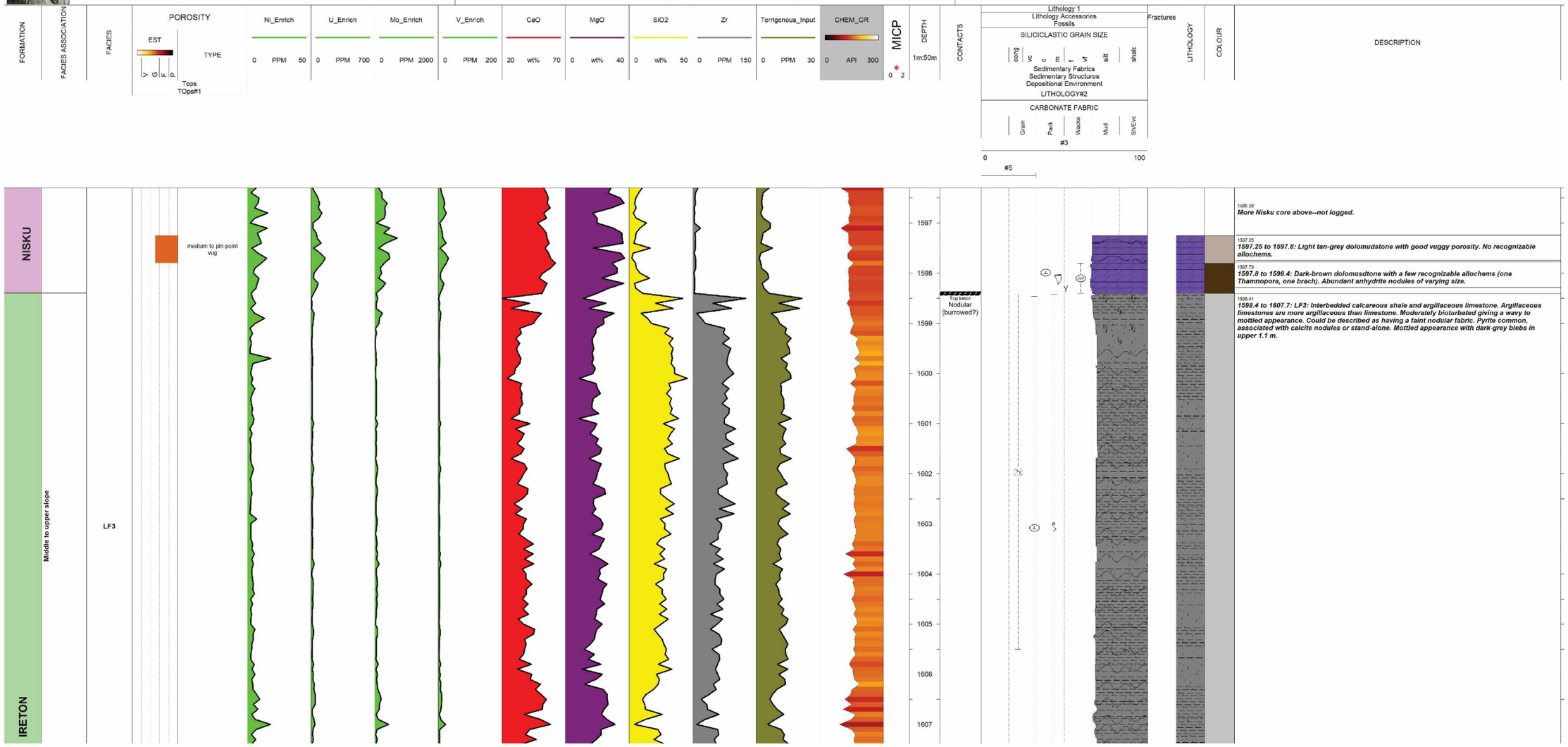
KB:

LOCATION: 100/14-16-038-20W4/00

INTERVAL: Ireton

SLABBED:

STATUS:



Sedimentary Structures

- Bioturbation

Sedimentary Fabrics

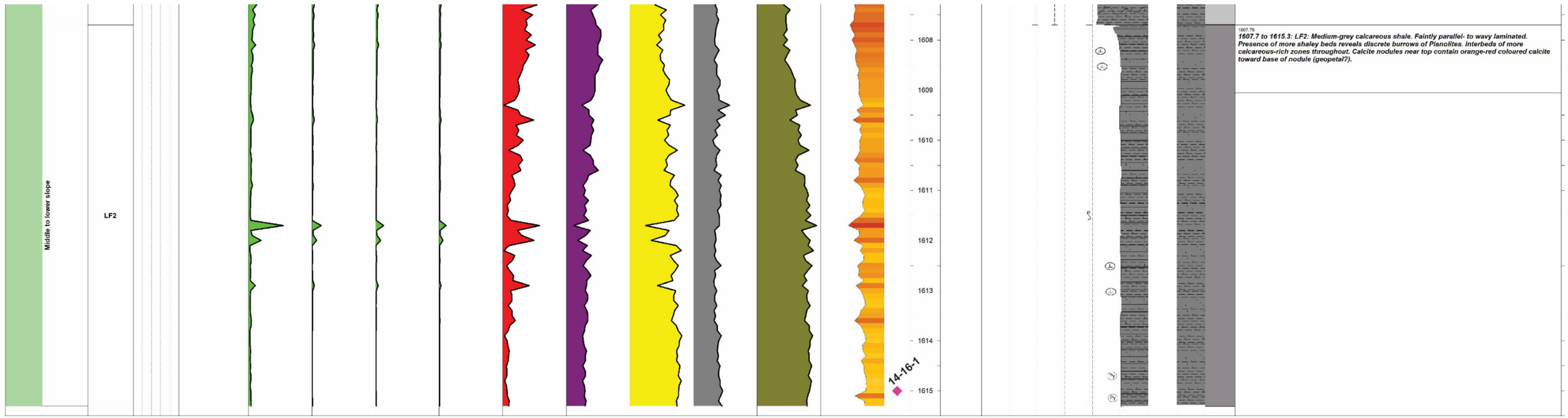
- Parallel Lamination
- Slightly Contorted
- Wavy lamination
- Mottled

Fossils

- Brachiopod
- Thamnopora

Lithology Accessories

- Anhydrite Nodule
- Calcite nodule
- Pyrite Nodule



Sedimentary Structures

- Bioturbation

Sedimentary Fabrics

- Parallel Lamination
- Slightly Contorted
- Wavy lamination
- Mottled

Fossils

- Brachiopod
- Thamnopora

Lithology Accessories

- Anhydrite Nodule
- Calcite nodule
- Pyrite Nodule



CARBONATE CORE DESCRIPTION FORM

WELL NAME: CNRL Erskine 15-24-39-21

LOCATION: 100/15-24-039-21W4/00

LOGGED BY: Tyler Hauck

CORE NO.:

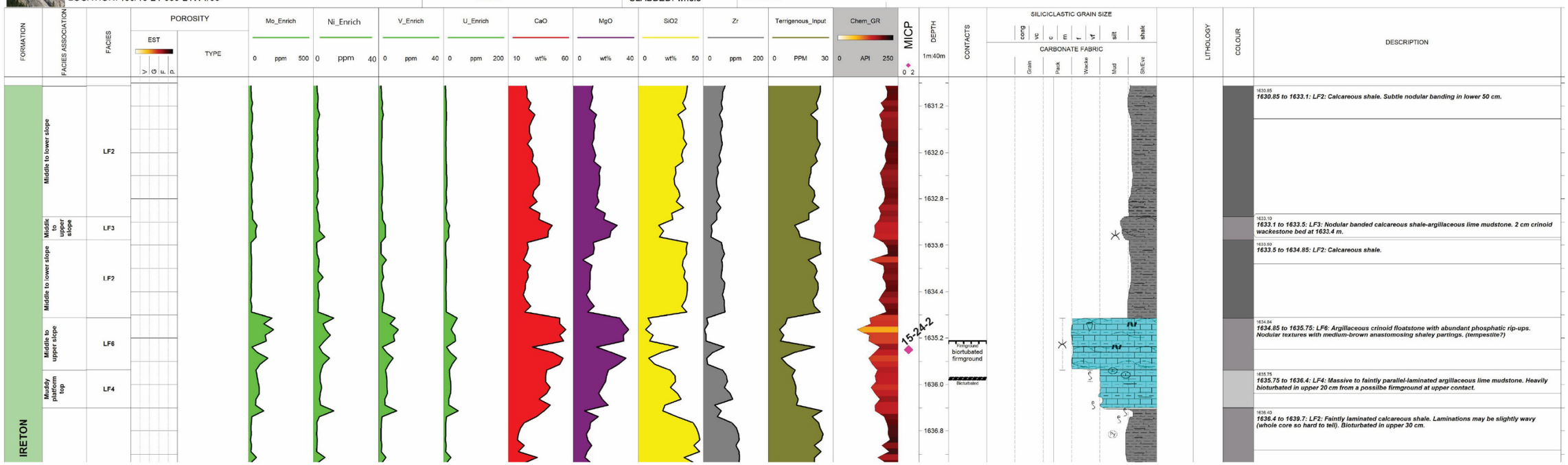
INTERVAL: Ireton

SLABBED: whole

DATE: April 4, 2023

KB:

STATUS:



Sedimentary Structures

- Hardground
- Bioturbation
- Stylolite
- Parallel Lamination

Sedimentary Fabrics

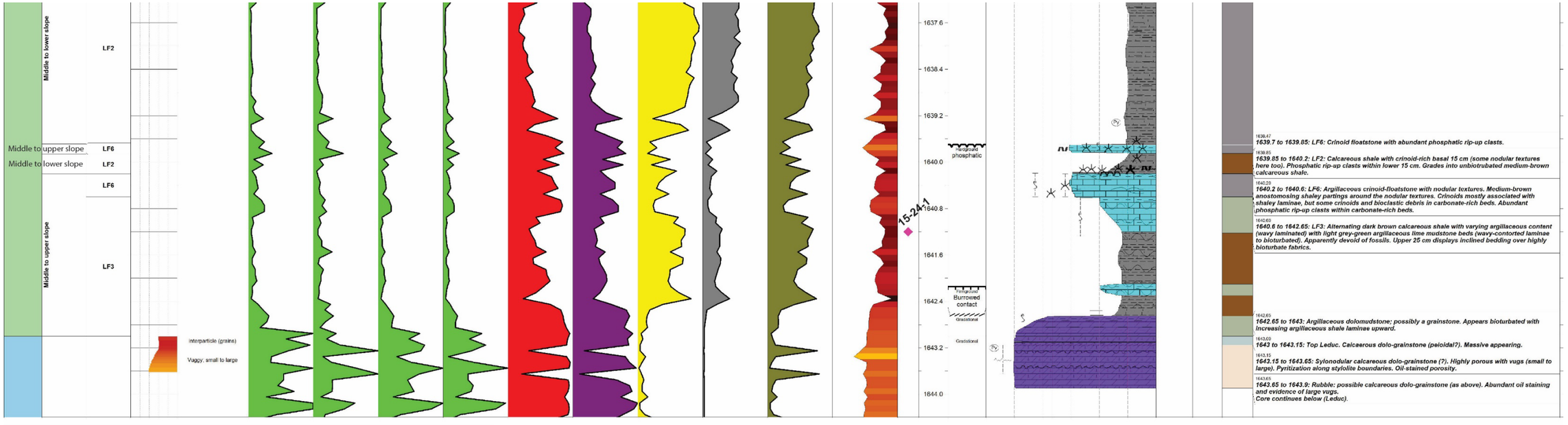
- Wavy lamination
- Nodular
- Stylolamina
- Shale laminae
- Tilted Beds

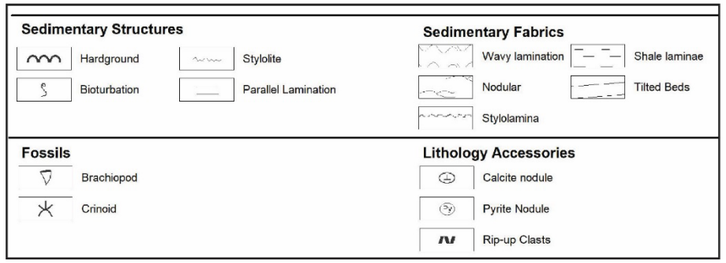
Fossils

- Brachiopod
- Crinoid

Lithology Accessories

- Calcite nodule
- Pyrite Nodule
- Rip-up Clasts


Middle to lower slope
Middle to upper slope
Middle to lower slope
Middle to upper slope
LF2
LF6
LF2
LF6
LF3
interparticle (grains)
Vuggy: small to large
1637.6
1638.4
1639.2
1640.0
1640.8
1641.6
1642.4
1643.2
1644.0
15-24-1
Hardground
phosphatic
Hardground
Burrowed
contact
Gradational
Gradational
1639.47
1639.7 to 1639.85: LF6: Crinoid floatstone with abundant phosphatic rip-up clasts.
1639.85
1639.85 to 1640.2: LF2: Calcareous shale with crinoid-rich basal 15 cm (some nodular textures here too). Phosphatic rip-up clasts within lower 15 cm. Grades into unbioturbated medium-brown calcareous shale.
1640.20
1640.2 to 1640.6: LF6: Argillaceous crinoid-floatstone with nodular textures. Medium-brown anostomosing shaley partings around the nodular textures. Crinoids mostly associated with shaley laminae, but some crinoids and bioclastic debris in carbonate-rich beds. Abundant phosphatic rip-up clasts within carbonate-rich beds.
1640.60
1640.6 to 1642.65: LF3: Alternating dark brown calcareous shale with varying argillaceous content (wavy laminated) with light grey-green argillaceous lime mudstone beds (wavy-contorted laminae to bioturbated). Apparently devoid of fossils. Upper 25 cm displays inclined bedding over highly bioturbate fabrics.
1642.65
1642.65 to 1643: Argillaceous dolomudstone; possibly a grainstone. Appears bioturbated with increasing argillaceous shale laminae upward.
1643.00
1643 to 1643.15: Top Leduc. Calcareous dolo-grainstone (peloidal?). Massive appearing.
1643.15
1643.15 to 1643.65: Sylonodular calcareous dolo-grainstone (?). Highly porous with vugs (small to large). Pyritization along stylolite boundaries. Oil-stained porosity.
1643.65
1643.65 to 1643.9: Rubble: possible calcareous dolo-grainstone (as above). Abundant oil staining and evidence of large vugs.
Core continues below (Leduc).


Sedimentary Structures
Hardground
Stylolite
Bioturbation
Parallel Lamination
Sedimentary Fabrics
Wavy lamination
Shale laminae
Nodular
Tilted Beds
Stylolamina
Fossils
Brachiopod
Crinoid
Lithology Accessories
Calcite nodule
Pyrite Nodule
Rip-up Clasts



CARBONATE CORE DESCRIPTION FORM

WELL NAME: Hudson's Bay Innisfail 15-29-34-1

LOCATION: 100/15-29-034-01W5/00

LOGGED BY: Tyler Hauck

CORE NO.:

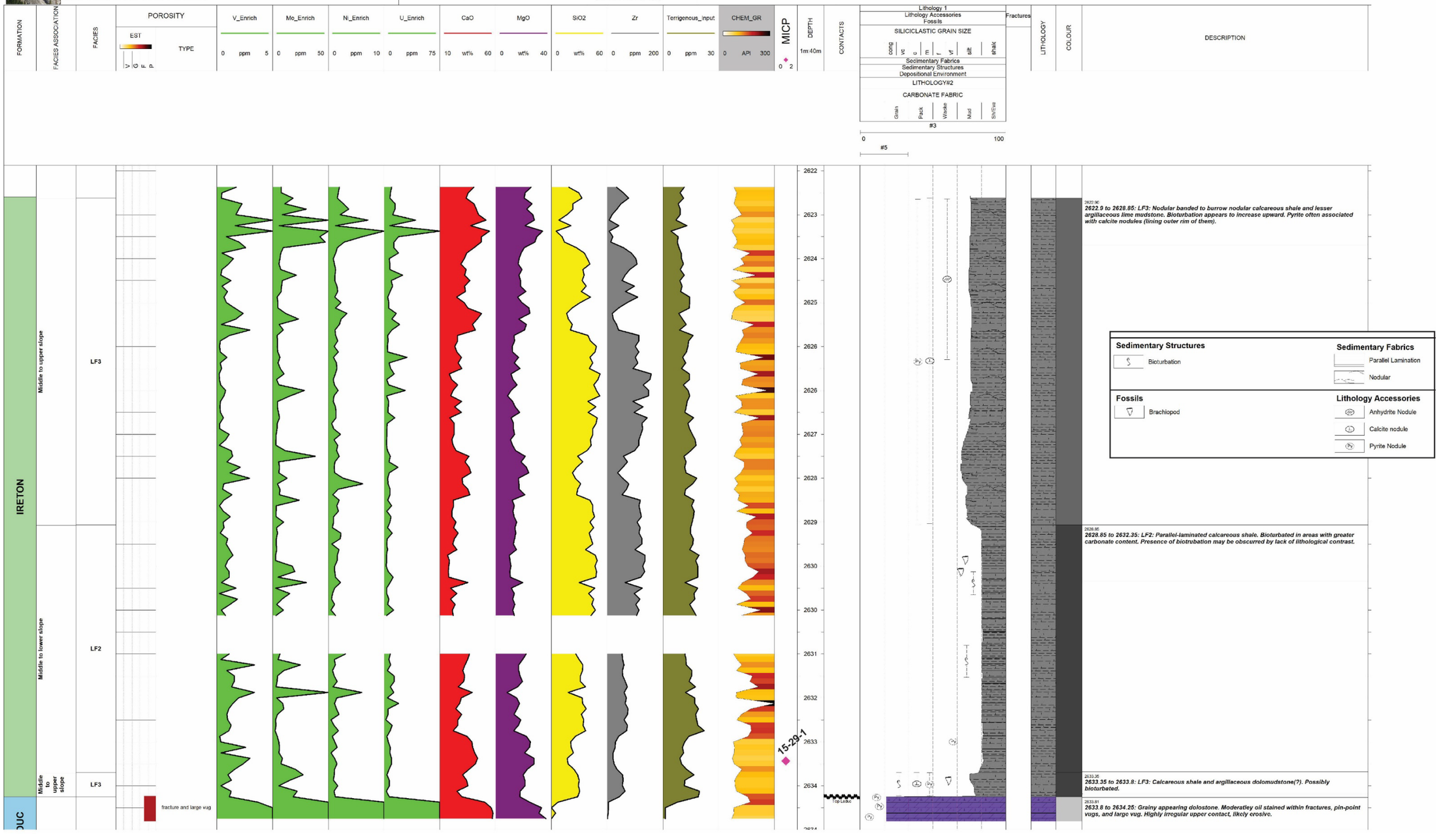
INTERVAL: Ireton

SLABBED: whole

DATE: March 10, 2023

KB:

STATUS:





CARBONATE CORE DESCRIPTION FORM

LOGGED BY: Tyler Hauck

DATE: Mach 3, 2023

WELL NAME: Ember Clive 16-26-39-24

CORE NO.:

KB:

LOCATION: 100/16-26-039-24W4/00

INTERVAL: Ireton

SLABBED:

STATUS:

FORMATION | FACIES ASSOCIATION | FACIES | POROSITY (EST: V, O, u, p; TYPE) | Mo_Enrich (0 ppm 1000) | Ni_Enrich (0 ppm 50) | U_Enrich (0 ppm 200) | V_Enrich (0 ppm 100) | CaO (0 wt% 70) | MgO (0 wt% 40) | SiO2 (0 wt% 60) | Zr (0 ppm 100) | Terrigenous_Input (0 ppm 30) | CHEM_GR (0 API 200) | Wireline_GR (0 GAPI 150) | MICP (0 2) | DEPTH (1m:50m) | CONTACTS | Lithology 1 | Lithology Accessories | Fossils | SILICICLASTIC GRAIN SIZE (cong, vc, c, m, f, vf, silt, shale) | Sedimentary Fabrics | Sedimentary Structures | Depositional Environment | LITHOLOGY#2 | CARBONATE FABRIC (Grain, Pack, Wkstn, Mud, Sh/Evp) | #3 (0 100) | #5 | Fractures | LITHOLOGY | COLOUR | DESCRIPTION

Sedimentary Structures

- Fenestral
- Stylolite
- Bioturbation

Sedimentary Fabrics

- Wavy lamination
- Mottled
- Nodular
- Tilted Beds
- Stylolamina

Fossils

- Amphipora
- Thamnopora
- Brachiopod
- Crinoid

Lithology Accessories

- Anhydrite Nodule
- Calcite nodule

NISKU

IRETON

Muddy platform top; thin intervals upper slope

LF4

LF7

LF4

LEDUC

vuggy after Amphipora

1845 1846 1847 1848 1849 1850 1851 1852 1853 1854 1855 1856 1857 1858

Nisku meteoric cont.

16-26-3

16-26-2

16-26-1

Gradational

Sharp

Scoured

Uncertain
Possibly gradational

1844.56
1844.85 to 1846.8: Lowermost Nisku. Massive to mottled dolostone. Slightly argillaceous in lower half. Partly calcareous. Possibly bioturbated, but lack of shale may hide this. Anhydrite nodules common. More Nisku core above; not logged; abundance of anhydrite nodules increases dramatically and nodules are larger. ~ 3 m above logged portion vuggy Nisku porosity becomes abundant.

1846.82
1846.8 to 1852.4: LF4: Stylo- to burrow-nodular argillaceous dolostone; slighty calcareous in places. Common anhydrite nodules throughout (1 - 4 cm). Bioturbation is 3-5. Possibly silty dolostone in places. Argillaceous content varies (e.g., see 1848.9 m with many shale laminations/beds = LF3). Almost devoid of allochems.

1848.96
1848.9: example of thin (12 cm) interval of LF3; another below at 1851.75 m

1852.38
1852.4 to 1852.7: LF4: Mottled argillaceous dolostone. Possibly bioturbated. Rare fossil debris.

1852.66
1852.7 to 1853.5: LF7: Calcareous shale with skeletal debris(?) in lower 20 cm, grading into a Thamnopora floatstone. Matrix is dark grey-black with thin wispy, anostomosing dark-black shale partings.

1853.48
1853.5 to 1855.3: LF4: Massive to mottled medium to light-grey-green calcareous, argillaceous dolostone. Wispy anostomosing dark shale partings in swarms that are inclined. Argillaceous content increases upward. Rare brachs.

1856.32
1855.3 to 1858.85 (base core): Leduc Formation: Lower Amphipora floatstone in a dark grey-black lime mudstone matrix, grading up into a light grey-tan possible Amphipora floatstone with a dark grey to beige dolomudstone matrix. Most vugs appear mouldic after Amphipora. Upper contact is uncertain--made at top of mouldic porosity.